Integrating Active Devices to Structures with Aperture-Coupled Microstrip Feeding

Peter M. Frank

A thesis presented to

University of Manitoba

in partial fulfillment of the requirements for

the degree of Master of Science

Winnipeg, Manitoba, 1996

ISBN 0-612-16133-1

Canada

Name PETER FRANK

Dissertation Abstracts International and *Masters Abstracts International* are arranged by broad, general subject categories. Please select the one subject which most nearly describes the content of your dissertation or thesis. Enter the corresponding four-digit code in the spaces provided.

SUBJECT TERM

ELECTRICAL ENGINEERING

0544 UMI

SUBJECT CODE

Subject Categories

THE HUMANITIES AND SOCIAL SCIENCES

COMMUNICATIONS AND THE ARTS
Architecture 0729
Art History 0377
Cinema 0900
Dance 0378
Design and Decorative Arts 0389
Fine Arts 0357
Information Science 0723
Journalism 0391
Landscape Architecture 0390
Library Science 0399
Mass Communications 0708
Music 0413
Speech Communication 0459
Theater 0465

EDUCATION
General 0515
Administration 0514
Adult and Continuing 0516
Agricultural 0517
Art 0273
Bilingual and Multicultural 0282
Business 0688
Community College 0275
Curriculum and Instruction 0727
Early Childhood 0518
Elementary 0524
Educational Psychology 0525
Finance 0277
Guidance and Counseling 0519
Health 0680
Higher 0745
History of 0520
Home Economics 0278
Industrial 0521
Language and Literature 0279
Mathematics 0280
Music 0522
Philosophy of 0998
Physical 0523
Reading 0535
Religious 0527
Sciences 0714
Secondary 0533
Social Sciences 0534
Sociology of 0340
Special 0529
Teacher Training 0530
Technology 0710
Tests and Measurements 0288
Vocational 0747

LANGUAGE, LITERATURE AND LINGUISTICS
Language
- General 0679
- Ancient 0289
- Linguistics 0290
- Modern 0291
- Rhetoric and Composition 0681

Literature
- General 0401
- Classical 0294
- Comparative 0295
- Medieval 0297
- Modern 0298
- African 0316
- American 0591
- Asian 0305
- Canadian (English) 0352
- Canadian (French) 0355
- Caribbean 0360
- English 0593
- Germanic 0311
- Latin American 0312
- Middle Eastern 0315
- Romance 0313
- Slavic and East European 0314

PHILOSOPHY, RELIGION AND THEOLOGY
Philosophy 0422
Religion
- General 0318
- Biblical Studies 0321
- Clergy 0319
- History of 0320
- Philosophy of 0322

Theology 0469

SOCIAL SCIENCES
American Studies 0323
Anthropology
- Archaeology 0324
- Cultural 0326
- Physical 0327

Business Administration
- General 0310
- Accounting 0272
- Banking 0770
- Management 0454
- Marketing 0338

Canadian Studies 0385
Economics
- General 0501
- Agricultural 0503
- Commerce-Business 0505
- Finance 0508
- History 0509
- Labor 0510
- Theory 0511

Folklore 0358
Geography 0366
Gerontology 0351
History
- General 0578
- Ancient 0579
- Medieval 0581
- Modern 0582
- Church 0330
- Black 0328
- African 0331
- Asia, Australia and Oceania 0332
- Canadian 0334
- European 0335
- Latin American 0336
- Middle Eastern 0333
- United States 0337

History of Science 0585
Law 0398
Political Science
- General 0615
- International Law and Relations 0616
- Public Administration 0617

Recreation 0814
Social Work 0452
Sociology
- General 0626
- Criminology and Penology 0627
- Demography 0938
- Ethnic and Racial Studies 0631
- Individual and Family Studies 0628
- Industrial and Labor Relations 0629
- Public and Social Welfare 0630
- Social Structure and Development 0700
- Theory and Methods 0344

Transportation 0709
Urban and Regional Planning 0999
Women's Studies 0453

THE SCIENCES AND ENGINEERING

BIOLOGICAL SCIENCES
Agriculture
- General 0473
- Agronomy 0285
- Animal Culture and Nutrition 0475
- Animal Pathology 0476
- Fisheries and Aquaculture 0792
- Food Science and Technology 0359
- Forestry and Wildlife 0478
- Plant Culture 0479
- Plant Pathology 0480
- Range Management 0777
- Soil Science 0481
- Wood Technology 0746

Biology
- General 0306
- Anatomy 0287
- Animal Physiology 0433
- Biostatistics 0308
- Botany 0309
- Cell 0379
- Ecology 0329
- Entomology 0353
- Genetics 0369
- Limnology 0793
- Microbiology 0410
- Molecular 0307
- Neuroscience 0317
- Oceanography 0416
- Plant Physiology 0817
- Veterinary Science 0778
- Zoology 0472

Biophysics
- General 0786
- Medical 0760

EARTH SCIENCES
Biogeochemistry 0425
Geochemistry 0996
Geodesy 0370
Geology 0372
Geophysics 0373
Hydrology 0388
Mineralogy 0411
Paleobotany 0345
Paleoecology 0426
Paleontology 0418
Paleozoology 0985
Palynology 0427
Physical Geography 0368
Physical Oceanography 0415

HEALTH AND ENVIRONMENTAL SCIENCES
Environmental Sciences 0768
Health Sciences
- General 0566
- Audiology 0300
- Dentistry 0567
- Education 0350
- Administration, Health Care 0769
- Human Development 0758
- Immunology 0982
- Medicine and Surgery 0564
- Mental Health 0347
- Nursing 0569
- Nutrition 0570
- Obstetrics and Gynecology 0380
- Occupational Health and Safety 0354
- Oncology 0992
- Ophthalmology 0381
- Pathology 0571
- Pharmacology 0419
- Pharmacy 0572
- Public Health 0573
- Radiology 0574
- Recreation 0575
- Rehabilitaion and Therapy 0382
- Speech Pathology 0460
- Toxicology 0383

Home Economics 0386

PHYSICAL SCIENCES
Pure Sciences
Chemistry
- General 0485
- Agricultural 0749
- Analytical 0486
- Biochemistry 0487
- Inorganic 0488
- Nuclear 0738
- Organic 0490
- Pharmaceutical 0491
- Physical 0494
- Polymer 0495
- Radiation 0754

Mathematics 0405
Physics
- General 0605
- Acoustics 0986
- Astronomy and Astrophysics 0606
- Atmospheric Science 0608
- Atomic 0748
- Condensed Matter 0611
- Electricity and Magnetism 0607
- Elementary Particles and High Energy 0798
- Fluid and Plasma 0759
- Molecular 0609
- Nuclear 0610
- Optics 0752
- Radiation 0756

Statistics 0463

Applied Sciences
Applied Mechanics 0346
Computer Science 0984
Engineering
- General 0537
- Aerospace 0538
- Agricultural 0539
- Automotive 0540
- Biomedical 0541
- Chemical 0542
- Civil 0543
- Electronics and Electrical 0544
- Environmental 0775
- Industrial 0546
- Marine and Ocean 0547
- Materials Science 0794
- Mechanical 0548
- Metallurgy 0743
- Mining 0551
- Nuclear 0552
- Packaging 0549
- Petroleum 0765
- Sanitary and Municipal 0554
- System Science 0790

Geotechnology 0428
Operations Research 0796
Plastics Technology 0795
Textile Technology 0994

PSYCHOLOGY
General 0621
Behavioral 0384
Clinical 0622
Cognitive 0633
Developmental 0620
Experimental 0623
Industrial 0624
Personality 0625
Physiological 0989
Psychobiology 0349
Psychometrics 0632
Social 0451

THE UNIVERSITY OF MANITOBA

FACULTY OF GRADUATE STUDIES

COPYRIGHT PERMISSION

INTEGRATING ACTIVE DEVICES TO STRUCTURES WITH APERTURE-COUPLED MICROSTRIP FEEDING

BY

PETER M. FRANK

A Thesis/Practicum submitted to the Faculty of Graduate Studies of the University of Manitoba in partial fulfillment of the requirements for the degree of

MASTER OF SCIENCE

ABSTRACT

In this thesis a method of mounting active devices to an aperture-coupled microstrip antenna is investigated. The goal of the research is to incorporate a thick ground plane with a minimum thickness of 0.635 mm into the antenna operating at approximately 19.5 GHz. This thickness will insure that active devices mounted on metallic carriers can be fastened to the ground plane with screws.

The modal expansion method for an aperture-coupled rectangular microstrip antenna and the transmission line matrix method are briefly described, which are utilized throughout the thesis.

The research investigates two methods of adding a thick ground plane to an aperture-coupled microstrip antenna. The first method replaces the thin ground plane with a thick ground plane. The aperture located between the antenna radiating element and the transmission line is machined into the thick ground plane. After numerous analyses and experimentation, this method was abandoned. The second method places a thick ground plane with a large cavity between the thin ground plane (containing the aperture) and the transmission line substrate. The operation of this antenna is similar to an aperture-coupled microstrip antenna with a thin ground plane, with the exception of a lower front-to-side radiation ratio. This antenna was tested with and without a low noise amplifier. The approximate noise temperature and G/T ratio of the antenna was calculated.

Table of Contents

List of Figures

List of Tables

Acknowledgments:

I would like to thank the following:

Professor Sebak for accepting me as a graduate student and giving me the excellent opportunity to conduct my research at the Communications Research Centre in Ottawa.

The incredible people at the Communications Research Centre in Ottawa: especially Dr. David Roscoe and Dr. Neil Simons for their excellent help and for being advisors at a home away from home. Also included are Dr. Apisak Ittipiboon, Brian Clarke, John Bradley, Carol Glaser, Aldo Petosa, Michel Cuhaci and Rene Douville. All research was conducted at this facility with the help of these individuals.

All my wonderful thesis related friends who brought me much joy throughout those years: Shailesh Raut, Bo Hu, Vibeke Vaerum, Carlos DeAlmeida, "Vigor" Vanessa Zaror, Duane Mateychuk, Larry and Michelle, Nikhil "The Coolest" Adnani, "Big" Tony Davidson, Dan Drolet, Neil Simons, Michel Gaudreault, and the three women: Pauline, Stephanie and Kiran.

My supporting family: Mama and Papa for teaching me the value and delight of an education, Monika, Anita and Krista for always being there for me whenever I needed their help.

Chapter 1:

Introduction

1.0 Introductory Remarks

The use of wireless communications by society is rapidly increasing. Communication devices that are lightweight, small and conformal are preferred, and generally the antenna is large relative to the electronic hardware. Therefore, in many personal communication applications, microstrip antennas are preferred due to their lightweight and conformal attributes. Unfortunately, they tend to have a lower gain in comparison to other types of antennas such as horns. One technique for increasing the gain of an antenna system is with the the addition of a device such as an LNA (Low Noise Amplifier) or a PA (Power Amplifier).

As frequencies increase towards the MMW (Millimeter Wave) band, the wavelength becomes shorter and many decibels of attenuation can occur between the antenna element and the modulator or demodulator. If the distance causes a large enough signal attenuation, the signal-to-noise ratio may become unacceptable. One method of compensating for signal attenuation is the addition of either a PA or an LNA at strategic locations in the antenna structure to amplify the modulated signal. Another method is to incorporate either a modulator [1] or demodulator into the antenna element to significantly remove path loss of the modulated signal.

Another reason for adding active devices to antenna structures is in the application

of active phased arrays. Phase shifters are utilized to steer electronically the direction of radiation transmitted or received from the antenna array.

This thesis investigates methods of integrating active devices to aperture-coupled microstrip antennas. The goal is to fasten a carrier to a thick metallic surface located in the antenna structure with screws; a carrier is a small metallic device which contains the active MIC (Microwave Integrated Circuit). The best approach of adding the thick metal to the antenna would be to combine the thin ground plane with the thick metal. The coupling efficiency could not be hindered by this process.

The active devices must fastened to the thick metal with screws for the following reasons. First of all, screws ensure good electrical and physical contact with the metallic surface. Bonding the carrier with an epoxy instead may result in loss of contact due to differing coefficients of expansion and time. Secondly, screws allow for easy removal and replacement for repair purposes.

The thick metal can also be utilized as a source of heat dissipation for the active devices.

1.1 Thesis Overview

The purpose of the thesis is to find a method of mounting active devices to an aperture-coupled rectangular microstrip antenna at an operating frequency of approximately 19.5 GHz. The antenna must contain a thick ground plane with a minimum thickness of 0.635 mm, because this thickness ensures that screws can be used to fasten active devices on metallic carriers to the ground plane.

The research examines two possible methods for mounting the carrier to the

ground plane of an aperture-coupled microstrip antenna:

METHOD 1: The first method replaces the thin ground plane with a thick ground plane. The aperture would be machined into the thick ground plane and would resemble a waveguide of finite thickness.

METHOD 2: The second method involves a thick ground plane with a large cavity centered directly between the thin ground plane containing the aperture and the transmission-line substrate.

The research of this thesis is contained in five chapters. The present chapter introduces the purpose, the goals, and an overview of the thesis. The second chapter briefly presents the theory of two numerical techniques utilized in the research of various antenna and transmission line structures. The numerical techniques included are modal expansion method for an aperture-coupled rectangular microstrip antenna [2], and the TLM (Transmission Line Matrix) method [3]. The third chapter presents the method and the results of coupling energy through an aperture in a thick ground plane (Method 1). Also, the TLM method results for these structures are compared with experimental results to determine the accuracy of the method. The fourth chapter examines the possibility of implementing Method 2. An aperture-coupled microstrip antenna containing a 0.635 mm thick ground plane is designed and tested with and without an LNA. The final chapter presents and discusses the results, and offers possible future research directions.

Chapter 2:

Modal Expansion and TLM Methods

This chapter presents a brief theoretical description of the modal expansion method and TLM (Transmission Line Matrix) method. These two methods were utilized in software tools for the design of all structures presented in the thesis.

2.0 Introductory Remarks

Software tools are required to analyze various microstrip antenna structures and transitions. The three-dimensional TLM method is chosen to analyze transmission line transitions and multiple-port aperture-coupled structures. The TLM analysis software is based on the three-dimensional symmetric condensed node model [4]. The TLM method is useful for calculating structures with arbitrary geometries. The disadvantages of the method are the rigorous calculations and intense computational time.

The modal expansion method is a tool which is chosen to analyze aperture-coupled microstrip antennas. This tool is based on approximations and fixed structure geometries and therefore generally calculates results quickly.

2.1 Modal Expansion Method for Aperture-Coupled Microstrip Antenna

In this section the modal expansion analysis of an aperture-coupled rectangular microstrip patch antenna is presented. The patch is analyzed using the cavity model, the

feedline is analyzed with the dynamic-planar-waveguide model, and the aperture-coupling is obtained via the magnetic current in the aperture. The derivations are primarily from [2] and [5].

The layout and coordinate system of the antenna are illustrated in Figure 2.1.

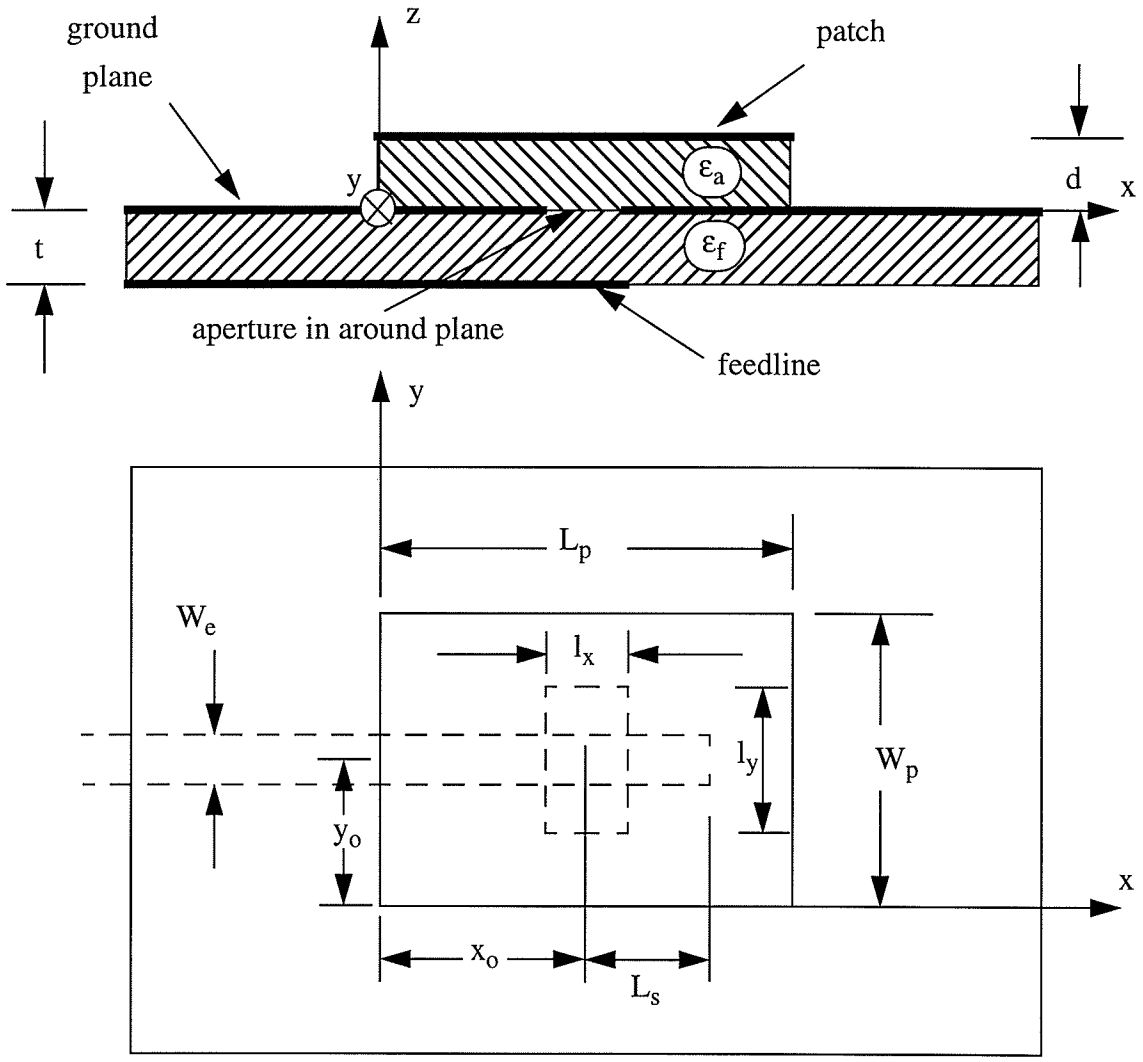

Figure 2.1: Layout of the aperture-coupled microstrip antenna

The patch antenna consists of a dielectric slab, surrounded on four sides by magnetic walls and on the top and bottom by electric walls. The microstrip feedline couples to the cavity

through a narrow slot aligned along the y-axis in the common ground plane.

2.1.1 Aperture Coupling of the Cavity

The TE (transverse electric) field expansion to the y direction is used because the slot magnetic current is directed along the y axis. The $\bar{E}$ (electric) and $\bar{H}$ (magnetic) fields are determined from [6]:

$$\bar{E} = -\nabla \times \psi \hat{a}_y \tag{2.1}$$

$$\bar{H} = -j\omega\varepsilon\psi\hat{a}_y + \frac{1}{j\omega\mu}\nabla(\nabla \cdot \psi\hat{a}_y) \tag{2.2}$$

where $\hat{a}_y$ is a unit vector in the y direction, ψ is an electric scalar function, ω is the angular frequency, ε is the permittivity, and μ is permeability. The modal fields in the cavity must satisfy:

$$\nabla^2\psi + k^2\psi = 0 \tag{2.3}$$

where $k = \omega\sqrt{\mu\varepsilon}$, $\varepsilon = \varepsilon_o\varepsilon_{eff}$, $\varepsilon_o = 8.854 \times 10^{-12}$F/m and ε_{eff}=effective dielectric constant.

The unknown function ψ is found by applying boundary conditions. The boundary conditions for the magnetic field components require the tangential components to be zero on the side walls; for the electric field components, the tangential components must be zero on the top and bottom walls. The depth of the cavity is small compared to the wavelength [7]; therefore the field components can be considered to be independent of $\hat{z}$. The expansions of (2.1) and (2.2) become:

$$E_x = 0 \qquad H_x = \frac{1}{j\omega\mu}\frac{\partial^2}{\partial_x \partial_y}\psi \tag{2.4}$$

$$E_y = 0 \qquad H_y = \frac{1}{j\omega\mu}\left[\frac{\partial^2}{\partial_y^2} + k^2\right]\psi \tag{2.5}$$

$$E_z = -\frac{\partial}{\partial_x}\psi \qquad H_z = 0 \tag{2.6}$$

The scalar function ψ^a is the homogeneous wave equation solution. Inhomogenous boundary conditions are set for the slot, and solution is given by [5]:

$$\psi^a = \frac{2}{a_e b_e}\sum_{mn}\alpha_m\left(\frac{l_x \sin\left(\frac{n\pi}{a_e}x_o\right)}{\gamma_m k_z \sin k_z d}\right)\sin\left(\frac{n\pi}{a_e}x\right)\cos\left(\frac{m\pi}{b_e}y\right)\cos\left(k_z(z-d)\right) \tag{2.7}$$

where $m, n \neq 0$

$$\gamma_m = 1;\ m = 0$$

$$\gamma_m = \frac{1}{2};\ m \neq 0$$

and k_z is given by:

$$k_z^2 = k_o^2 \varepsilon_{a,\,eff} - \left(\frac{m\pi}{b_e}\right)^2 - \left(\frac{n\pi}{a_e}\right)^2 \tag{2.8}$$

where k_o is the free space wavenumber, $\varepsilon_{a,\,eff}$ is the effective permittivity of the cavity [8], and a_e and b_e are the effective length L_p and width W_p of the cavity which account for fringing fields at the edges [9]. The coefficients α_m are given by:

$$\alpha_m = \int_0^{b_e} f(y)\cos\left(\frac{m\pi}{b_e}y\right)dy \tag{2.9}$$

The function $f(y)$ corresponds to the electric field distribution in the slot and is given by:

$$\bar{E}_a = Vf(y)\,\hat{a}_x \tag{2.10}$$

where

$$f(y) = \frac{1}{l_x};\quad y_o - \frac{W_e}{2} \le y \le y_o + \frac{W_e}{2}$$

$$f(y) = \frac{1}{l_x}\frac{\sin k_s (l_y - |y - y_o|)}{\sin \frac{k_s}{2}(l_y - W_e)};\quad \frac{W_e}{2} \le |y - y_o| \le \frac{l_y}{2}$$

$$f(y) = 0;\quad \text{otherwise}. \tag{2.11}$$

The wavenumber k_s is given by [10]:

$$k_s = k_o \sqrt{\frac{\varepsilon_a + \varepsilon_f}{2}} \tag{2.12}$$

where ε_a and ε_f are the dielectric constants of the antenna element and the microstrip transmission line, respectively. The effective width of the transmission line is given by W_e. The voltage V is maintained at a constant value.

2.1.2 Aperture Coupling of the Feedline

The modal-field expansions of the total $\bar{E}$ and $\bar{H}$ fields of the microstrip feedline can be obtained by applying the Dynamic-Planar-Waveguide Model [11]. The upper and lower surfaces of the feedline are electric walls of width W_e and the sidewalls are magnetic walls of thickness t.

Coupling between the feedline and patch through the aperture is derived using the Concept of Reaction [6] and the Reciprocity Theorem. The formulas are obtained by

declaring two regions around the slot, as shown in Figure 2.2. The fields scatter at the slot due to the incident field of the dominant mode from Region I. The resulting effects can be expanded in the modal fields which are TE-to-y. The $\bar{E}$ and $\bar{H}$ fields can be determined from (2.1) and (2.2) after ψ^f has been found in Regions I and II.

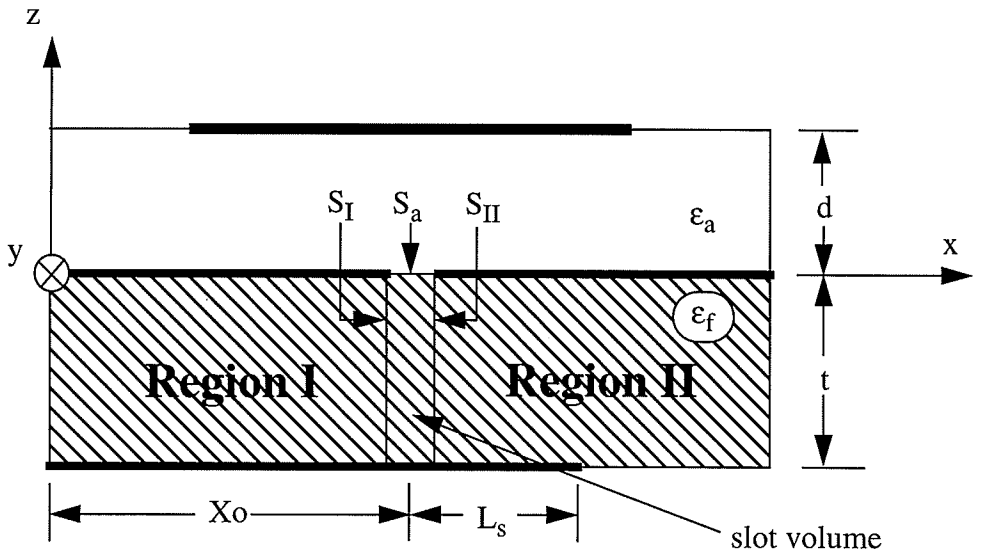

Figure 2.2: Various regions for the aperture-coupled microstrip antenna feedline geometry

From [5], the scalar function for the feedline in Regions I and II is found to be:

$$\psi_I^f = A_o e^{-jk_x x} + A_I^- e^{jk_x x} + \sum_{mn}' A_{mn}^- e^{\alpha_{mn} x} \cos\left[\left(\frac{m\pi}{t}\right)(z+t)\right] \cdot \cos\left[\left(\frac{n\pi}{W_e}\right)\left(y - y_o + \frac{W_e}{2}\right)\right]; \quad x \le x_o \tag{2.13}$$

$$\psi_{II}^f = A_{II}^+ e^{-jk_x x} + A_{II}^- e^{jk_x x} + \sum_{mn}' A_{mn}^+ e^{-\alpha_{mn} x} \cos\left[\left(\frac{m\pi}{t}\right)(z+t)\right] \cdot \cos\left[\left(\frac{n\pi}{W_e}\right)\left(y - y_o + \frac{W_e}{2}\right)\right]; \quad x \ge x_o \tag{2.14}$$

where:

$$k_x^2 = k_o^2 \varepsilon_{f,\,eff} - \left(\frac{m\pi}{t}\right)^2 - \left(\frac{n\pi}{W_e}\right)^2 \tag{2.15}$$

$$\alpha_{mn}^2 = \left(\frac{m\pi}{t}\right)^2 + \left(\frac{n\pi}{W_e}\right)^2 - k_o^2 \varepsilon_{f,\,eff} \tag{2.16}$$

The effective permittivity of the feedline is given by $\varepsilon_{f,\,eff}$. The substrate thickness is given by t. The symbol $\sum'_{mn}$ implies that the dominant mode (m=n=0) is excluded. The amplitude of the incident field is given by A_o. The unknown expansion coefficients A_I^-, A_{mn}^-, A_{II}^+, A_{II}^-, and A_{mn}^+ need to be determined. The coefficients A_{II}^+ and A_{II}^- are related through the terminating load at $x = x_o + L_s$. By the use of the Lorentz Reciprocity Theorem [6], the total $\bar{E}$ and $\bar{H}$ fields using the various sets of test fields over the volume V around the slot (Figure 2.2) enables the expansion coefficients to be determined in terms of the incident and induced slot fields [5].

2.1.3 Circuit Model

After the relevant field components in the regions defined in Figure 2.2 have been determined, the Poynting Theorem applied to the slot volume is used to derive the input admittance of the slot coupled microstrip antenna. The following is found:

$$\frac{1}{2}\oint_S (E \times H) \cdot \hat{n} ds = -2jw\left(\frac{\mu}{4}\int_V H \cdot H dv - \frac{\varepsilon}{4}\int_V E \cdot E dv\right) \tag{2.17}$$

The volume integrals can be neglected, since L_s is small, which yields a first-order approximation:

$$\frac{1}{2}\oint_S (\bar{E}\times\bar{H})\cdot\bar{n}ds = 0 \tag{2.18}$$

Therefore:

$$\frac{1}{2}\int_{S_1} (\bar{E}_I\times\bar{H}_I)\cdot\hat{a}_x ds = \frac{1}{2}\int_{S_2} (\bar{E}_{II}\times\bar{H}_{II})\cdot\hat{a}_x ds + \frac{1}{2}\int_{S_a} E_{\mathrm{d}} H_y ds \tag{2.19}$$

where H_y is the y-component of the $\bar{H}$ field in the cavity. By substituting for the $\bar{E}$ and $\bar{H}$ values, and performing some algebraic manipulation, (2.18) can be reduced to:

$$y_{in}V_T^2 = y_L V_L^2 + y_s V_s^2 \tag{2.20}$$

where

$$V_T = jk_s A_o t\left(1 - \frac{A_I}{A_o}e^{2jk_s x_o}\right)e^{-jk_s x_o} \tag{2.21}$$

$$V_L = jk_s A_{II}^{+} t\left(1 + e^{-2jk_s L_s}\right)e^{-jk_s x_o} \tag{2.22}$$

The voltage across the feedline is represented by V_T and the voltage across the matching section at the plane of the slot is represented by V_L. The voltage across the slot which is seen by the feedline is represented by V_S. The input admittance which is seen by the microstrip line at a plane central to the slot is given by y_{in}. The admittance of the matching stub at the slot is given by y_L. The total admittance is y_s (comprised of the admittance of the higher order modes inside the guide y_e, and the admittance of slot-fed microstrip antenna y_a), where:

$$y_s = y_e + N^2 y_a. \tag{2.23}$$

An approximation for N in equation (2.23) can be found in [12] from the expression for stripline. From (2.20), an equivalent circuit for the slot-fed microstrip element can be derived, which is illustrated in Figure 2.3. The antenna input admittance, y_{in}, can be calculated by:

$$\frac{1}{y_{in}} = \frac{1}{y_L} + \frac{1}{y_s}. \tag{2.24}$$

The value y_e is generally neglected since y_a is much larger.

The back-plane radiation, described by y_b, is assumed to be small [10], and is therefore disregarded. The back-plane radiation can only be neglected as long as the slot length is small in comparison to the resonant length.

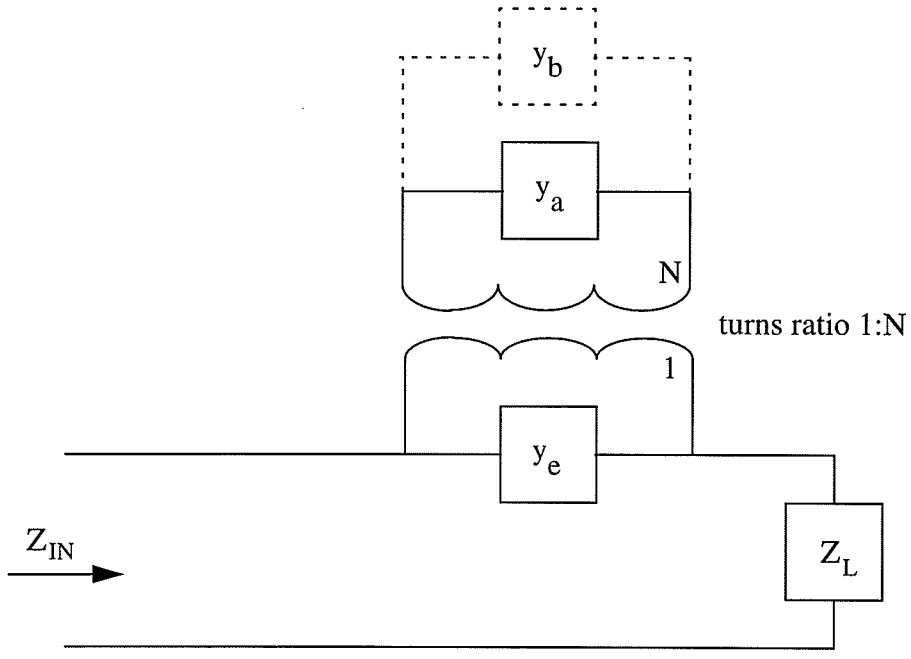

Figure 2.3: Aperture-coupled microstrip antenna equivalent circuit

The slot-fed microstrip antenna admittance, y_a, is stationary with respect to the included slot fields. By applying the Laurent's series expansion to ω_{01} (which is the

angular resonant frequency of the dominant mode), the admittance y_a is:

$$y_a = -\frac{j}{\omega\mu}\left(\frac{2}{a_e b_e}\right) l_x^2 \cdot \left[\frac{\omega^2 \alpha_o^2}{2d} \sin\left(\frac{\pi x_o}{a_e}\right)^2 \left\{ \frac{1}{\omega'_{01}(\omega - \omega'_{01})} - \frac{1}{2\omega'^2_{01}} \right\} + \sum'_{mn} \frac{\left(k_o^2 \varepsilon_{a,\,eff} - \left(\frac{m\pi}{b_e}\right)^2\right)}{\gamma_m} \cdot \alpha_m^2 \sin\left(\frac{n\pi x_o}{a_e}\right) \cdot \frac{\cos k_z d}{k_z \sin k_z d} \right] \tag{2.25}$$

where ω_{01} is given by:

$$\omega_{01} = \frac{c_o \pi}{a_e \sqrt{\varepsilon_{a,\,eff}}} \tag{2.26}$$

and ω'_{01} is given by:

$$\omega'_{01} = \omega_{01}\left(1 + \frac{j}{2Q}\right) \tag{2.27}$$

and c_o is the speed of light in free space.

The quality factor of the patch element is given by Q, which is calculated from [13] using the admittance of the radiating wall, given by [14]. The total admittance comprising the admittance of the higher order modes inside the guide, y_e, is given by:

$$y_e = \frac{1}{2}\sum'_{mn} y_{mn} \frac{\left[\int_{S_a} f(y)\, \psi_{mn}\, dxdy\right]^2}{\int_S \psi_{mn}^2\, dydz} \tag{2.28}$$

where S_a is the area of the slot, S is the cross-sectional area of the waveguide at $x=x_o$, and:

$$y_{mn} = j\frac{\left(k_o^2\varepsilon_{f,\,eff} - \left(\frac{n\pi}{W_e}\right)^2\right)}{\omega\mu\alpha_{mn}} \tag{2.29}$$

$$\psi_{mn} = \cos\left(\left(\frac{m\pi}{t}\right)(z+t)\right)\cos\left(\left(\frac{n\pi}{W_e}\right)\left(y - y_o + \frac{W_e}{2}\right)\right) \tag{2.30}$$

where $\sum'$ denotes that m=0, n=1 is excluded.

Aperture-coupled rectangular microstrip antenna elements can now be evaluated without *a priori* assumptions, using the equivalent circuit (Figure 2.3) and the definitions given in (2.19)-(2.30).

2.2 TLM Method

The TLM method is a numerical technique capable of solving general problems containing nonlinear, inhomogeneous, anisotropic, time-dependent material properties and arbitrary geometries [15]. For simplicity, this section will describe the two-dimensional TLM shunt-node [3] method. Most of the technique described in this chapter is applicable to the three-dimensional method and is based on [16].

2.2.1 Description of the TLM Algorithm

The two-dimensional model can provide an approximate solution based on the following equations:

$$\frac{\partial E_z}{\partial x} = \mu\frac{\partial H_y}{\partial t} \tag{2.31}$$

$$\frac{\partial E_z}{\partial y} = -\mu\frac{\partial H_x}{\partial t} \tag{2.32}$$

$$\frac{\partial H_y}{\partial x} - \frac{\partial H_x}{\partial y} = \varepsilon\frac{\partial E_z}{\partial t} \tag{2.33}$$

Equations (2.31)-(2.33) are derived from Maxwell's equations with $\frac{\partial}{\partial z} = 0$ and H_z=0.

The TLM method utilizes a discretized uniform grid of interconnected transmission lines. Each transmission line has a characteristic impedance of Z_l. A voltage pulse is initiated at a specified location on the grid, and the pulse propagates and evolves in accordance with the algorithm. Each voltage pulse represents a discrete component of the field distribution.

The operation of incident and scattered waves for the two-dimensional TLM algorithm is illustrated in Figure 2.4. The figure reveals the progression of the incident and scattered voltage pulses at t-Δt/2 through time t+Δt/2. The spatial locations for the four nodes are given by:

node 1: (x_o, y_o)

node 2: $(x_o + \Delta l, y_o)$

node 3: $(x_o, y_o - \Delta l)$

node 4: $(x_o + \Delta l, y_o - \Delta l)$

The algorithm consists of scattering events and transfer events. The scattering events for the original two-dimensional shunt-node are given by [3]:

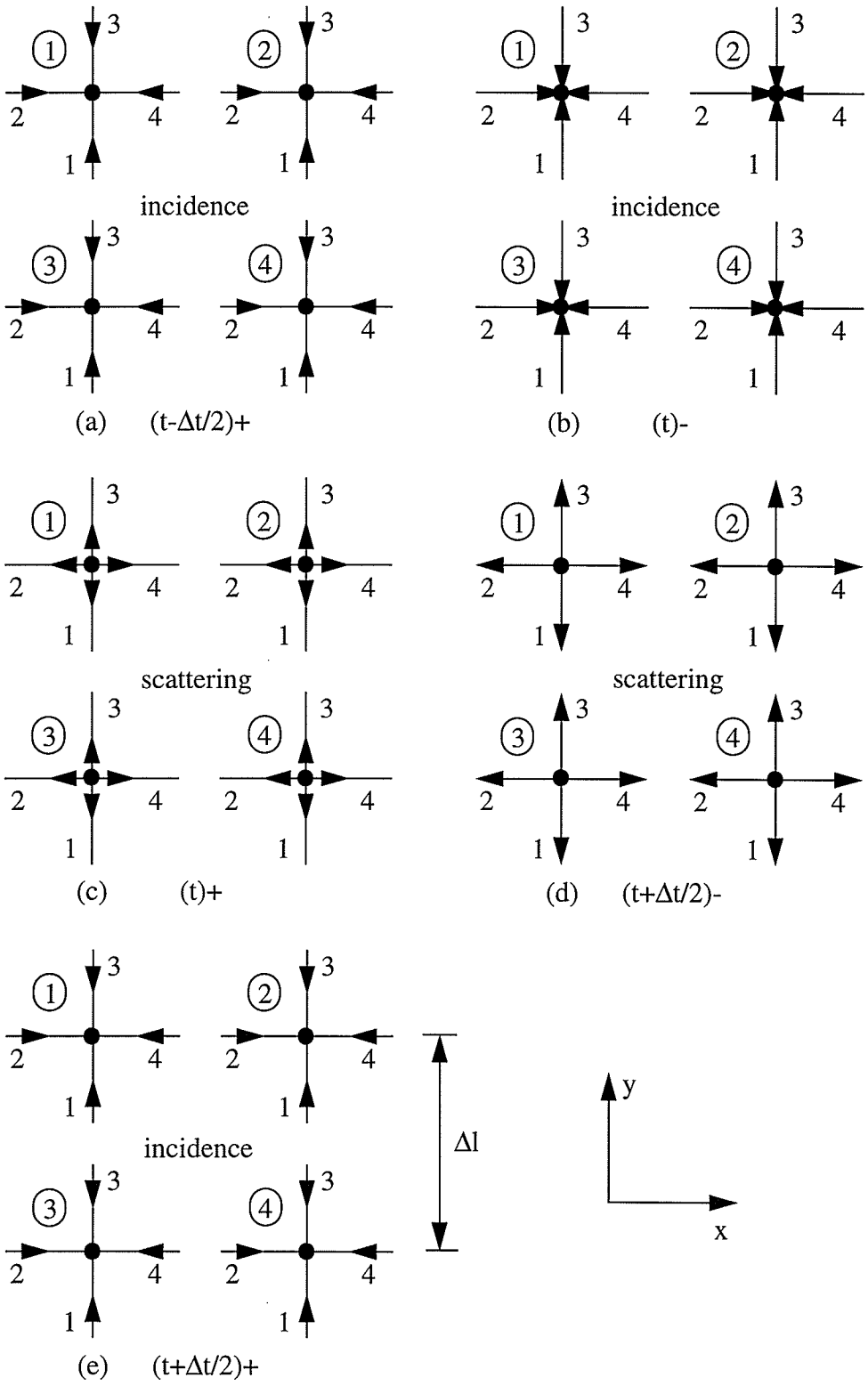

Note: (t)+ and (t)- signify time just before and after time t, respectively

Figure 2.4: Incidence and scattering of the two-dimensional TLM algorithm [3]

$$\begin{bmatrix} v_1^r \\ v_2^r \\ v_3^r \\ v_4^r \end{bmatrix}^t = \frac{1}{2}\begin{bmatrix} -1 & 1 & 1 & 1 \\ 1 & -1 & 1 & 1 \\ 1 & 1 & -1 & 1 \\ 1 & 1 & 1 & -1 \end{bmatrix}\begin{bmatrix} v_1^i \\ v_2^i \\ v_3^i \\ v_4^i \end{bmatrix}^t \tag{2.34}$$

and the transfer events are given by:

$$v_1^{i,t+1}(i,j) = v_3^{r,t}(i,j-1) \tag{2.35}$$

$$v_2^{i,t+1}(i,j) = v_4^{r,t}(i-1,j) \tag{2.36}$$

$$v_3^{i,t+1}(i,j) = v_1^{r,t}(i,j+1) \tag{2.37}$$

$$v_4^{i,t+1}(i,j) = v_2^{r,t}(i+1,j) \tag{2.38}$$

The superscripts i and r denote incident and reflected voltage pulses, respectively. The superscript t corresponds to the discrete time step, and the n in each v_n refers to the branch number (as illustrated in Figure 2.4). The operations (2.34)-(2.38) are executed for every node within the mesh.

Figure 2.4(a) shows that at time (t-Δt/2)+, the voltage pulses move toward the branches. The voltage pulses travel with a velocity $v_l = \Delta l/\Delta t$, and therefore reach the centre of the nodes at time t. Time (t)- is illustrated in Figure 2.4(b). The change between (t)- and (t)+ is a scattering event, as given by (2.34). The incident voltage pulses at time (t)- scatter from the node centre and are represented by reflected voltage pulses at time (t)+. The reflected pulses at time (t)+ are illustrated in Figure 2.4(c). The reflected voltage pulses reach the node centre at time (t+Δt/2). The transformation from time (t+Δt/2)- to

$(t+\Delta t/2)+$ is due to the transfer event given by (2.35) - (2.38). The new reflected voltage pulses at time $(t+\Delta t/2)-$ are transferred to surrounding nodes and become the incident voltage pulses at time $(t+\Delta t/2)+$. The scattered pulses for $(t+\Delta t/2)-$ are illustrated in Figure 2.4(d) and the incident pulses for $(t+\Delta t/2)+$ are illustrated in Figure 2.4(e).

2.2.2 Material Regions

In order to represent regions with arbitrary material properties within the simulation space, transmission line stubs are added to the homogeneous model [17]. Following [16], the modified rectangular model with permittivity and conductivity stubs, is illustrated in Figure 2.5. The permittivity stub is an open-circuit terminated transmission line of characteristic admittance Y_o and length $\Delta l/2$.

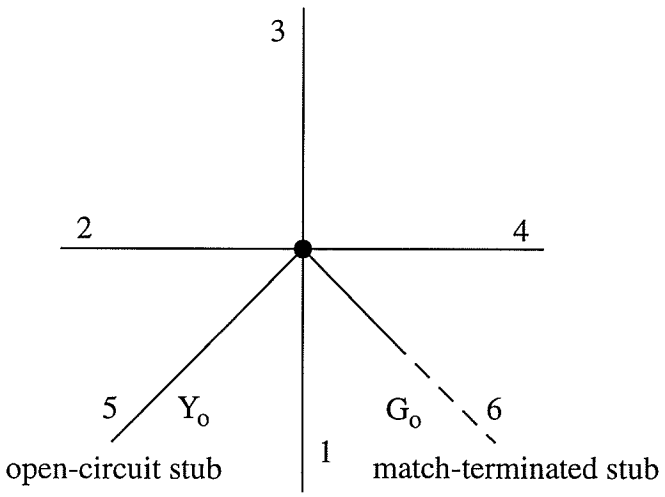

Figure 2.5: Modified rectangular model with permittivity and conductivity stubs [16]

The scattering event which includes the effect of the permittivity stubs is given by:

$$\begin{bmatrix} v_1^r \\ v_2^r \\ v_3^r \\ v_4^r \\ v_5^r \end{bmatrix}^t = \left[\frac{1}{Y} \begin{bmatrix} 1 & 1 & 1 & 1 & \mathrm{Yo} \\ 1 & 1 & 1 & 1 & \mathrm{Yo} \\ 1 & 1 & 1 & 1 & \mathrm{Yo} \\ 1 & 1 & 1 & 1 & \mathrm{Yo} \\ 1 & 1 & 1 & 1 & \mathrm{Yo} \end{bmatrix} - \mathrm{I} \right] \begin{bmatrix} v_1^i \\ v_2^i \\ v_3^i \\ v_4^i \\ v_5^i \end{bmatrix}^t \tag{2.39}$$

where $Y=4+Y_o$ and I is the unit matrix. The transfer event is given by:

$$v_1^{i,t+1}(i,j) = v_3^{r,t}(i,j-1) \tag{2.40}$$

$$v_2^{i,t+1}(i,j) = v_4^{r,t}(i-1,j) \tag{2.41}$$

$$v_3^{i,t+1}(i,j) = v_1^{r,t}(i,j+1) \tag{2.42}$$

$$v_4^{i,t+1}(i,j) = v_2^{r,t}(i+1,j) \tag{2.43}$$

$$v_5^{i,t+1}(i,j) = v_5^{r,t}(i,j) \tag{2.44}$$

For every step in time, a segment of energy incident on the node is transmitted into the permittivity stub in the form of a transmitted voltage pulse. At the next time step, the transmitted voltage pulse is returned with the same polarity (open-circuit termination). The permittivity stub's function is to reduce the macroscopic wave propagation velocity.

The conductivity stub (also illustrated in Figure 2.5) is a match-terminated transmission line with a characteristic admittance G_o. The scattering event which includes the effect of both the permittivity and the conductivity stubs is given by:

$$\begin{bmatrix} v_1^r \\ v_2^r \\ v_3^r \\ v_4^r \\ v_5^r \end{bmatrix}^t = \left[\frac{1}{Y} \begin{bmatrix} 1 & 1 & 1 & 1 & \mathrm{Yo} \\ 1 & 1 & 1 & 1 & \mathrm{Yo} \\ 1 & 1 & 1 & 1 & \mathrm{Yo} \\ 1 & 1 & 1 & 1 & \mathrm{Yo} \\ 1 & 1 & 1 & 1 & \mathrm{Yo} \end{bmatrix} - \mathrm{I} \right] \begin{bmatrix} v_1^i \\ v_2^i \\ v_3^i \\ v_4^i \\ v_5^i \end{bmatrix}^t \tag{2.45}$$

where $Y=4+Y_o+G_o$. The transfer event is the same as for the permittivity stub. Similar to the permittivity stub, a segment of the energy incident on the node is transmitted into the conductivity stub in the form of a transmitted voltage pulse. The energy pulse is not returned to the node ($v_6^r=0$), since the conductivity stub is match-terminated. The conductivity stub has a macroscopic effect of reducing the amount of energy present in the TLM mesh at each time step.

The material parameters with conductivity and permittivity stubs [17] are given as:

$$\varepsilon_r = 1 + \frac{Y_o}{4}, \quad \mu_r = 1, \quad \sigma = \frac{G_o}{\Delta l} \tag{2.46}$$

Using Y_o and G_o, either lossless or lossy dielectrics can be simulated. The dielectric is lossless when $G_o=0$.

2.2.3 Boundary Conditions

Boundary conditions consisting of lossless electric conductors, perfect magnetic conductors, and a type of absorbing local arbitrary boundary condition can be implemented with the TLM method. A boundary condition is enforced by terminating the transmission lines with reflection coefficients half-way between two node centres.

There are two similar techniques which can be utilized to determine the proper

reflection coefficient at a given boundary. One technique is based on the intrinsic impedance of the boundary. The second technique is defined by the field components tangential to the boundary. Figure 2.6 is an illustration of the boundary conditions located half-way between two node centres.

The operation of the boundary condition is as follows. An incident voltage pulse v^i travels in the +x direction (t-), and reflects off the boundary (t), which causes a voltage pulse of magnitude Γv^i to travel in the -x direction (t+).

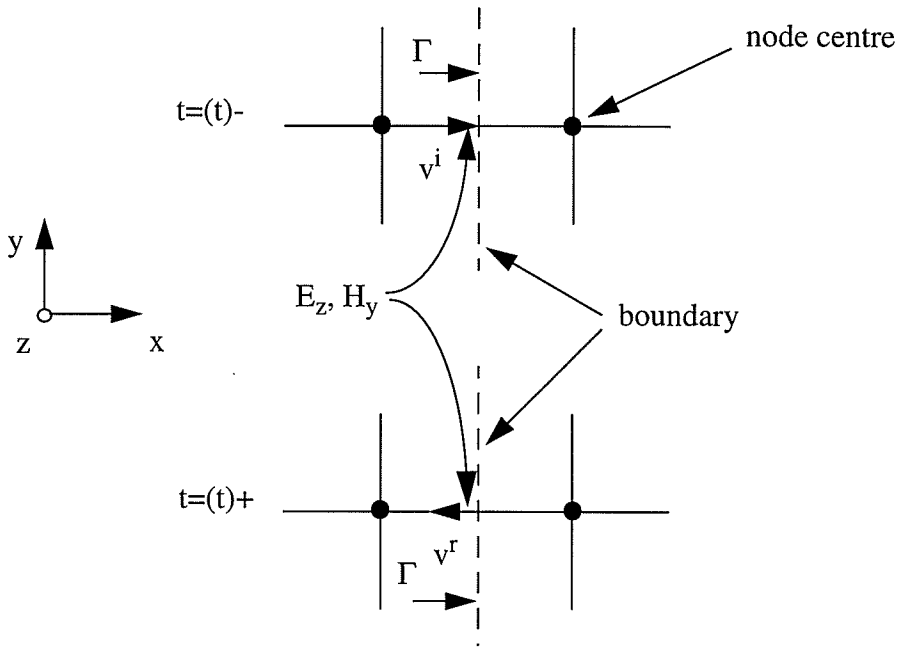

Figure 2.6: TLM boundary condition enforcement using reflection coefficients [16]

2.2.4 Results Attainable from the TLM Algorithm

This section describes how the *E* and *H* fields can be determined from the voltage pulses discussed in the earlier TLM sections.

The TLM method is capable of supporting transmission lines; thus, TEM waves

can propagate in an x-y geometry. The electric and magnetic fields can be found in terms of a voltage pulse v travelling in the x-y plane and in a direction **d**. The E and H fields are as follows:

$$E_z \, \alpha \, v \tag{2.47}$$

$$H_k \, \alpha \, \frac{v}{Z_l} \tag{2.48}$$

where the k component of the magnetic field is given by $\mathbf{d} \times \mathbf{z}$. Examining Figure 2.4, the directions that the energy can propagate are in ±x and ±y. The pulses which travel in the + and - x directions have the following field components, respectively:

$$E_z, -H_y \quad \text{and} \quad E_z, +H_y \tag{2.49}$$

The pulses which travel in the + and - y directions have the following field components, respectively:

$$E_z, +H_x \quad \text{and} \quad E_z, -H_x \tag{2.50}$$

Now that the electric and magnetic field components have been determined, the voltage pulse components can be combined with the electromagnetic fields. In order to determine field quantities, more than a single pulse is required; generally an arbitrary field distribution cannot be represented by a single TEM entity.

Unlike the previous calculations, which were performed at half time steps, the following calculations are performed for even time steps ($n\Delta t$), where the voltage pulses are at the node centres. The electromagnetic fields at the centres of the nodes at even time steps (just before a scattering event ($n\Delta t$)-) are given by:

$$E_z^{n\Delta t}(n_x\Delta l, n_y\Delta l) = \frac{1}{2}\left(v_1^i + v_2^i + v_3^i + v_4^i\right) \tag{2.51}$$

$$H_x^{n\Delta t}(n_x\Delta l, n_y\Delta l) = \frac{1}{Z_l}\left(v_1^i - v_3^i\right) \tag{2.52}$$

$$H_y^{n\Delta t}(n_x\Delta l, n_y\Delta l) = \frac{1}{Z_l}\left(v_4^i - v_2^i\right) \tag{2.53}$$

The v_n^i pulses centre on the node at $(n_x\Delta l, n_y\Delta l)$.

The fields half-way between the node centres at half time steps (just before a transfer event ((n+1/2)Δt)-) are given by:

$$E_z^{\left(n+\frac{1}{2}\right)\Delta t}\left(\left(n_x+\frac{1}{2}\right)\Delta l, n_y\Delta l\right) = v_2^i + v_4^i \tag{2.54}$$

$$H_y^{\left(n+\frac{1}{2}\right)\Delta t}\left(\left(n_x+\frac{1}{2}\right)\Delta l, n_y\Delta l\right) = \frac{1}{Z_l}\left(v_2^i - v_4^i\right) \tag{2.55}$$

where the voltage pulse v_2^i belongs to the node centered at $((n_x+1)\,\Delta l, n_y\Delta l)$ and v_4^i belongs to $(n_x\Delta l, n_y\Delta l)$. Finally, the voltage pulse v_1^i belongs to the node centered at $(n_x\Delta l, n_y\Delta l)$ and v_3^i belongs to $(n_x\Delta l,\ (n_y+1)\,\Delta l)$:

$$E_z^{\left(n+\frac{1}{2}\right)\Delta t}\left(n_x\Delta l, \left(n_y+\frac{1}{2}\right)\Delta l\right) = v_1^i + v_3^i \tag{2.56}$$

$$H_x^{\left(n+\frac{1}{2}\right)\Delta t}\left(n_x\Delta l, \left(n_y+\frac{1}{2}\right)\Delta l\right) = \frac{1}{Z_l}\left(v_3^i - v_1^i\right) \tag{2.57}$$

Given only equations (2.51)-(2.53), the electric and magnetic fields are overconstrained in terms of voltage pulses. However, with equations (2.54)-(2.55) and (2.56)-

(2.57), the electric and magnetic fields can be enforced at half time steps.

2.3 Summary

In this chapter a brief description of the modal expansion method and the TLM method is provided. These two tools are utilized in the thesis research for the design of antenna and transmission line structures. In the following chapters, the results obtained from these simulation tools are compared to experimental results.

Chapter 3:

Coupling Energy through a Slot in a Thick Ground Plane

The purpose of this chapter is to investigate how effectively energy can couple through a slot in a thick ground plane. The results demonstrate the change in performance of aperture-coupled devices for various ground plane thicknesses. A minimum practical ground plane thickness would be approximately 0.635 mm, which is thick enough to mount an active device to the ground plane surface with a screw.

3.0 Introductory Remarks

A simple approach for establishing the level of coupling is achieved by examining the operation of a two-port aperture-coupled resonant coupler. By fixing a control frequency and stub length, and optimizing the slot dimensions for a number of different ground plane thicknesses, a maximum coupling level can be determined. From this information, optimized slot dimensions can be realized for different ground plane thicknesses.

The time-domain TLM method [see Chapter 2.2] is selected to simulate aperture-coupling through thick ground plane structures. Experiments are conducted on four port couplers with various slot dimensions and substrates to determine the flexibility and reliability of the TLM method. Results from [18] are compared to both TLM and experimental results. Based on the TLM simulation results, a two-port coupler experiment is conducted. Finally, the results from papers [19] and [20] are evaluated, and a conclusion is

made regarding the feasibility of aperture-coupling through a thick ground plane.

3.1 Verification of the TLM Method's Results

The validity of the numerical method is established in two ways. The first utilizes the results from [18] for a 50 Ω line-to-line coupling through a common thick ground plane (at approximately 5 GHz). This includes experimental and computational results for an infinitely thin ground plane, and computational results for a ground plane of finite thickness. These results are compared to TLM method and experimental results. In the second, an experiment is conducted on a modified structure operating at approximately 20 GHz. The TLM computations are validated through comparison with the experimental results.

The four-port 50 Ω line-to-line coupling structure is shown in Figure 3.1. In the numerical simulations, a magnetic wall is placed along the centre of the transmission line to reduce simulation time by a factor of two (i.e., the y-plane was reduced by a factor of two). Results with and without a magnetic wall are found to be identical. The structure shown in Figure 3.1 cannot be used in experimental testing, due to the problem of mounting the connectors. Therefore, the transmission lines are fabricated in such a way that four connectors may be added to the structure, following [21], which also states that the curved transmission lines are found to produce some mismatches. Figure 3.2 illustrates the layout of the experimentally measured line-to-line coupler.

The experimental measurements are initially done using a TRL calibration. A TRL calibration should be executed with only two connectors in order to de-embed their mismatches. However, in the actual calibration, nine connectors are used. The coupler

under test contains four connectors, the THRU and LINE calibration set each contains two connectors, and the REFLECT calibration piece contains one connector. Because of the large number of connectors, many errors are introduced into the calibration and the results are poor.

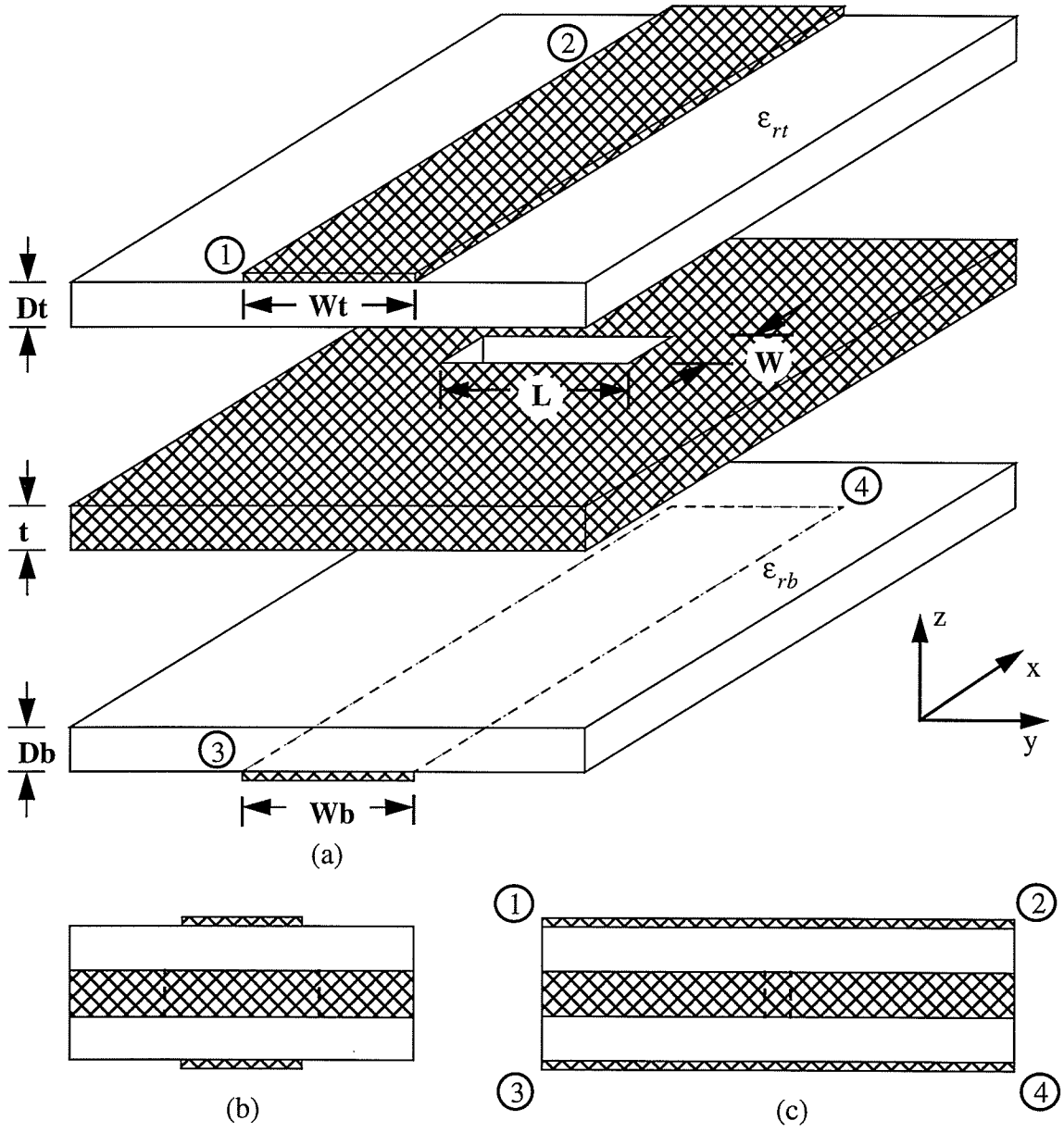

Figure 3.1: Line-to-line coupling through a thick ground plane (four-port 50 Ω structure) (a) 3-D View, (b) End View, (c) Side View

Thus, a coaxial calibration is performed instead. First, the insertion loss of a 50 Ω

microstrip transmission line of a length equal to the coupler length (i.e., transmission line length between port 1 and port 2, as seen in Figure 3.2) is measured. These losses are then subtracted from the coupler measurements (in decibels), which gives extremely accurate results. Losses due to the slot are not accounted for.

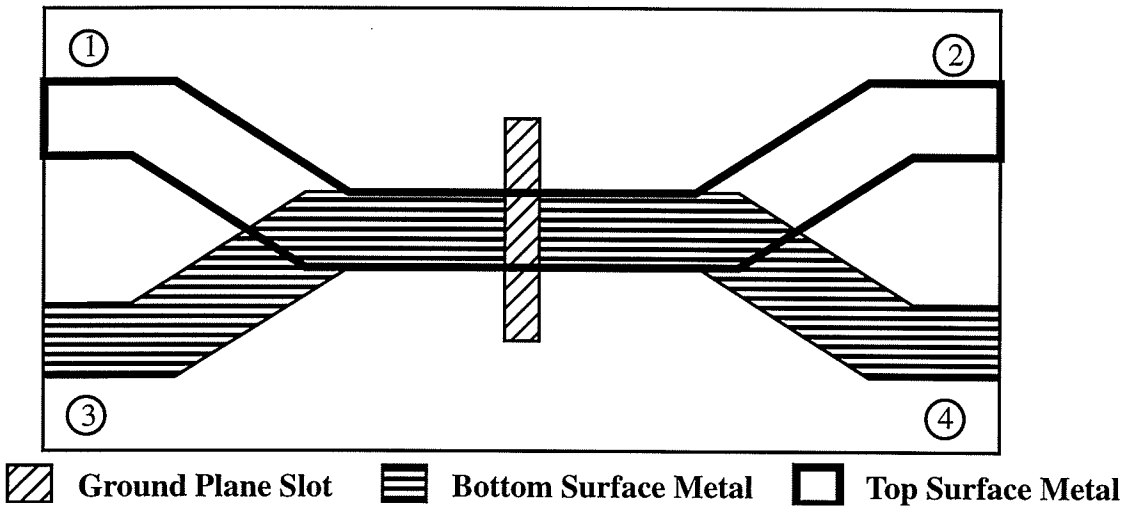

Figure 3.2: Layout of the measured four-port 50 Ω line-to-line coupler

3.1.1 Line-to-Line Coupling using Substrates with a Permittivity of 2.2

The S-parameters of a 50 Ω line-to-line coupler with a thick ground plane are given by [18], and are compared both experimentally and with the TLM method. The simulation space is of size Nx=90, Ny=80, Nz=40; the spatial increment is 0.127 mm; number of iterations is 1500; Wb=Wt=2.54 mm; Db=Dt=0.762 mm; W=1.1 mm; L=15 mm and $\varepsilon_{rb}=\varepsilon_{rt}=2.2$. The ground plane thicknesses evaluated experimentally and with the TLM method are t=0.0 mm, t=0.127 mm, t=0.254 mm, t=0.381 mm and t=0.508 mm for a frequency range from 1.0 GHz to 20.0 GHz. Computational and experimental results for t=0.0 mm and t=0.508 mm are provided in Figure 3.3. Comparing the measured and computed results, the S-parameters are found to agree well. The differences in results for Figure 3.3(a) and Figure 3.3(b) are almost negligible. The electrical thickness difference between the two ground planes is found to be small. Close inspection of the S-parameters indicate that for increasing ground plane thickness, energy coupled through the slot is

increased and the energy flowing into port two decreases. However, the results presented in Section 3.1.2 (for an electrically thick ground plane) indicate that for increasing ground plane thickness, energy coupled through the slot is decreased and the energy flowing into port two increases. For Figure 3.3, the rationalization for the increase in energy coupled through the slot for the thicker ground plane is due to a slightly superior impedance match.

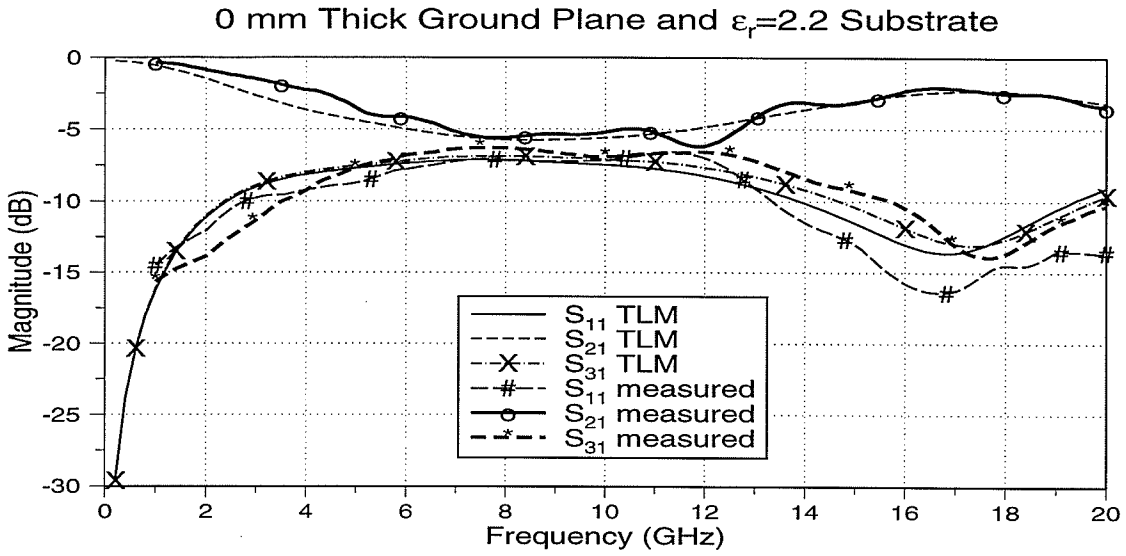

(a)

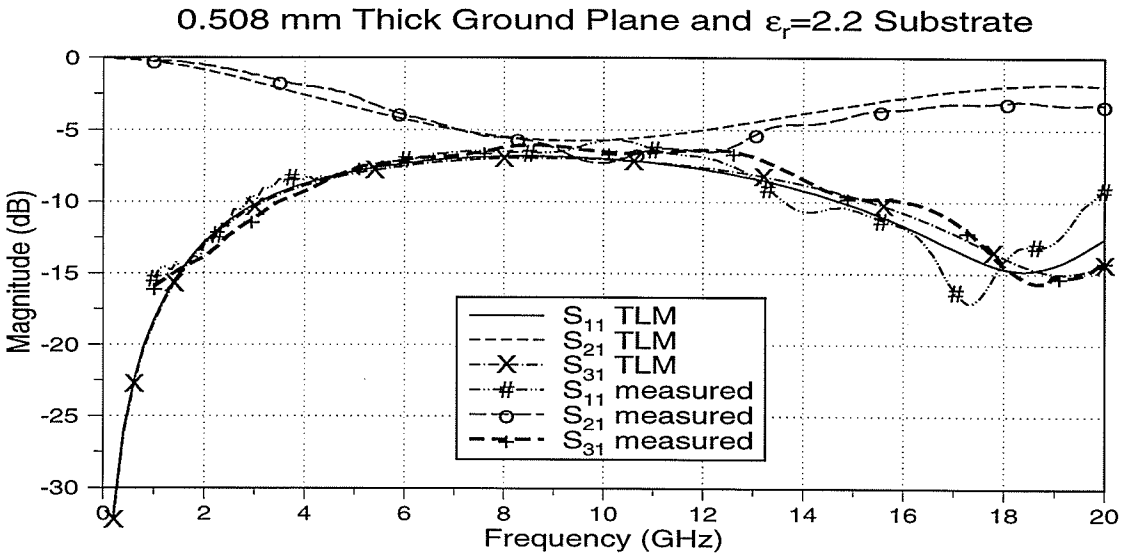

(b)

Figure 3.3: Measured and computed results for a four-port 50 Ω line-to-line coupler with ε_r=2.2.
(a) t=0 mm thick ground plane, (b) t=0.508 mm thick ground plane

3.1.2 Line-to-Line Coupling using Substrates with a Permittivity of 10.2

In the previous section, the TLM method was validated for couplers with low-permittivity substrates and electrically thin ground planes. In this section, various ground plane thicknesses and more typical dielectric constants for the substrates are considered. A practical ground plane thickness is anything greater than 0.635 mm thick (as stated above), and a typical transmission line dielectric constant is approximately 10.2.

The dimensions of an aperture, 50 Ω transmission line, and substrate are given for a typical aperture-coupled microstrip antenna designed for operation at 20 GHz are Wb=Wt=0.264 mm; Db=Dt=0.254 mm; W=0.3 mm; L(t=0.000 mm)=2.700 mm; L(t=0.891 mm)=4.356 mm and $\varepsilon_{rb}=\varepsilon_{rt}=10.2$. The simulation space size is Nx=80, Ny=90, Nz=70; the spatial increment is 0.033 mm and the number of iterations is 2000;

The coupler is simulated for ground plane thicknesses from t=0.0 mm to t=0.891 mm, in 0.127 mm thick increments. As the ground plane thickness increases, the maximum coupling decreases and the frequency of optimum coupling increases. The slot length is increased for the t=0.891 mm case in order to determine the effect on coupling. Coupling similar to the t=0.0 mm case is observed when the slot length is increased by a factor of 1.6. In Figure 3.4, the TLM and experimental results agree within 2 dB for S_{21} and within 4 dB for S_{11} and S_{31} (the measured S-parameter results are smoothed slightly in the figure). The reflections may be due to the bends in the transmission line and to construction tolerances.

Based on the accurate measurements made for two structures with different substrate permittivities, the time domain TLM method is found to be an accurate modelling tool for line-to-line coupling through a thick ground plane.

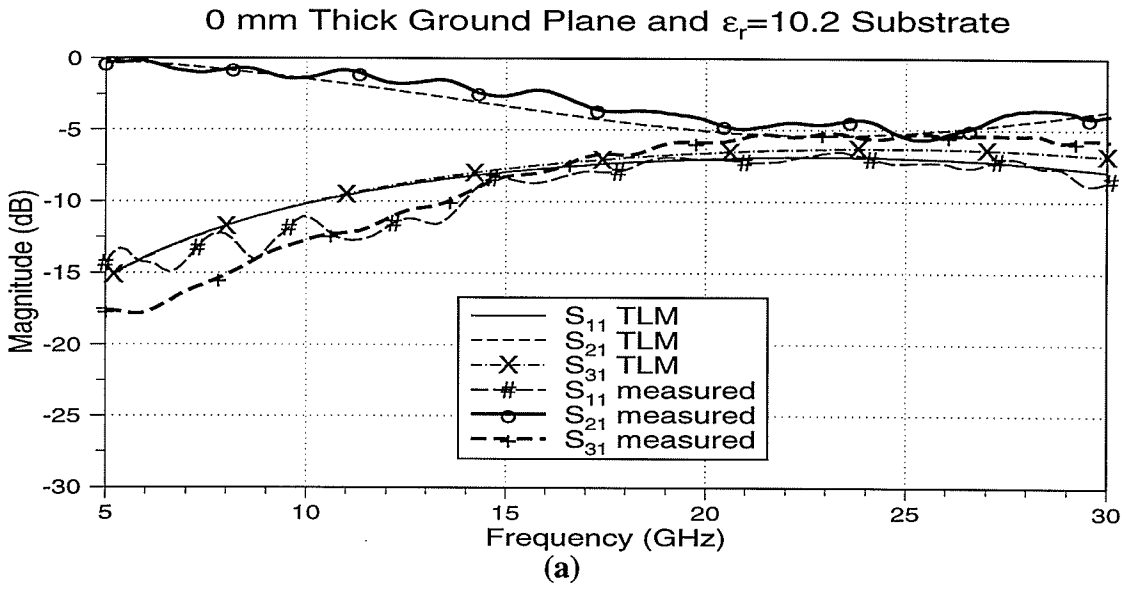

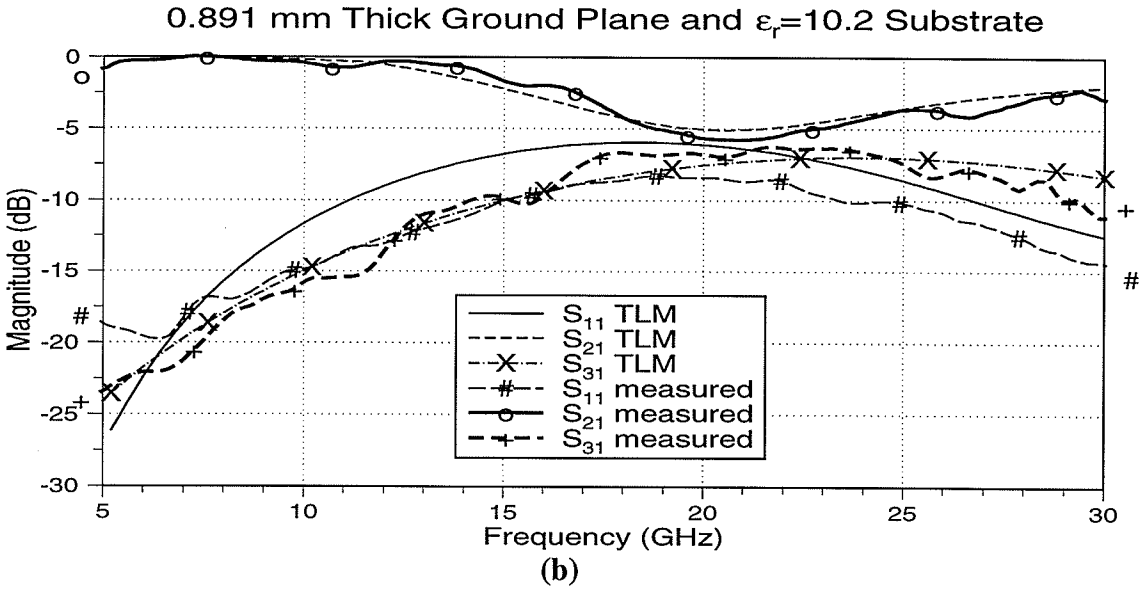

Figure 3.4: Measured and computed results for a four-port 50 Ω line-to-line coupler with ε_r=10.2
(a) t=0 mm thick ground plane, (b) t=0.891 mm thick ground plane

3.2 Optimization of a Two-Port 50 Ω Line-to-Line Slot Coupler with a Thick Common Ground Plane

A two-port coupler is simulated with the TLM method to determine the optimum level of coupling for various thicknesses of ground planes. The two-port coupler with two

open-circuit stubs is illustrated in Figure 3.5

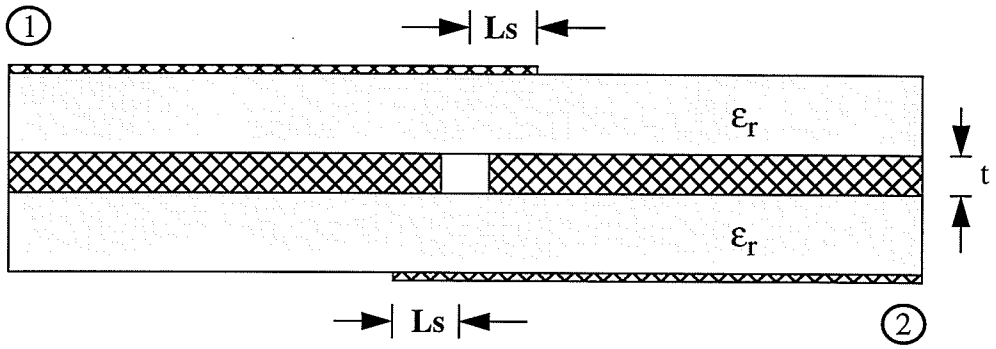

Figure 3.5: Side view of a two-port 50 Ω line-to-line slot coupler with a thick common ground plane

The coupler is optimized for the various ground plane thicknesses by adjusting the slot length and width. The goal of the optimization is to achieve a -20 dB impedance bandwidth centered at approximately 24 GHz. A double resonance is present due to the two open-circuit stubs at the slot. The S_{11} level between the two resonances is maintained between -25 dB to -30 dB. The S-parameters for the coupler with ground plane thicknesses of 0.0 mm, 0.254 mm, 0.508 mm, 0.762 mm, 1.020 mm, 1.270 mm and 1.524 mm are computed, and the graph for the ground plane thickness versus the optimized slot dimensions is presented in Figure 3.6. The ground plane thicknesses of 0.254 mm and 0.762 mm are tested experimentally (as seen further on).

The impedance bandwidth (at -20 dB), centre frequency, S_{21}, and worst S_{11} level between the double resonances are given in Table 3.1. The tabulated results do not include dielectric or copper losses. The results demonstrate that as the ground plane thickness and slot length increase, the slot begins to radiate (i.e., S_{21} decreases). For the coupler simulations, the spatial increment is 0.033 mm, the feed substrate is 0.231 mm thick, the dielectric constant is 10.2, the feedline width is 0.264 mm, and the stub length is 0.650

mm. The simulation space size for the 0 mm case is Nx=80, Ny=70 and Nz=40 with 2500 iterations, and for the 1.524 mm case is Nx=80, Ny=80 and Nz=90 with 4000 iterations.

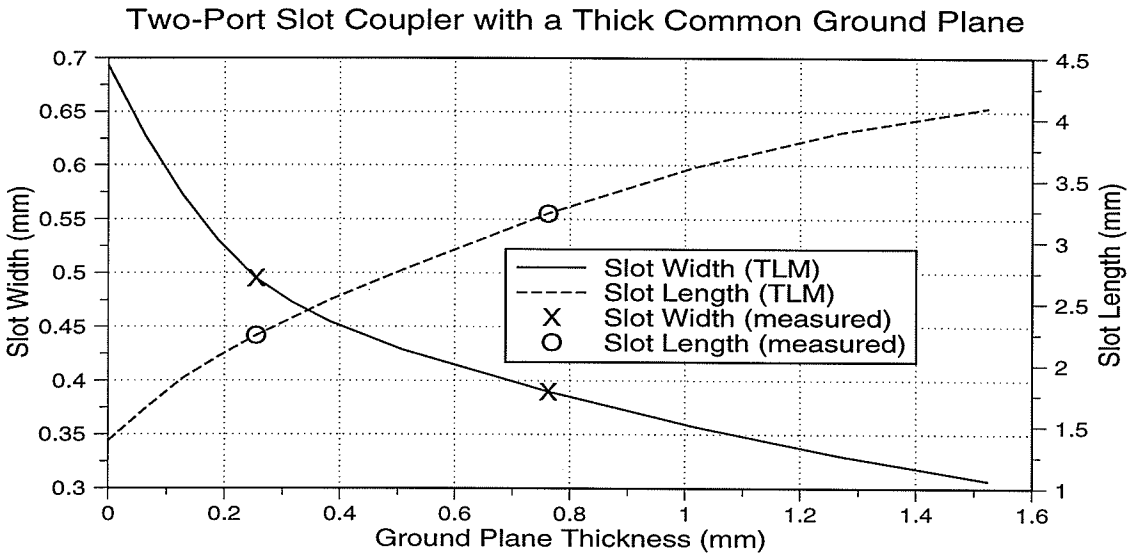

Figure 3.6: Ground plane thickness versus the optimized slot dimensions

Table 3.1: Ground plane thickness versus optimized slot dimension results for a 50 Ω two-port line-to-line coupler

Ground Plane Thickness	Centre Frequency (GHz)	Bandwidth at -20 dB (GHz)	S_{21} (dB)	S_{11} Level (dB)
0.000 mm	23.80	10.2	-0.44	-26.96
0.254 mm	23.60	9.4	-0.44	-27.40
0.508 mm	23.40	9.4	-0.64	-26.12
0.762 mm	24.05	9.9	-0.85	-25.22
1.020 mm	23.45	9.1	-0.94	-24.69
1.270 mm	22.80	8.0	-0.99	-28.18
1.524 mm	24.40	8.8	-1.07	-28.63

One interesting point to note is the rapid decrease of the slot width between ground plane thicknesses of 0 and 0.3 mm. Table 3.1 shows that for ground plane thickness 0 and 0.254 mm there is no change in S_{21}. For thicknesses greater than 0.254 mm, S_{21} starts to

decrease. Therefore, the energy radiated by the slot may have an effect on loading which can be matched by the width of the slot.

The S-parameters are experimentally measured for ground plane thicknesses of 0.254 mm and 0.762 mm. A special jig is constructed to test the structure with minimal adverse interference. Fiberglass clamps are fabricated which fix the transmission line pieces firmly to the ground plane. The clamps also minimize the flexing of the structure during testing. Flexing of the structure may result in a loss of contact between the connector and transmission line.

The S-parameter measurements are performed for ground plane thicknesses of 0.254 mm and 0.762 mm. For a stub length of 0.650 mm, experimental and simulated results do not match well. Therefore, for the 0.254 mm thick case, a stub length of 0.850 mm is used to match the computed results to the experimental results, as seen in Figure 3.7. For the 0.762 mm thick case, a stub length of 0.950 mm is used to match the results.

The measured and computed results for the two-port coupler with a 0.762 mm thick ground plane are illustrated in Figure 3.8. The S_{21} computed and measured results agree quite well. However, the S_{11} computed and experimental results do not agree. A possible explanation for the error may be the relatively coarse mesh used in the TLM analysis in the vicinity of the slot.

The purpose of using a 50 Ω line-to-line coupler is to determine the level of coupling corresponding to the thickness of the ground plane. Using a high-permittivity substrate on both sides of the ground plane may reduce the dimensions of the slot, and thus reduce the energy radiated into free space (resulting in maximum coupling from one line to another). If a high-permittivity substrate is used on one side and a low-permittivity sub-

strate on the other side, the slot is larger and radiates more energy.

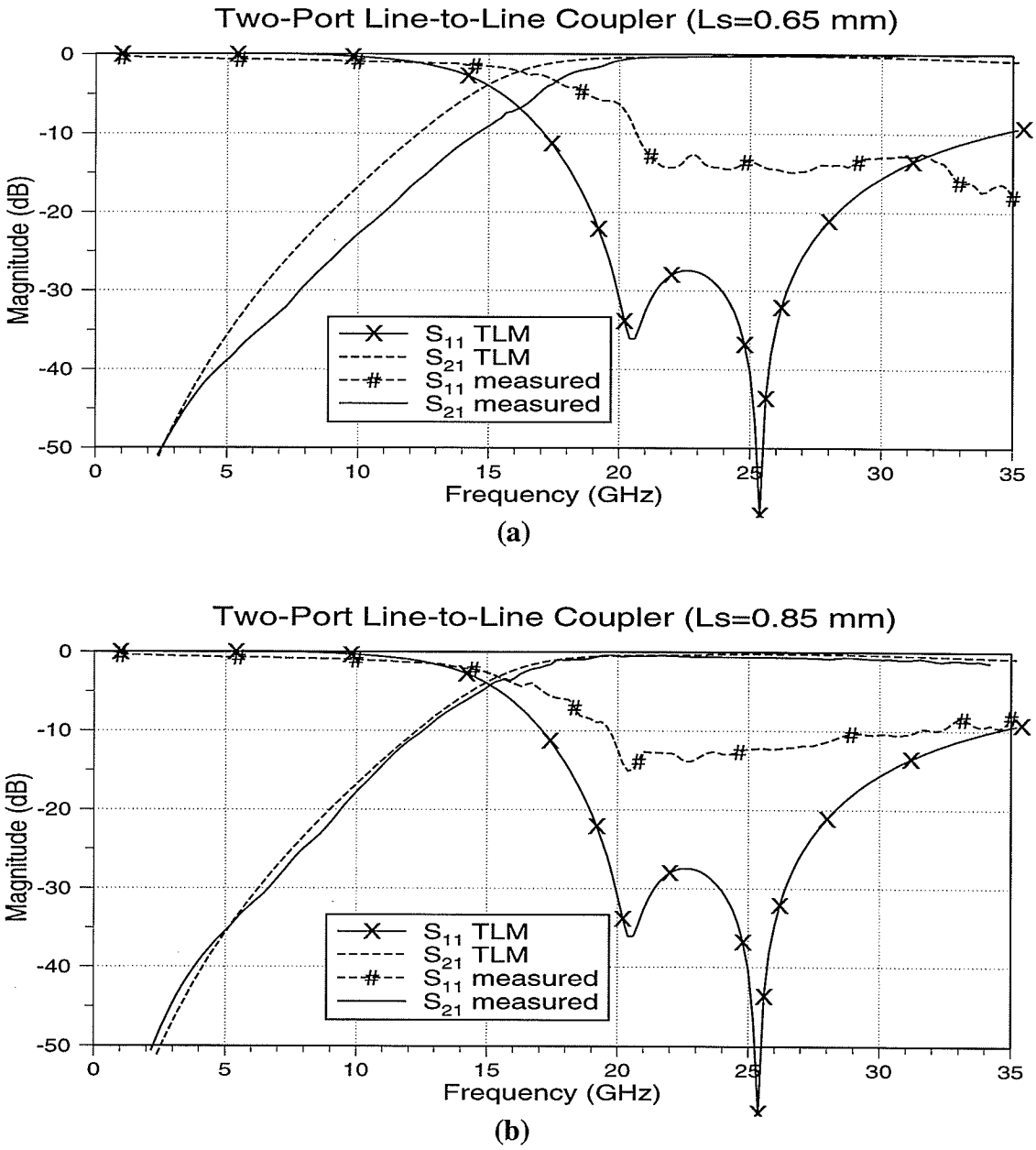

Figure 3.7: Measured and computed results of a 50 Ω two-port line-to-line coupler with a t=0.254 mm thick ground plane (a) Ls=0.65 mm, (b) Ls=0.85 mm

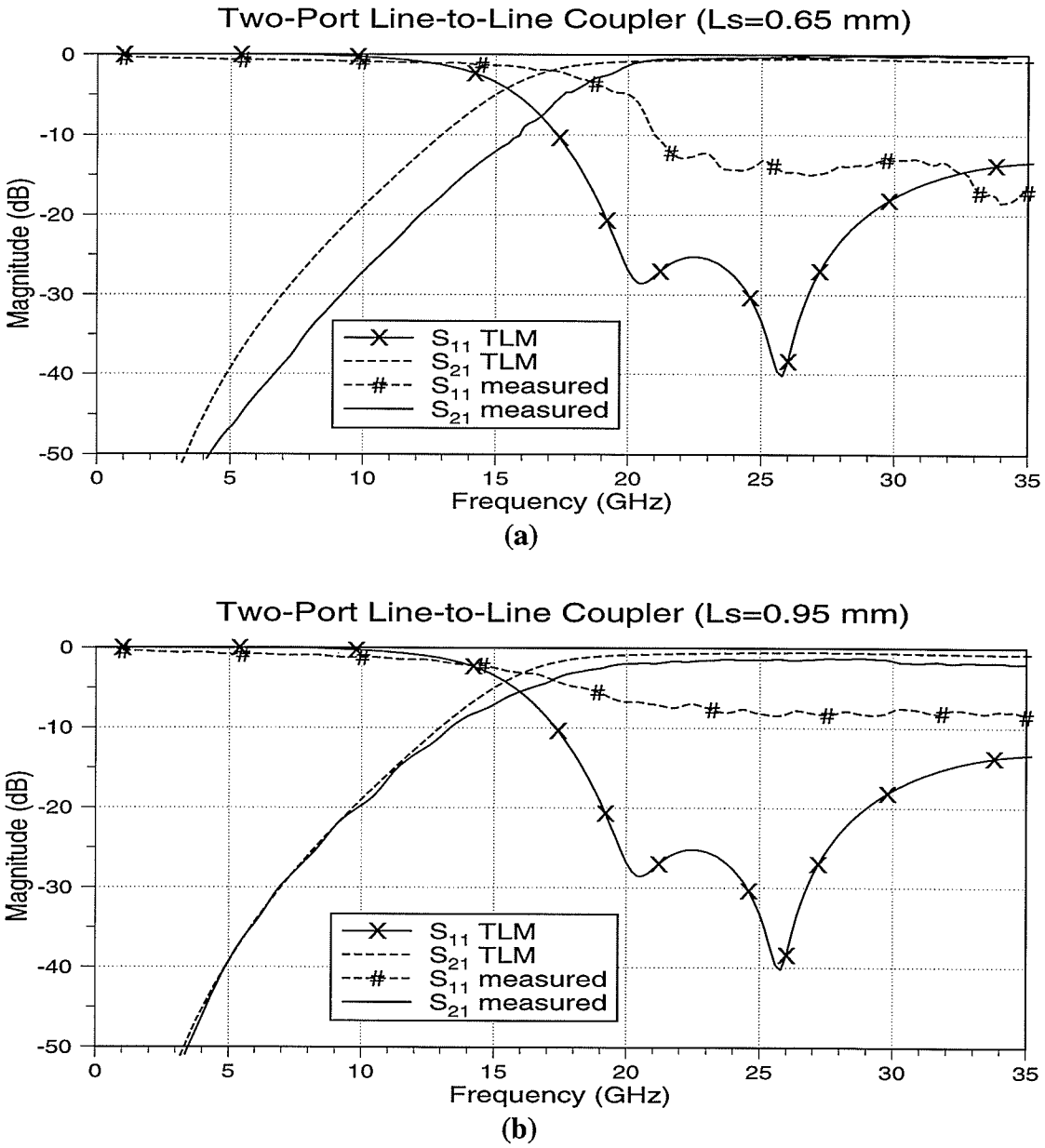

Figure 3.8: Measured and computed results of a 50 Ω two-port line-to-line coupler with a t=0.762 mm thick ground plane (a) LS=0.65 mm, (b) LS=0.95 mm

During the optimization, various S-parameter trends are observed for various slot lengths and widths, at various ground plane thicknesses. Increasing the length of the slot is found to lower the resonance resistance, increase the coupling, and negligibly change the resonant frequency. Increasing the width of the slot is found to decrease the resonant frequency. As the ground plane thickness increases, the bandwidth is found to decrease.

3.3 Comparison of Results with Current Literature

Results for a microstrip patch antenna utilizing aperture-coupling through a thick ground plane are documented in [19] and [20]. These papers present optimized stub and slot dimensions for a thick ground plane. Their goal is to attain a similar level of coupling to an infinitely thin ground plane case.

In [19] and [20], measurements are made to determine the effect of increasing the thickness of the ground plane while maintaining the dimensions of the antenna. The resonant resistance (i.e., when $Re(Z_s)$ is at a maximum) decreases and the resonant frequency increases with increasing thickness. Coupling to the patch is found to drop rapidly (with a decrease of 68%) when $t/\lambda_o = 0.01$. These results coincide with the four-port coupler measurements in Section 3.1.

A disadvantage of the thick ground plane is the decreased level of coupling through the slot. The thick slot acts like a waveguide below cutoff, and in order to minimize the coupling loss, the slot length must be increased to operate above the cutoff frequency.

When the slot length is altered, the resonant frequency, front-to-back lobe radiation, gain, and VSWR are affected [19]. When the ground plane thickness is increased, the front-to-back lobe radiation and gain tend to decrease. The optimization of the antenna, results in an increase in slot length and a decrease in the resonant frequency; as the slot becomes larger, the length approaches resonant frequency and begins to radiate. Therefore, the length of the slot should be maintained below $\lambda_o / 2$ [22].

In [19], aperture-coupled microstrip antenna results show that the ground plane thickness can be increased up to $0.1\ \lambda_o$ while maintaining a front-to-back lobe ratio greater

than 20 dB, with a gain drop of 0.4 dB. The bandwidth is found to drop from 1.4% to 1.1%. The two port coupler measurements (section 3.2) reveal similar results. As the ground plane thickness increases, the coupling through the slot decreases and the impedance bandwidth decreases.

3.4 Summary

In this chapter, aperture-coupling through a thick ground plane is investigated. The TLM method is found to be reasonably accurate by comparing measured and computed results. Four-port and two-port 50 Ω line-to-line couplers are utilized to determine the effect on coupling when the thickness of the ground plane is increased.

Maintaining a high coupling level when a thick ground plane is present is a challenging problem. First of all, a computationally intensive full-wave analysis tool is required to design an aperture-coupled antenna with the thick ground plane. A single patch simulation on a SPARC 10 requires approximately 120 megabytes of RAM and a simulation time of approximately 5 days. Simulating a more complex structure, such as multi-layer patch antenna, requires much more memory and time. Furthermore, at high frequencies between 20 and 30 GHz, the slot becomes difficult to fabricate due to the small width; an EDM (Electro Drilling Machine) required an hour to drill one particular slot through a 0.889 mm thick ground plane. This method does work reasonably well when the slot dimensions are large relative to the ground plane thickness; when the ground plane thickness is 0.254 mm, fairly simple setup and drilling with the EDM can be achieved.

Therefore, since a ground plane thickness of at least 0.635 mm is required, a new method of coupling is chosen (as presented in Chapter 4).

Chapter 4:

Aperture-Coupled Microstrip Antenna Containing a Thick Ground Plane

This chapter examines a novel method of adding a thick ground plane to an aperture-coupled microstrip antenna. In this antenna, a thick sheet of metal containing a dielectric filled cavity is placed between the thin ground plane and the feed substrate. The placement of the cavity is centered directly around the slot in the thin ground plane. The thick sheet of metal acts as a thick ground plane due to the electrical contact with the thin ground plane. The thick ground plane behaves as a heat sink and as a surface on which a LNA (Low Noise Amplifier) can be mounted with screws.

The antenna structure with the thick ground plane and dielectric filled cavity is illustrated in Figure 4.1. The dielectric filled cavity is centered on the slot and a microstrip transition exists where the transmission line crosses over the edge of the cavity. The permittivity of the dielectric filled cavity is chosen to be the same as the transmission line.

4.0 Introductory Remarks

This chapter consists of four sections. The first section examines a microstrip transmission line transition experimentally and with the TLM method. The second section investigates an aperture-coupled microstrip antenna with a thick feed substrate. The third explores the thick ground plane antenna with and without an LNA. The final section investigates system noise temperature and presents G/T ratio results of the active antenna.

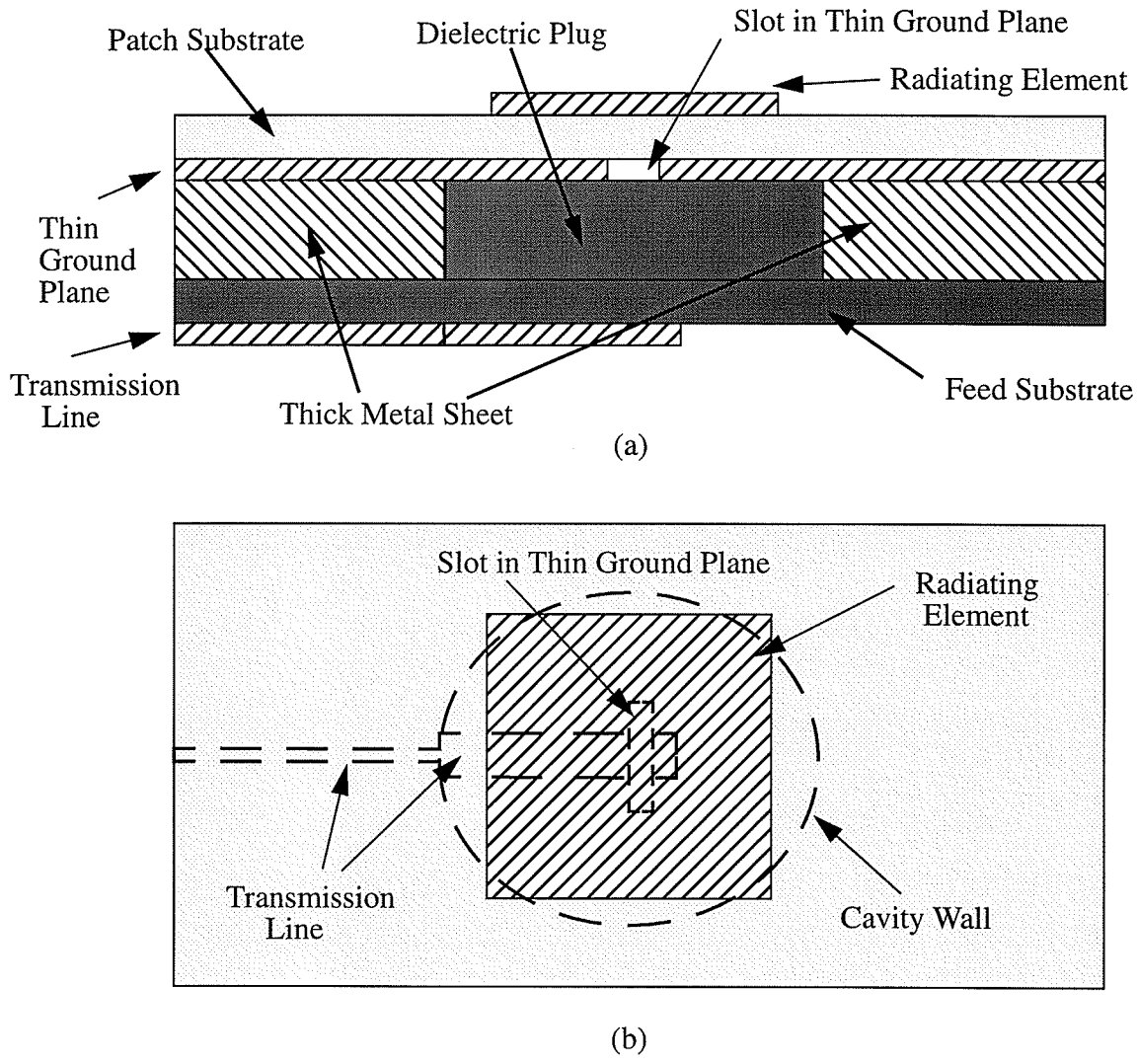

Figure 4.1: Aperture-coupled antenna with a thick ground plane and dielectric filled cavity (a) Side view, (b) Top view

4.1 Microstrip Transmission Line Transition

The purpose of this section is to determine how well a microstrip transmission line transition, illustrated in Figure 4.2, functions. The microstrip structure is an element of the antenna presented in Figure 4.1. The transition is analyzed using the three-dimensional time domain TLM method, which returns the impedance mismatch and insertion

loss.

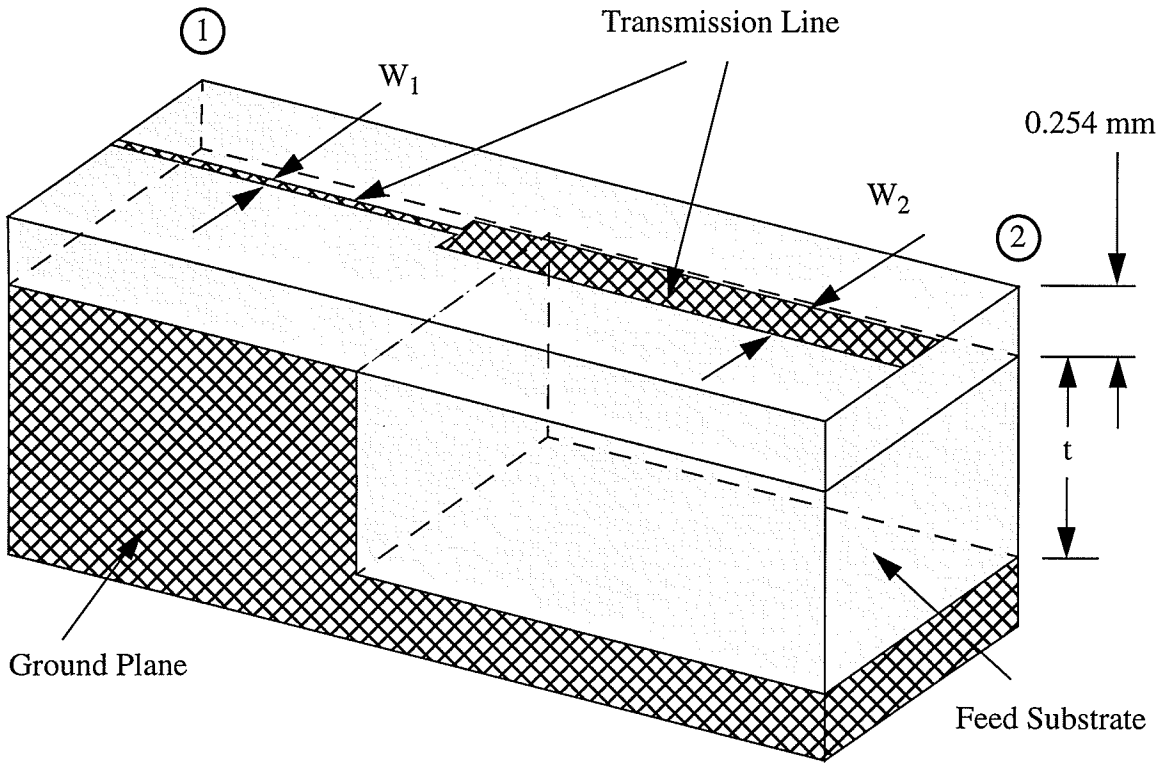

Figure 4.2: Microstrip thin-to-thick-substrate transmission line transition

The ground plane thicknesses analyzed with the TLM method are chosen to be t=0.635 mm and t=0.891 mm. These thicknesses are chosen due to availability of the materials and because a screw could be properly tapped and secured without stripping the threads. The t=0.891 mm thickness is the preferred thickness due to the extra number of threads to hold a screw; on the other hand, the thinner material is more feasible due to a smaller transition.

The thickness of the substrate at W_1 is maintained at 0.254 mm. The transmission line width W_1 is found to be 0.238 mm (using Touchstone™), for a 50 Ω system. The width of the W_2 is found to be 1.045 mm when t is equal to 0.635 mm, for a 50 Ω system.

The width of W_2 is found to be 1.475 mm when t is equal to 0.891 mm. Both of the transitions are analyzed to determine their mismatches and insertion loss.

The size of the simulation space for both cases is Nx=110, Ny=50 and Nz=60; the spatial increment is 0.066 mm; the number of iterations is 1600; the feed substrate at port one is 0.264 mm thick; the dielectric constant is 10.2; and the feedline width at port two is 1.056 mm (over the 0.891 mm thick substrate) and 1.452 mm (over the 1.145 mm thick substrate). The measured and computed results for the transition are illustrated in Figure 4.3.

The experimental S_{11} results match reasonably well with the computed values. However, the S_{21} results are not as accurate between 20 GHz and 30 GHz.

The S-parameter results for the 0.254 mm to 0.891 mm transition, Figure 4.3(a), are found to be much better than those found for the 0.254 mm to 1.145 mm transition, Figure 4.3(b). Also, the thinner substrate transition does not require a matching circuit for frequencies operating below 20 GHz, while the thicker transition requires a matching circuit for frequencies operating above 15 GHz.

A comparable microstrip transition is found in [23], and is referred to as an "abrupt transition". The abrupt transition in [23] is similar to the one illustrated in Figure 4.2, except that the transition in the paper involves multiple substrate layers with varying dielectric constants. The transition in [23] uses a combination of low and high permittivity substrates, which would not be feasible for the microstrip antenna presented in this chapter; a feed substrate with a high dielectric constant is preferred because the cavity containing the substrate can be kept physically small.

The paper also presents a wideband microstrip transition which has a much better

impedance match than the abrupt transition. The wideband transition is physically large and could not be used in microstrip antenna arrays due to size constraints; it requires a much larger cavity in the ground plane than the abrupt transition.

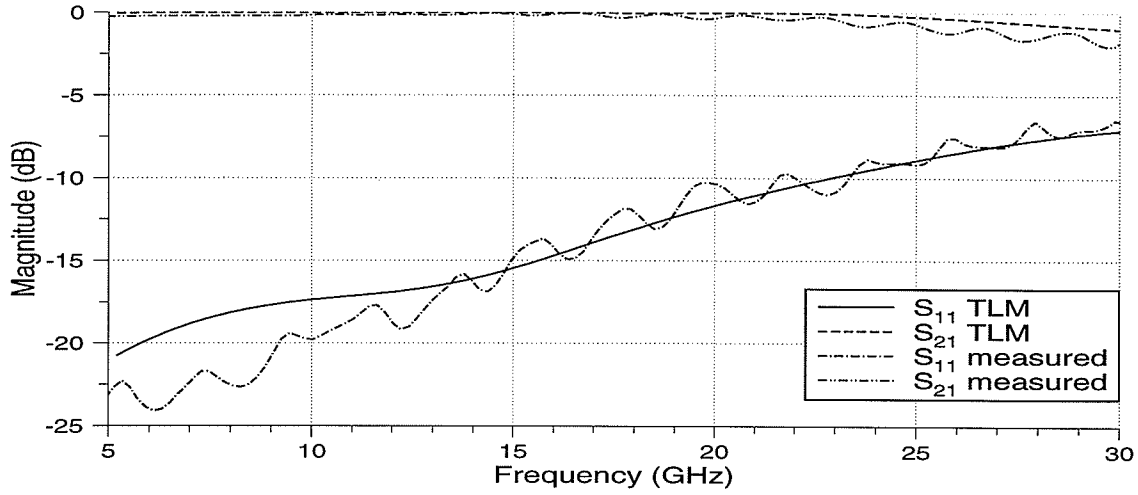

(a)

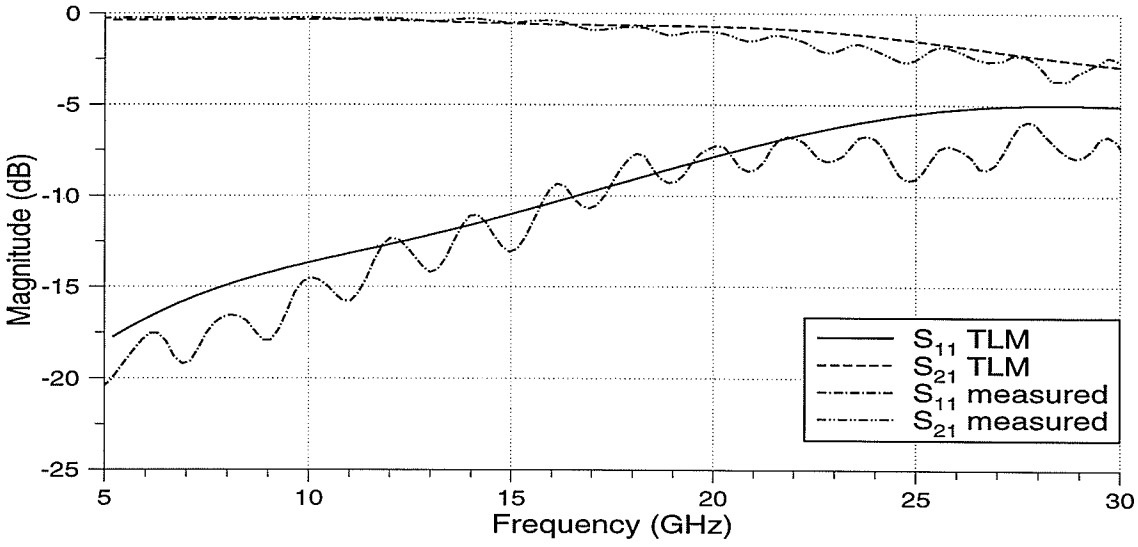

(b)

Figure 4.3: Measured and computed results of a microstrip thin-to-thick-substrate transmission line transition (for a 50 Ω system)
(a) 0.254 mm to 0.891 mm transition (b) 0.254 mm to 1.145 mm transition

4.2 Aperture-Coupled Microstrip Antenna with Thick Feed Substrate

In this section, an aperture-coupled microstrip antenna is designed and tested in order to determine what the patch, slot and transmission line dimensions need to be for an antenna constructed according to Figure 4.1. The aperture-coupled microstrip antenna is designed using the modal expansion method [2]. The cavity walls surrounding the slot and the microstrip transition are assumed to be located an infinite distance away.

The selected substrate for the patch is chosen to be 0.254 mm thick with a permittivity of 2.2. The feed substrates are chosen to be 0.891 mm and 1.145 mm thick with a permittivity of 10.2. The layout of the aperture-coupled microstrip antenna is illustrated in Figure 4.4.

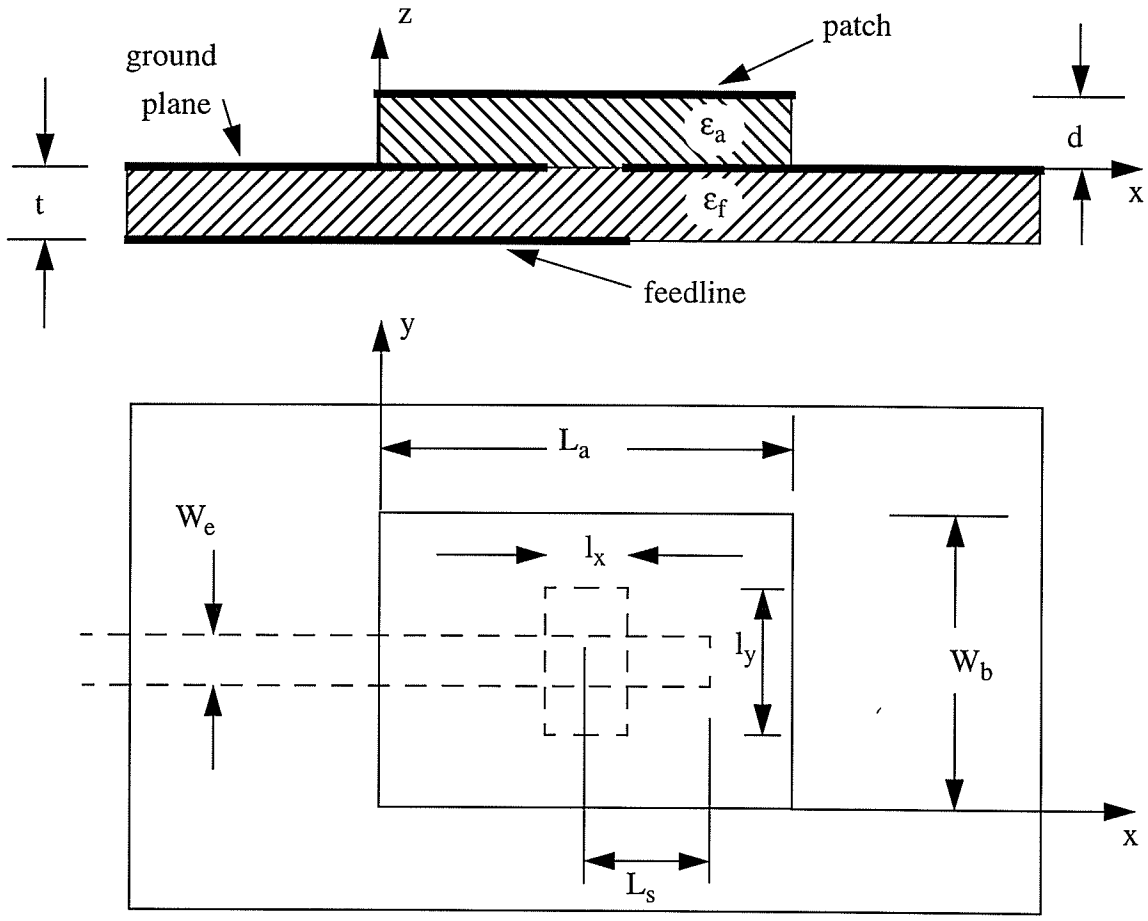

Figure 4.4: Physical layout of the aperture-coupled microstrip antenna

The dimensions of the microstrip antenna for t equal to 0.891 mm and 1.145 mm are given in Table 4.1.

Table 4.1: Physical dimensions of aperture-coupled microstrip antennas

L_a (mm)	W_b (mm)	d (mm)	ε_a	l_x (mm)	l_y (mm)	W_e (mm)	L_s (mm)	t (mm)	ε_f
4.30	4.61	0.254	2.2	0.44	2.35	1.045	0.92	0.891	10.2
4.18	4.70	0.254	2.2	0.25	3.00	1.495	0.82	1.145	10.2

Each antenna is optimized for a centre frequency of 19.70 GHz with the largest possible impedance bandwidth. For the t=0.891 mm case, the computed S_{11} is equal to -28.5 dB at 19.70 GHz and the -10 dB fractional bandwidth is equal to 1.57% (approximately 280 MHz). For the t=1.145 mm case, the computed S_{11} is equal to -27.0 dB at 19.70 GHz and the -10 dB fractional bandwidth is equal to 1.42%.

The aperture-coupled microstrip antenna is a multi-layer antenna. When the antenna is fabricated, the patch and feed substrate must be fastened together; the chosen methods are either nylon screws or bonding film. The only available feed substrates have thicknesses of 0.254 mm and 0.635 mm, and therefore the feed substrates are laminated using the bonding film, which has a thickness of 0.0254 mm and a permittivity of 2.2. For the t=0.891 mm feed substrate, 0.254 mm and 0.635 mm thick substrates are laminated. For the t=1.145 mm feed substrate, two 0.254 mm pieces and a 0.635 mm piece are laminated. The extra thickness and change in permittivity could be possible sources of error when comparing computed and experimental results.

The S-parameters are measured for both the antenna structures assembled with bonding film and those assembled with screws. For the t=0.891 mm case, the antenna fas-

tened with screws is found to have a centre frequency of 18.91 GHz and a -10 dB impedance bandwidth of 2.03%, and the antenna fastened with bonding film is found to have a centre frequency of 19.13 GHz and a -10 dB impedance bandwidth of 2.01%. The layer of film is found to add a 1.4% upwards shift in frequency compared to the antenna fastened with screws. A second resonance occurred, at a frequency 4.89% higher than the operating frequency. The measured S-parameters are illustrated in Figure 4.5. The radiation pattern for the microstrip antenna fastened with screws is illustrated in Figure 4.6.

The 1.145 mm thick feed substrate antennas had measured centre frequencies of approximately 18.6 GHz for both laminated and screwed assembly. Multiple resonances, resulting from higher order modes, occurred periodically after 18.6 GHz. The antennas have a poor impedance match at 18.6 GHz, which is slightly improved with stub tuning. Unfortunately, these antennas are found to be poor radiators (low gain radiation pattern measurement) and are therefore abandoned.

The front and back plane radiation patterns for the antenna are plotted in Figure 4.6. The back plane radiation is 15.2 dB down from the main beam (H-Plane) and 10.8 dB down from the main beam (E-Plane). The back plane radiation is expected to be high due to the wide microstrip transmission line. As the width increases, the stub begins to act as a radiator. For an aperture-coupled microstrip antenna with a electrically thin feed substrate, the front to back plane radiation is approximately 22 dB [10]. The cross-polarization levels are acceptable for both the E- and H-Planes.

The aperture-coupled microstrip antenna with a thick feed substrate is found to function acceptably. The only disadvantage is the high back lobe radiation which reduces the efficiency of the antenna.

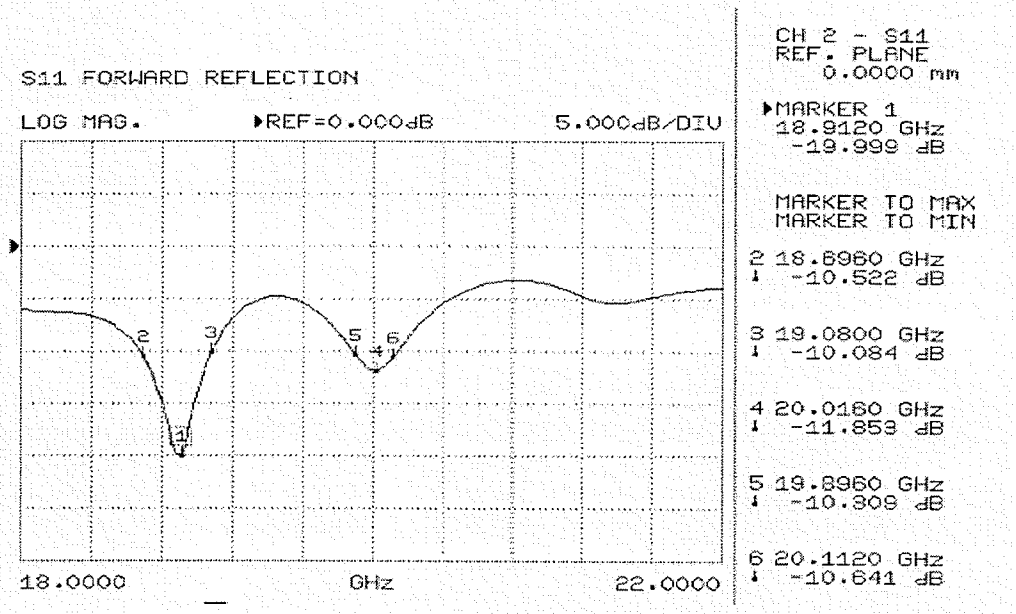

(a)

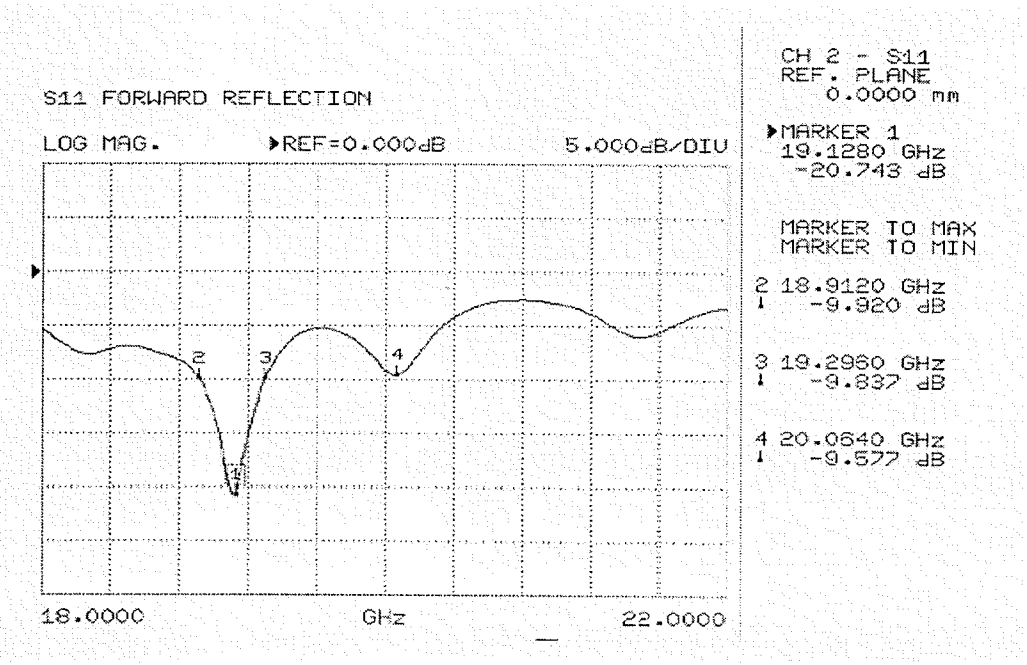

(b)

Figure 4.5: Measured S_{11} for an aperture-coupled microstrip antenna with a thick feed substrate(t=0.891 mm)
(a) structure bonded with screws, (b) structure bonded with film

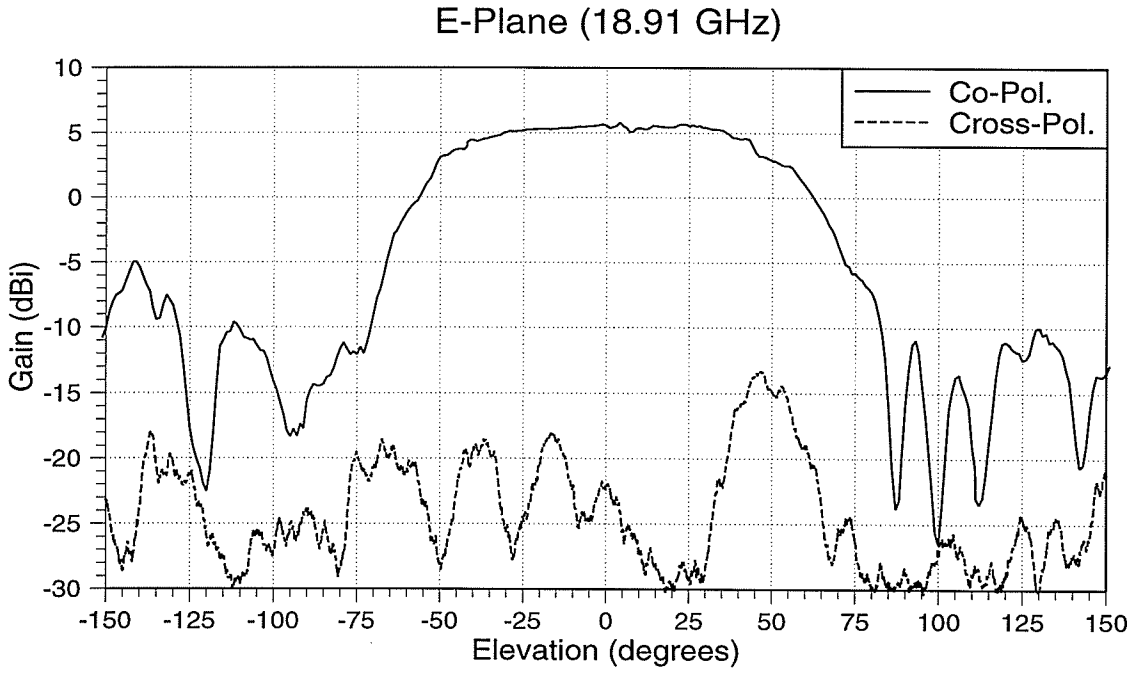

(a)

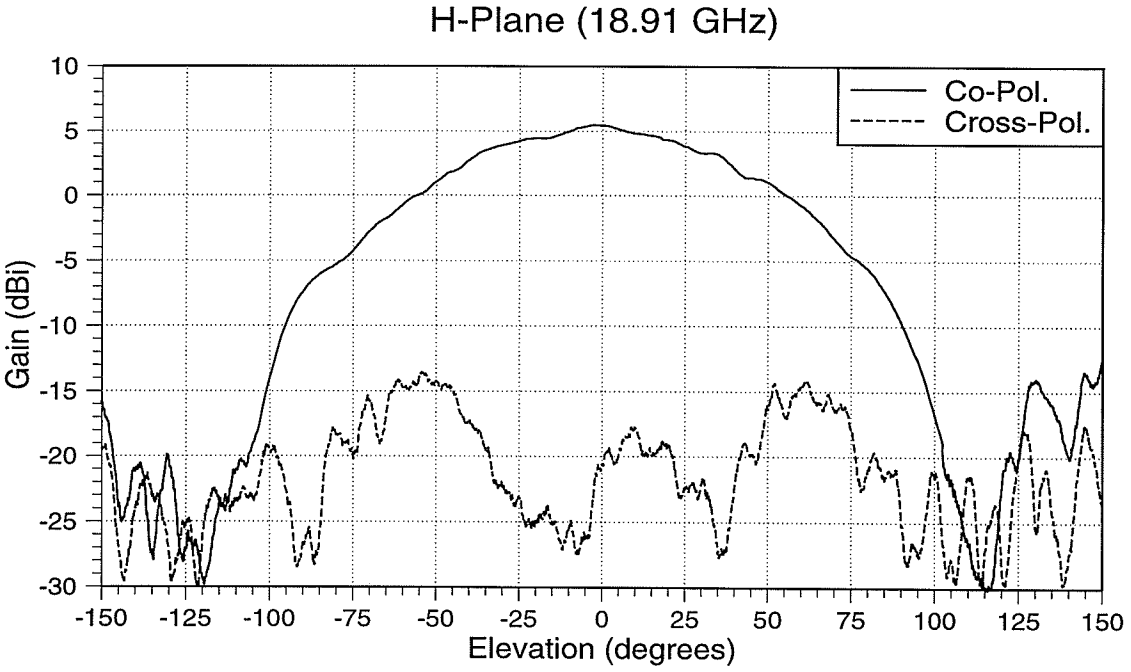

(b)

Figure 4.6: Radiation pattern of an aperture-coupled microstrip antenna with a thick feed substrate (t=0.891 mm)
(a) E-Plane, (b) H-Plane

4.3 Aperture-Coupled Microstrip Antenna Containing a Thick Ground Plane

Since the microstrip transition and microstrip antenna are found to function reasonably well, the two structures can be combined to determine the overall functionality. The thickness of the ground plane is chosen to be 0.635 mm based on the results obtained in sections 4.1 and 4.2.

4.3.1 Square and Circular Dielectric Filled Cavities with a 5 λ_g Diameter

Two brass ground planes are fabricated and are illustrated in Figure 4.7. One ground plane contains a square cavity and the other a circular cavity. The square cavity combined with a transmission line closely resembles the microstrip transmission line transition (see section 4.1). However, a circular cavity is simpler to fabricate than a square cavity; a square cavity requires a milling machine, whereas the circular cavity can be drilled. Also, circular substrate pieces are much simpler to fabricate than square pieces. The results of the antenna with a circular and with a square cavity are compared to determine whether a significant difference in the results occur. In both cases, the diameter of the aperture is selected to be 5 λ_g, which is large enough that the aperture wall does not interact with the slot.

In section 4.2, utilizing bonding film to laminate layers together is found to cause a shift in the operating frequency. Another problem with bonding film is that once the structure is laminated, alterations can no longer be made. An alternative method is to fabricate fiberglass clamps, which hold the patch substrate and transmission line substrate firmly against the ground plane. The fiberglass clamps are illustrated in Figure 4.8. The patch

substrate contains a patch on the top side, while the bottom side contains a ground plane and slot. The transmission line substrate contains the transmission line.

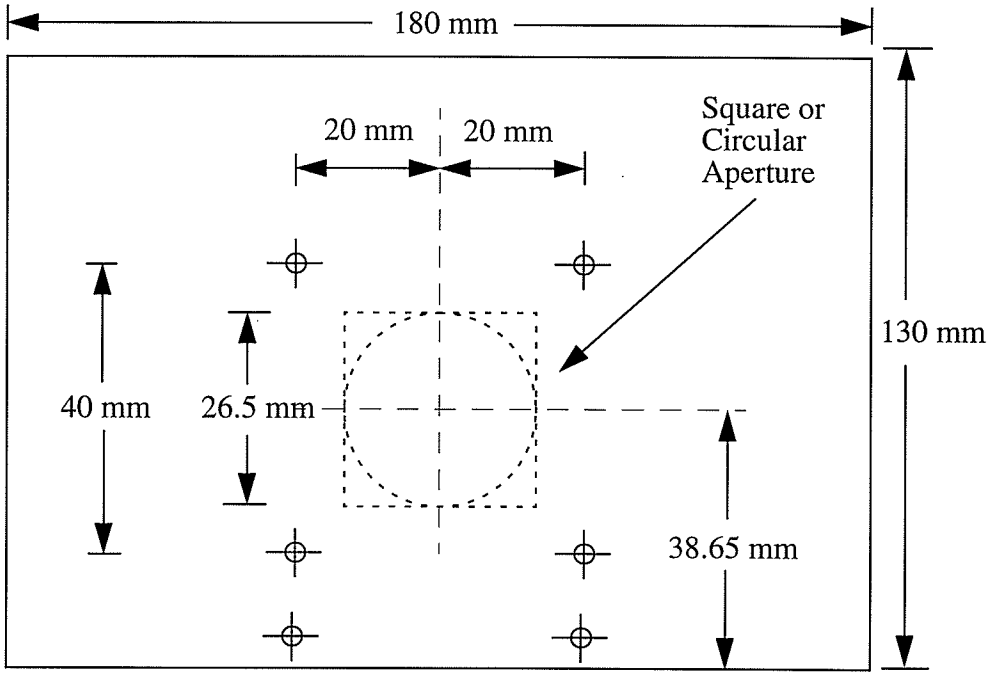

Figure 4.7: Layout of the thick brass ground plane

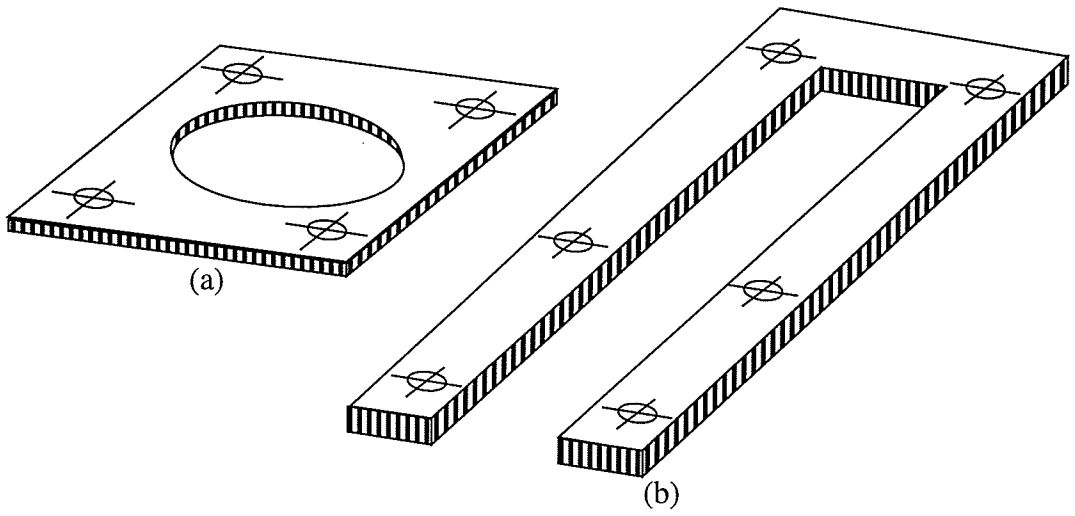

Figure 4.8: Fiberglass substrate clamps
(a) Patch clamp, (b) Transmission line clamp

The patch and transmission line dimensions are as given in Table 4.1 for the t=0.891 mm thick case. The S_{11} results do not agree with Figure 4.5 (a), and therefore a longer stub is required to obtain a good match. For the circular cavity, a double resonance at 18.8 GHz and 19.8 GHz occurs, in which each resonance has a 2.1% (approximately 400 MHz) impedance bandwidth at -10 dB. For the square cavity, a -10 dB impedance bandwidth is maintained from 18.8 GHz to 19.8 GHz. The S-parameters are illustrated in Figure 4.9. Pattern measurements are obtained and an odd 3 dB ripple occurs at broad-side, as illustrated in Figure 4.10. The ripple occurs when the thick ground plane contains either a square cavity or a circular cavity.

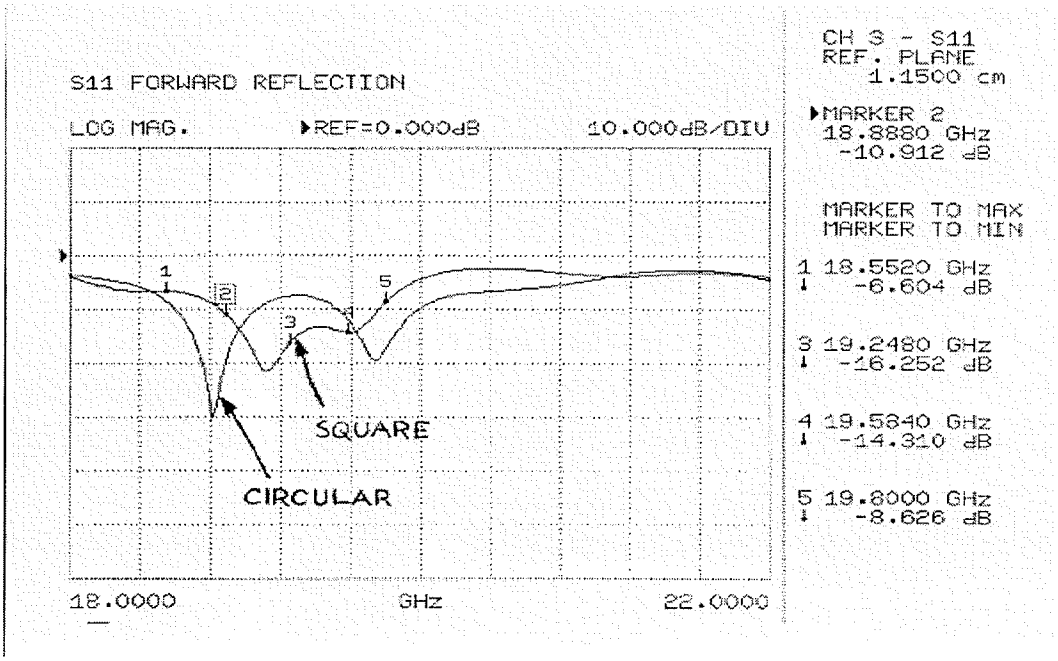

Figure 4.9: Measured S_{11} for the circular and square dielectric filled cavity (where the patch is clamped to the thick brass ground plane)

The results in Figure 4.9 and Figure 4.10 are unacceptable, which are due to poor ground contact between the patch susbtate ground plane and the thick brass ground plane. The 3 dB ripple in the radiation pattern is caused by energy radiating from between the

two conducting surfaces. The radiation pattern is therefore remeasured with the patch substrate and thick brass ground plane bonded with a silver conducting epoxy. In order for the epoxy to cure, the material must bake for 20 minutes at 150° C. All subsequent measurements are made with the patch substrate epoxied to the thick ground plane. The transmission line substrate continues to be fastened with the fiberglass clamp.

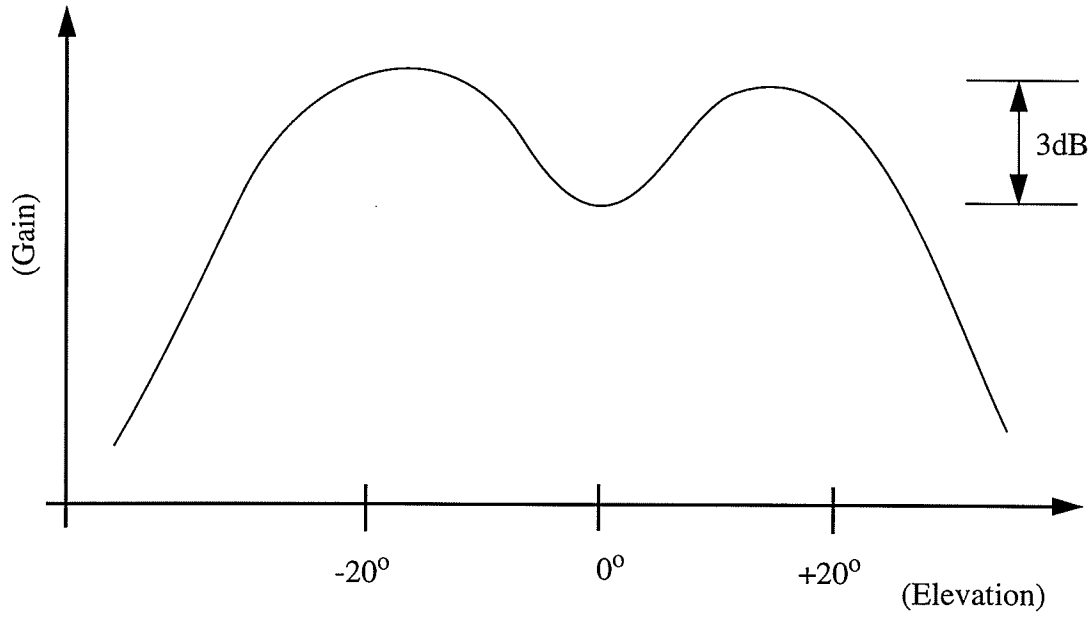

Figure 4.10: Broadside radiation pattern when poor electrical contact exists between the substrate ground plane and thick brass ground plane

The radiation pattern of the microstrip antenna at 19.2 GHz containing a square dielectric filled cavity with a diameter of 5 λ_g is illustrated in Figure 4.11. The radiation pattern of the microstrip antenna containing a circular dielectric filled cavity is almost identical to Figure 4.11. The stub lengths for the two antennas are kept constant. The stub length found to give the best impedance match is Ls = 1.701 mm.

As shown in Figure 4.11, the peak side-lobe radiation is 15.1 dB down from the

main beam (H-Plane) and 10.5 dB down from the main beam (E-Plane). The microstrip antenna with the large dielectric filled cavity is thus found to give reasonable results.

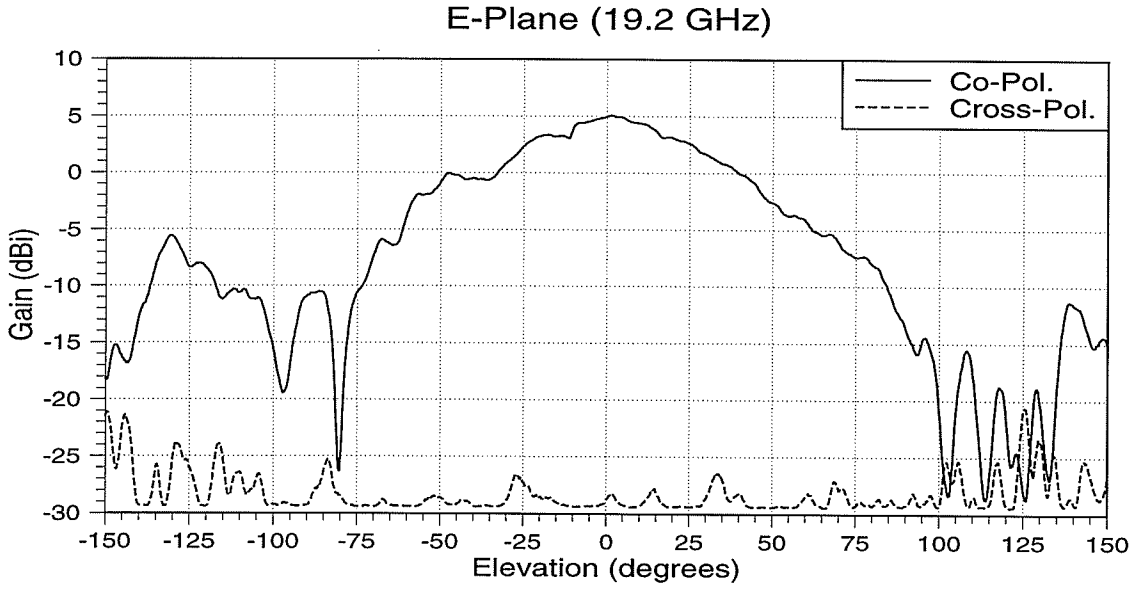

(a)

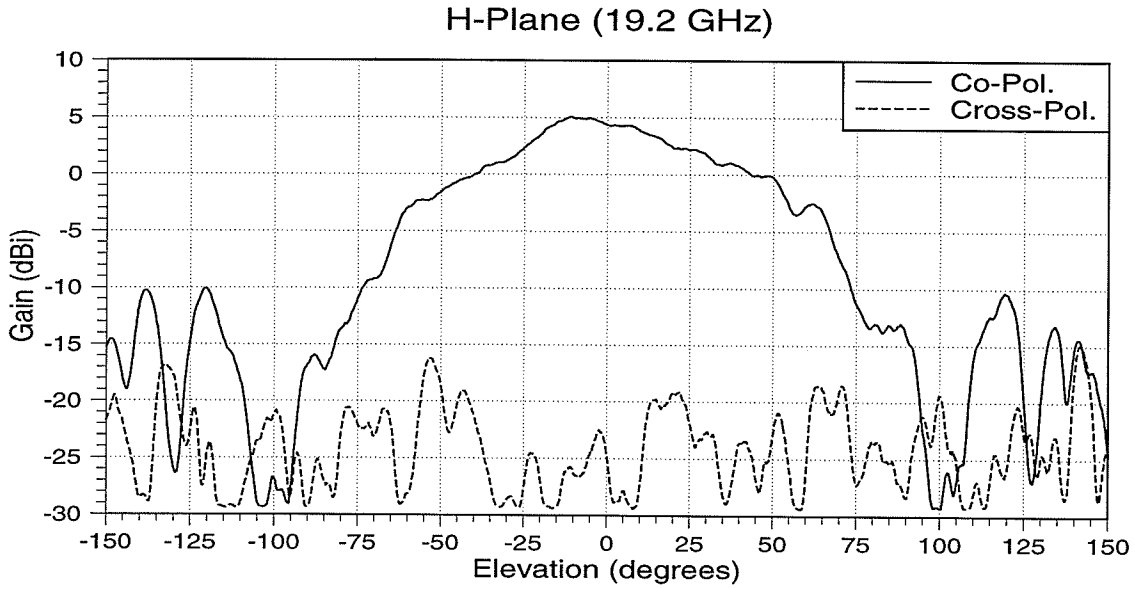

(b)

Figure 4.11: Radiation pattern of a microstrip antenna with a 5.0 λ_g square dielectric cavity
(a) E-Plane, (b) H-Plane

4.3.2 Circular Dielectric Filled Cavities with Various Diameters

A cavity diameter of 5.0 λ_g would be impractical in an antenna array due to spacing and grating lobe problems. Therefore, the minimum cavity dimension must be determined in order for this feeding technique to be practically utilized in array applications. The cavity diameters investigated have the dimensions of 5.0 λ_g (26.50 mm), 3.0 λ_g (16.00 mm), 2.5 λ_g (13.25 mm), 2.0 λ_g (10.62 mm) and 1.5 λ_g (7.97 mm). All cavities are machined as circles and the dielectric pieces which fill the cavities are fabricated using a hole punch. The thick ground plane is also machined to be 180 mm by 180 mm with the cavity located in the centre. The expected gain should theoretically be 0.7 dB lower than the results illustrated in Figure 4.11, due to copper and line losses.

Table 4.2: Stub lengths and centre frequencies for various circular cavities

Cavity Diameter	Stub Length (mm)	Centre Frequency (GHz)	S-parameters	Radiation Pattern	E-Plane Front-to-Side Lobe Ratio (dB)	H-Plane Front-to-Side Lobe Ratio (dB)
5.0 λ_g	1.701	18.968	Figure 4.12	Figure 4.19	10.0	13.0
3.0 λ_g	0.211	18.080	Figure 4.13	Figure 4.20	-1.5	4.0
2.5 λ_g	0.608	18.512	Figure 4.14	Figure 4.21	6.5	5.0
2.0 λ_g	1.154	19.256	Figure 4.15	Figure 4.22	10.5	18.2
1.5 λ_g	1.903	19.640	Figure 4.16	Figure 4.23	5.0	11.0
3.0 λ_g remeasured	1.541	19.232	Figure 4.17	Figure 4.24	11.5	12.0
2.5 λ_g remeasured	1.617	19.736	Figure 4.18	Figure 4.25	4.5	9.5

The antennas with the various cavity diameters are measured and tuned by trimming the transmission line stub. Table 4.2 illustrates the stub lengths and centre frequencies of the various diameters of cavities, along with the figure numbers for the S-

parameters, the radiation patterns, and the front-to-side lobe radiation ratios.

Two cavities with diameters of 3.0 λ_g and 2.5 λ_g are found to have high side-lobe radiation, which is attributed to their short stub lengths. When the stub length is too short, minimal energy couples from the transmission line to the patch, and higher side-lobe radiation results, as seen in Figures 4.20 and 4.21. Therefore, new measurements are performed on those cavities with longer tuning stubs. The longer stubs raise the centre frequency by approximately 1.2 GHz. The stubs are trimmed until the best match occurs.

Both the diameter of the cavity and the corresponding stub length seem to be a determining factor of the side-lobe radiation. The various results for different cavity diameters demonstrate that the side-lobe radiation either increases or decreases with no obvious pattern. A more theoretical study should therefore be conducted on the effect of the cavity diameter.

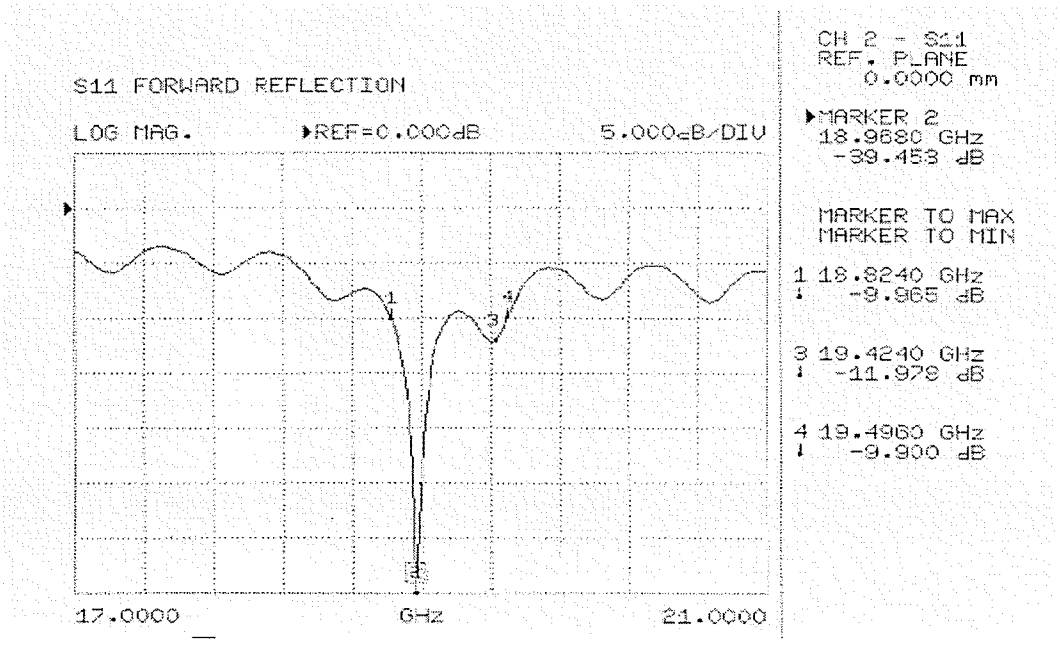

Figure 4.12: S_{11} for microstrip antenna with a circular 5.0 λ_g cavity (Ls = 1.701 mm)

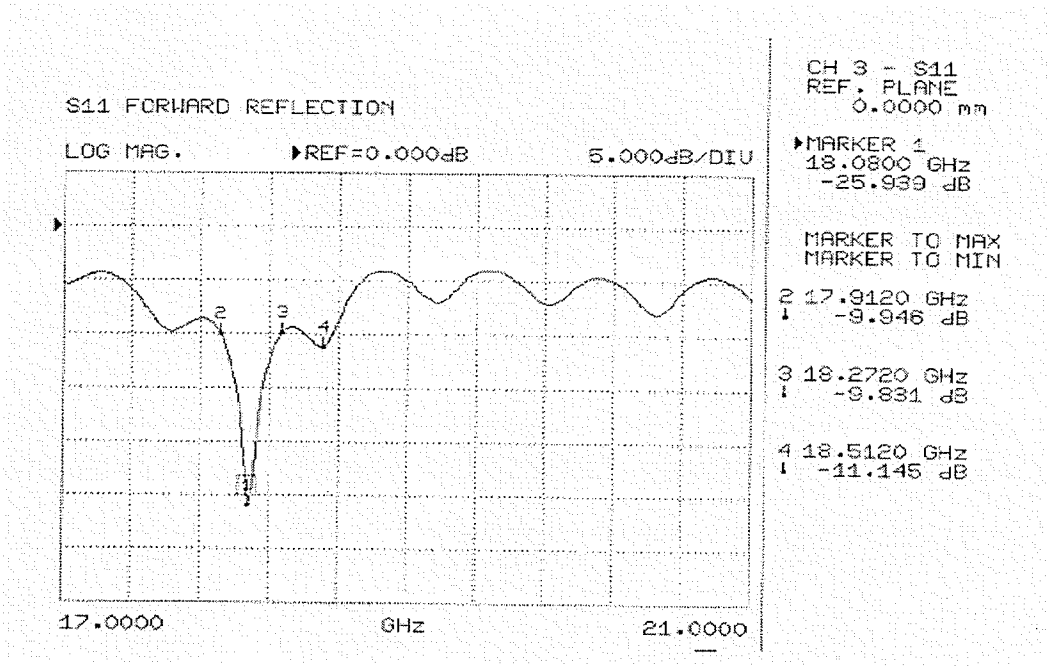

Figure 4.13: S_{11} for microstrip antenna with a circular 3.0 λ_g cavity (Ls = 0.211 mm)

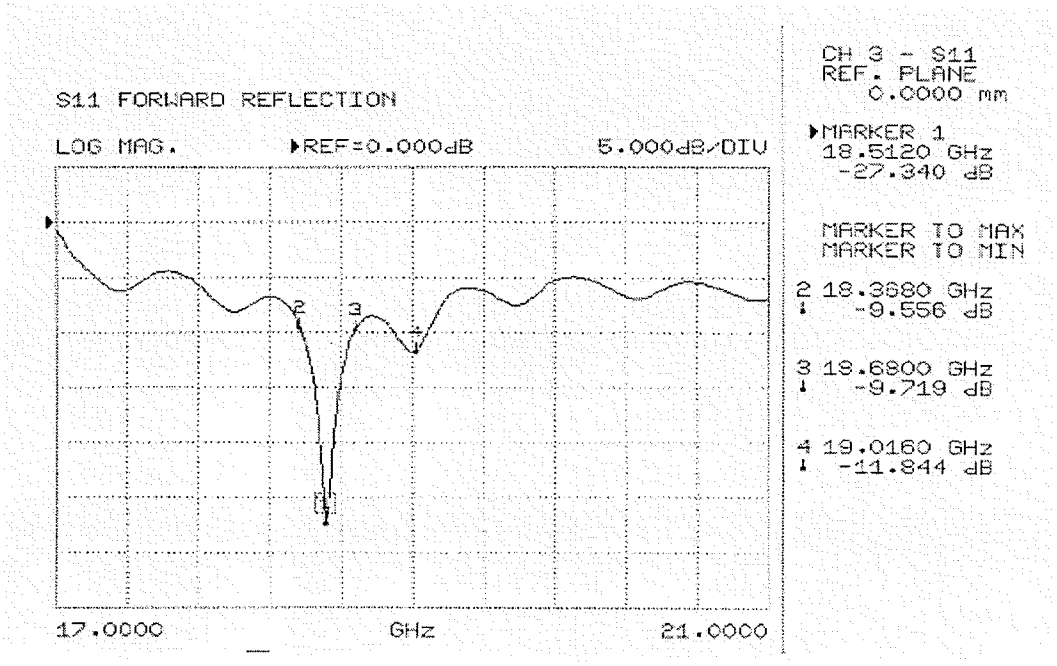

Figure 4.14: S_{11} for microstrip antenna with a circular 2.5 λ_g cavity (Ls = 0.608 mm)

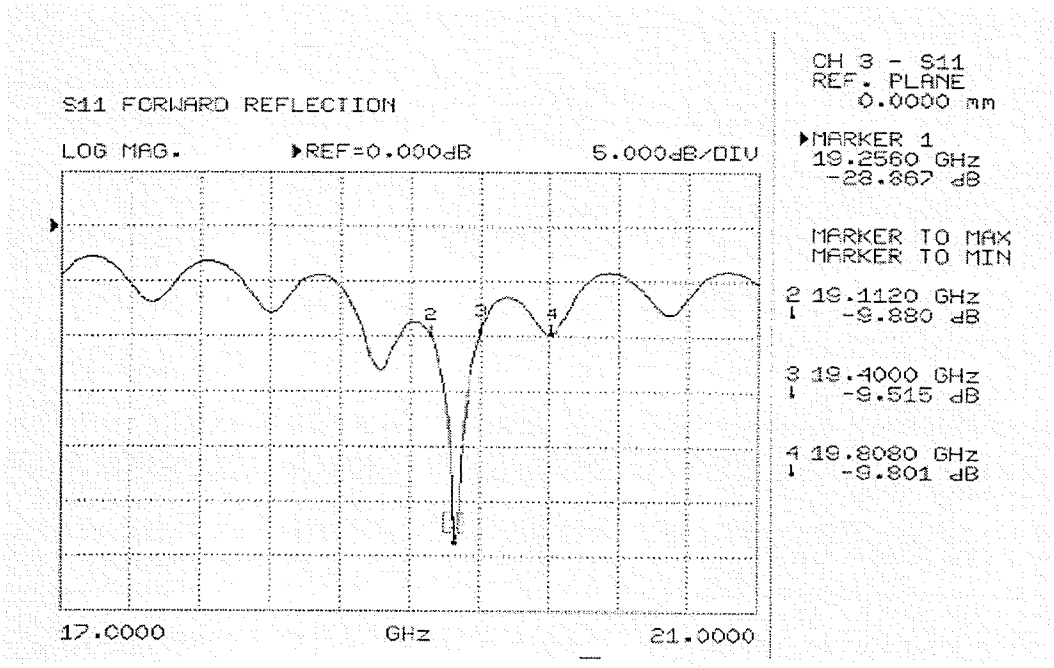

Figure 4.15: S_{11} for microstrip antenna with a circular 2.0 λ_g cavity (Ls = 1.154 mm)

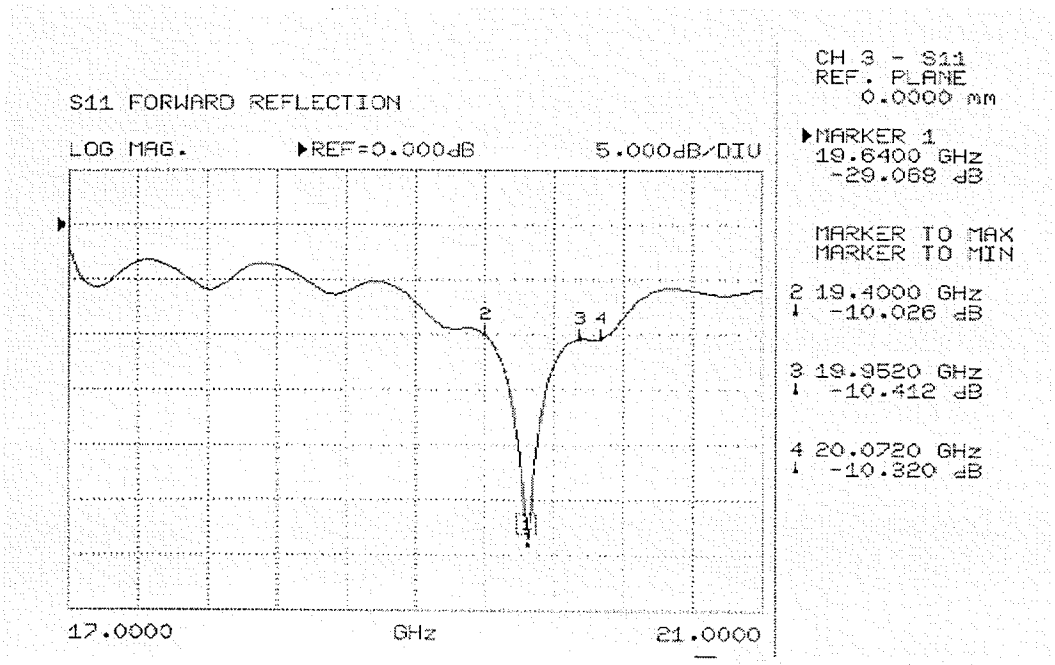

Figure 4.16: S_{11} for microstrip antenna with a circular 1.5 λ_g cavity (Ls = 1.903 mm)

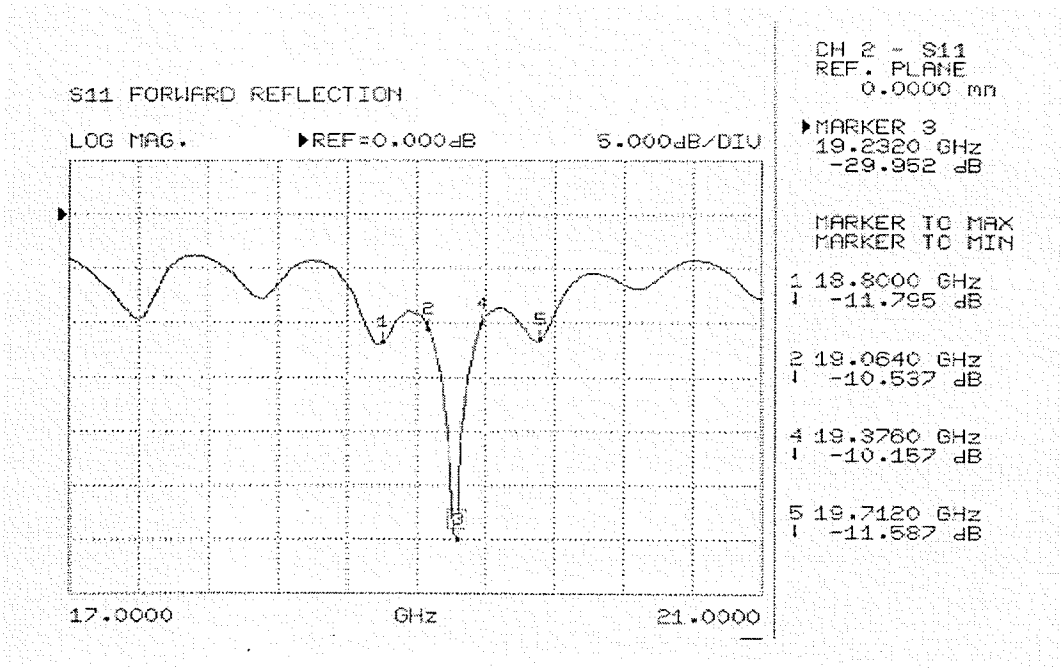

Figure 4.17: S_{11} for microstrip antenna with a circular 3.0 λ_g cavity (Ls = 1.541 mm)

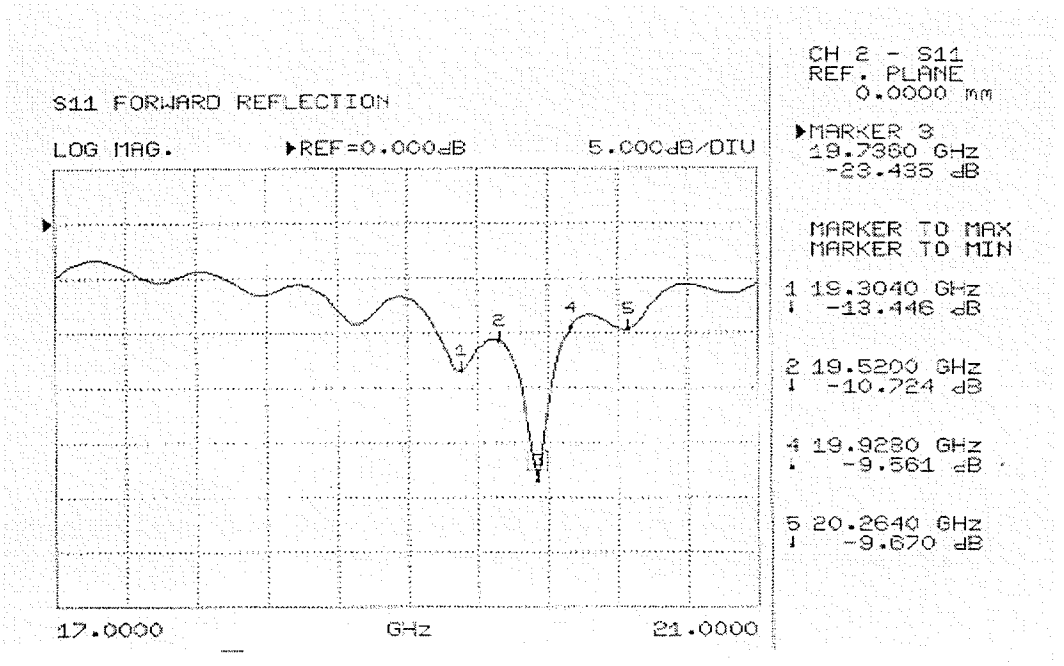

Figure 4.18: S_{11} for microstrip antenna with a circular 2.5 λ_g cavity (Ls = 1.617 mm)

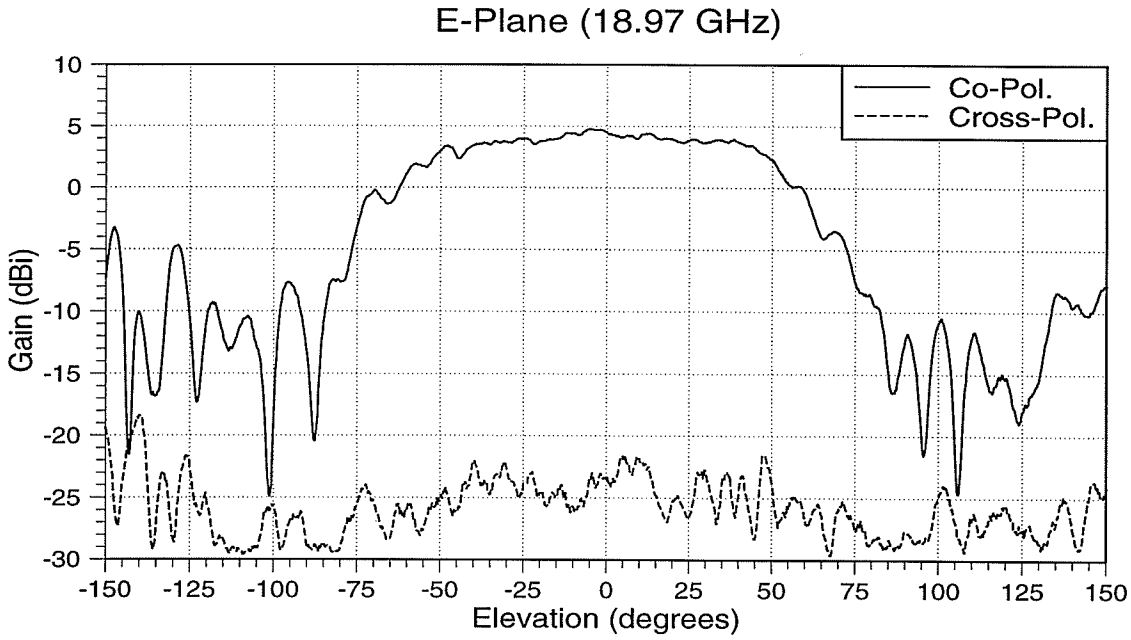

(a)

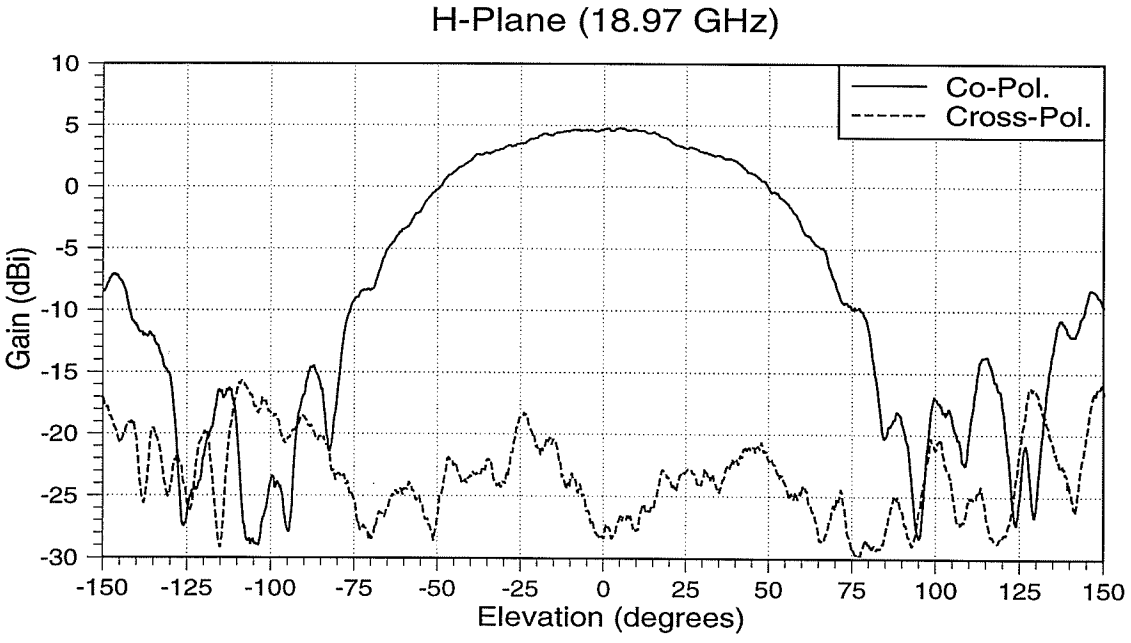

(b)

Figure 4.19: Radiation pattern of a microstrip antenna with a 5.0 λ_g circular cavity and Ls=1.701 mm
(a) E-Plane, (b) H-Plane

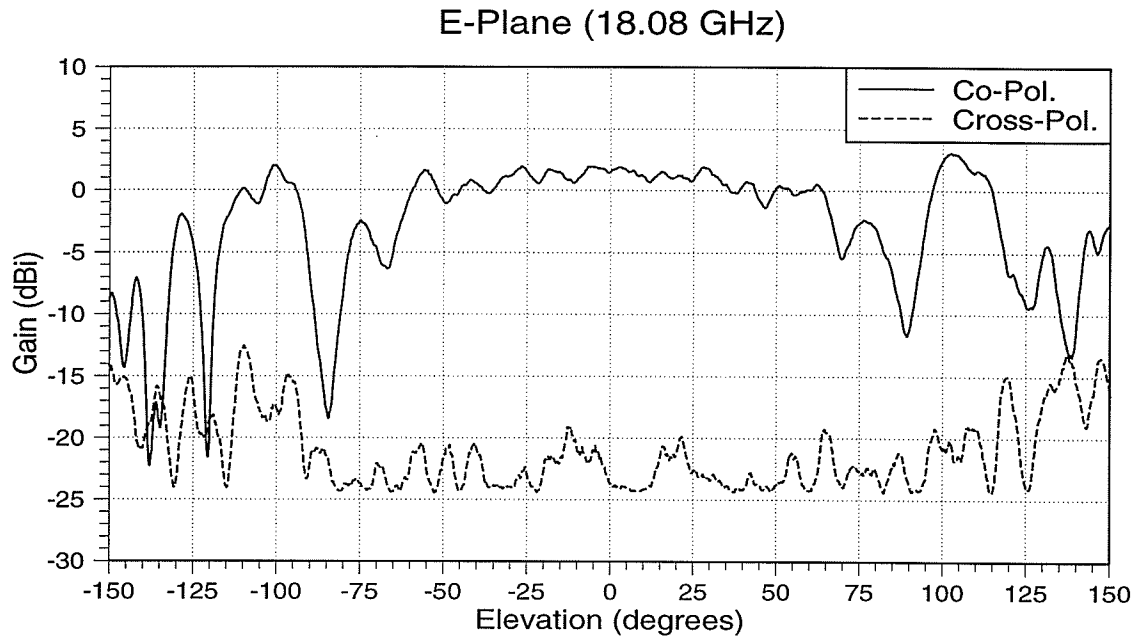

(a)

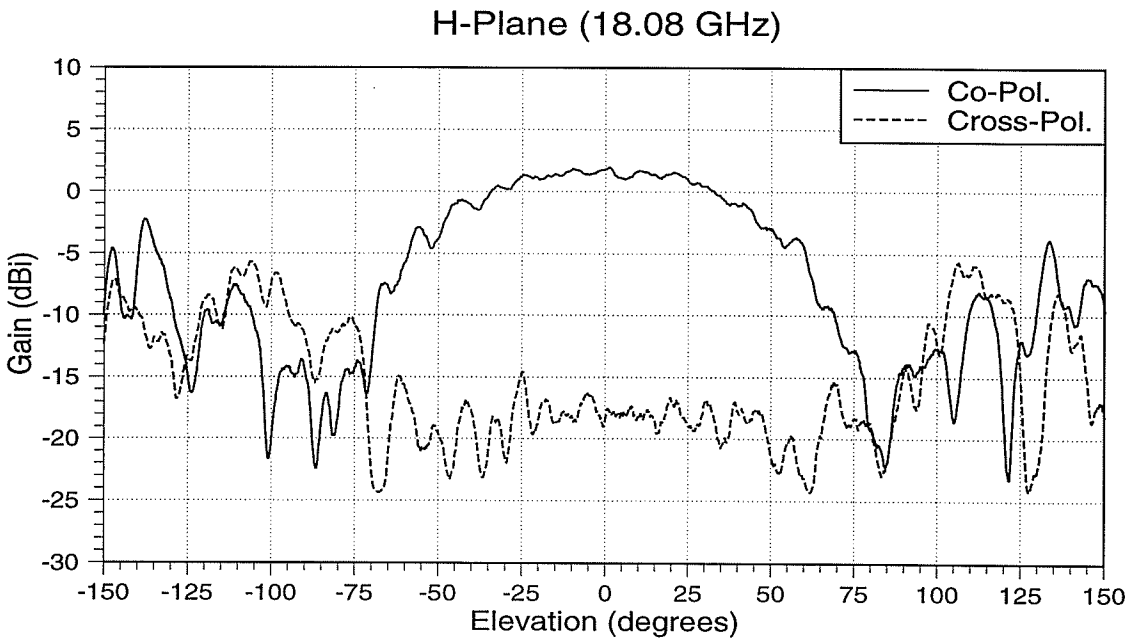

(b)

Figure 4.20: Radiation pattern of a microstrip antenna with a 3.0 λ_g circular cavity and Ls=0.211 mm
(a) E-Plane, (b) H-Plane

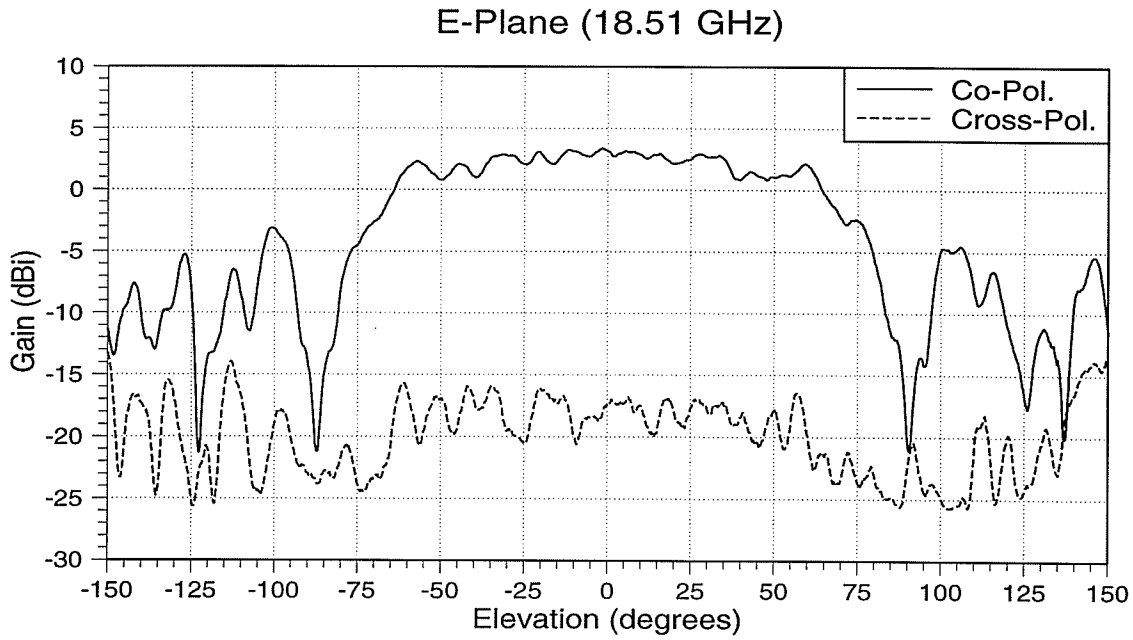

(a)

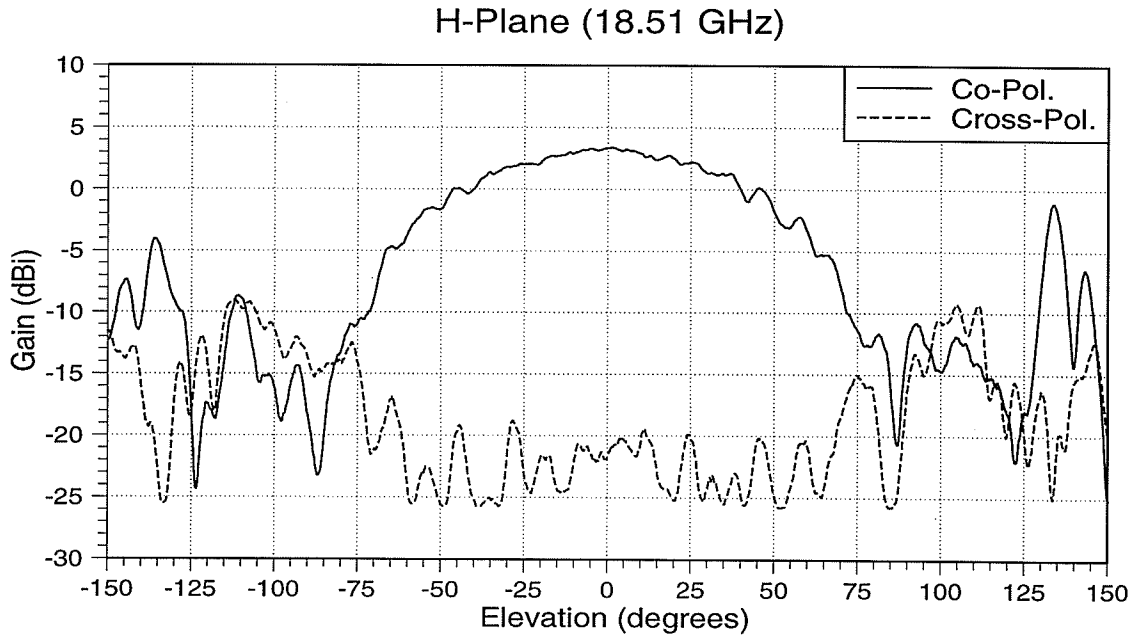

(b)

Figure 4.21: Radiation pattern of a microstrip antenna with a 2.5 λ_g circular cavity and Ls=0.608 mm
(a) E-Plane, (b) H-Plane

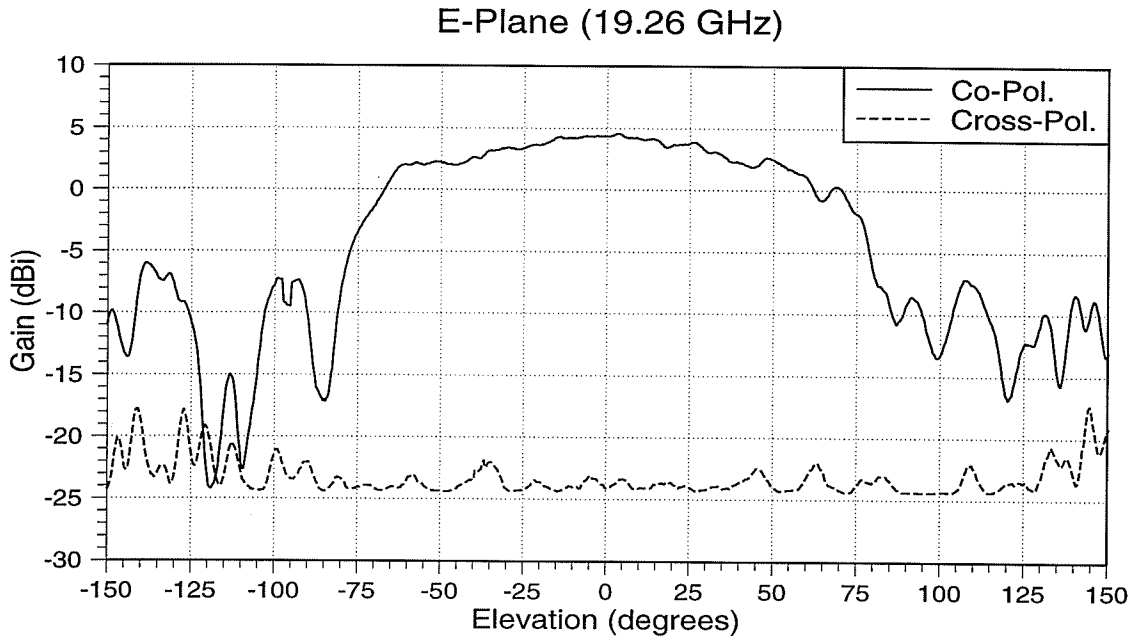

(a)

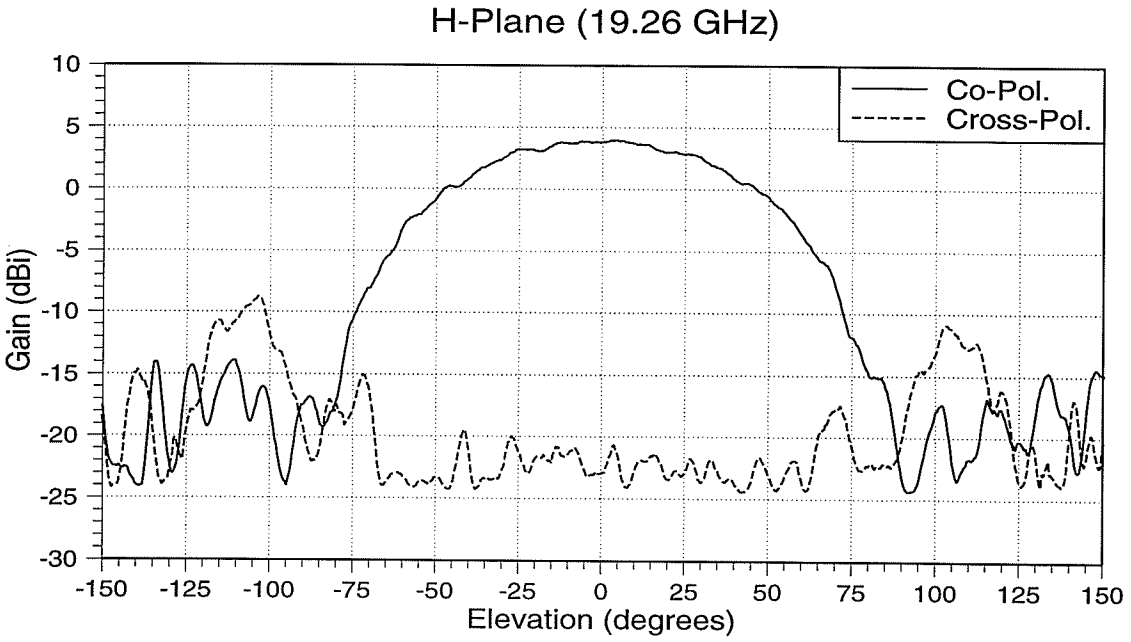

(b)

Figure 4.22: Radiation pattern of a microstrip antenna with a 2.0 λ_g circular cavity and Ls=1.154 mm
(a) E-Plane, (b) H-Plane

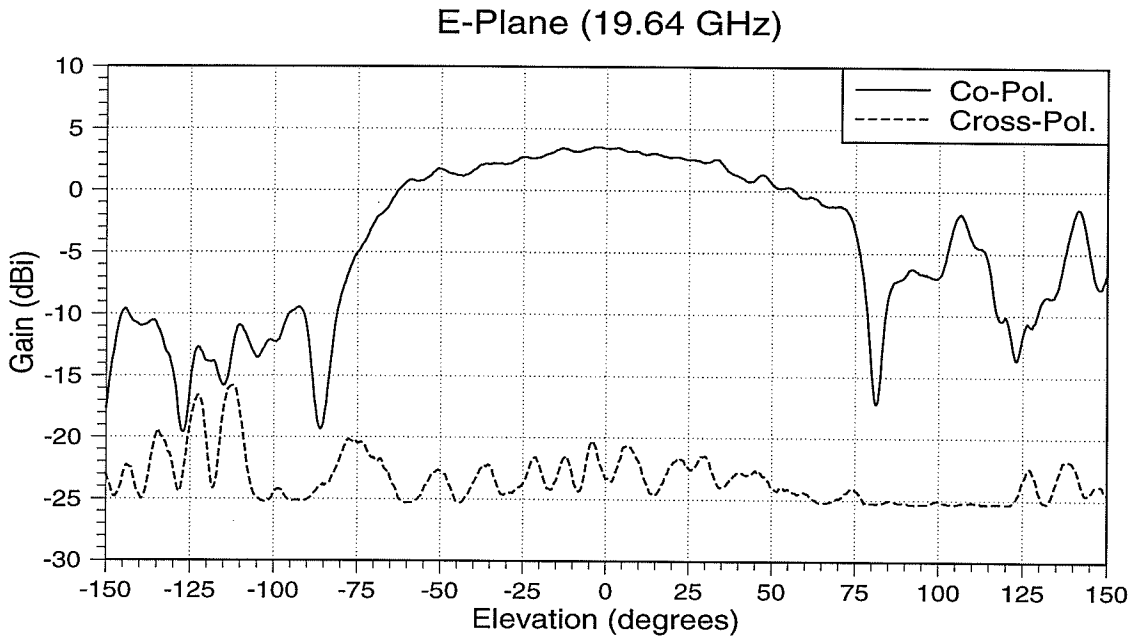

(a)

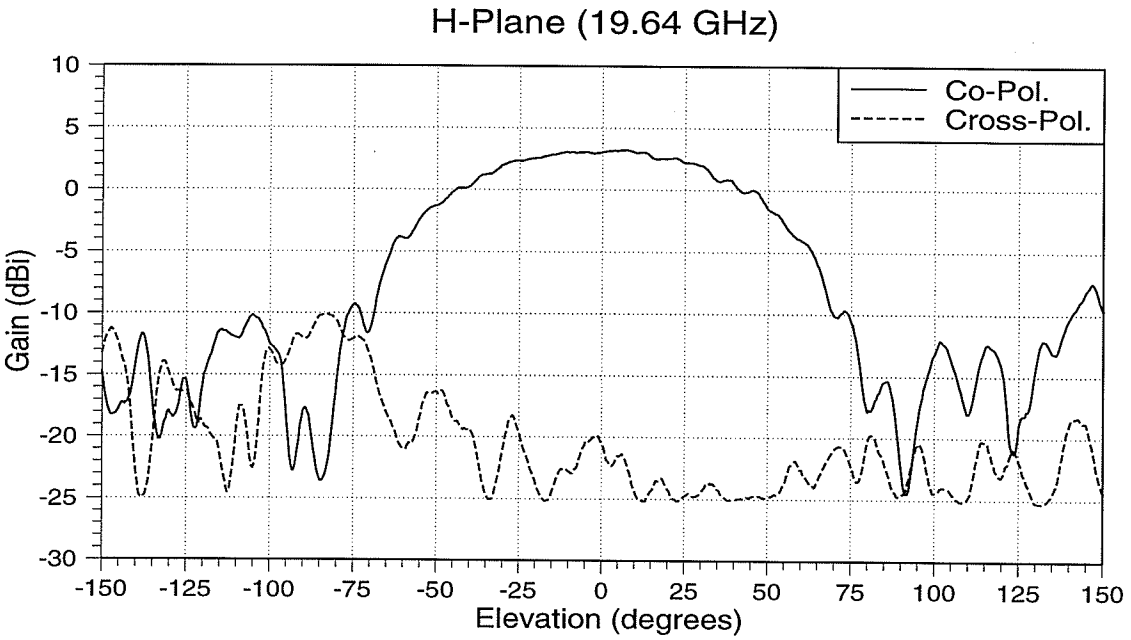

(b)

Figure 4.23: Radiation pattern of a microstrip antenna with a 1.5 λ_g circular cavity and Ls=1.903 mm
(a) E-Plane, (b) H-Plane

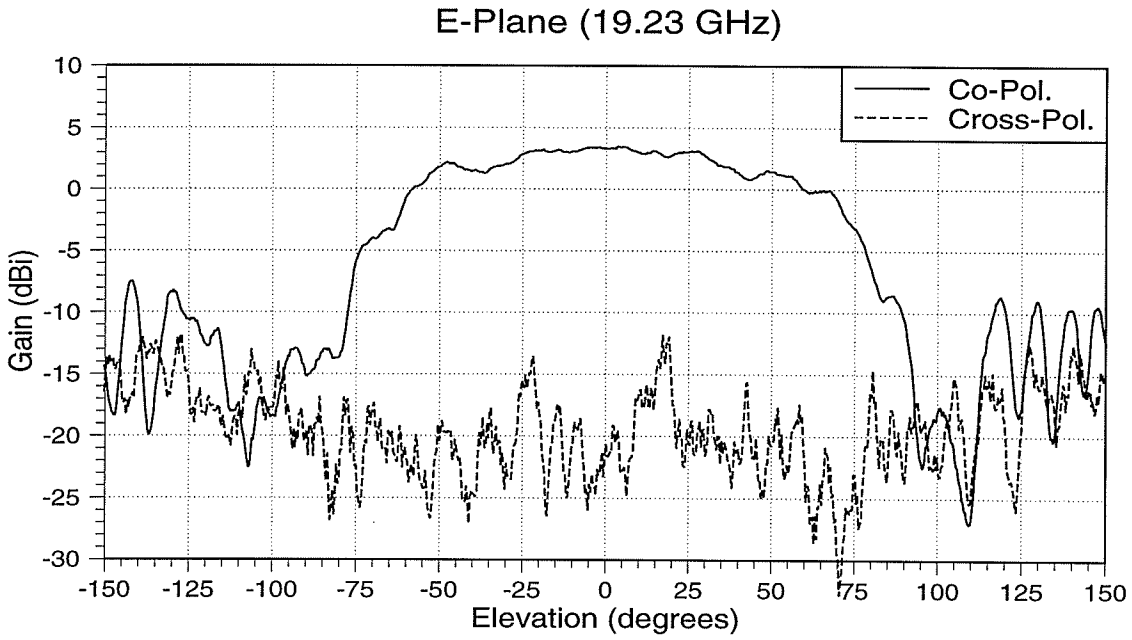

(a)

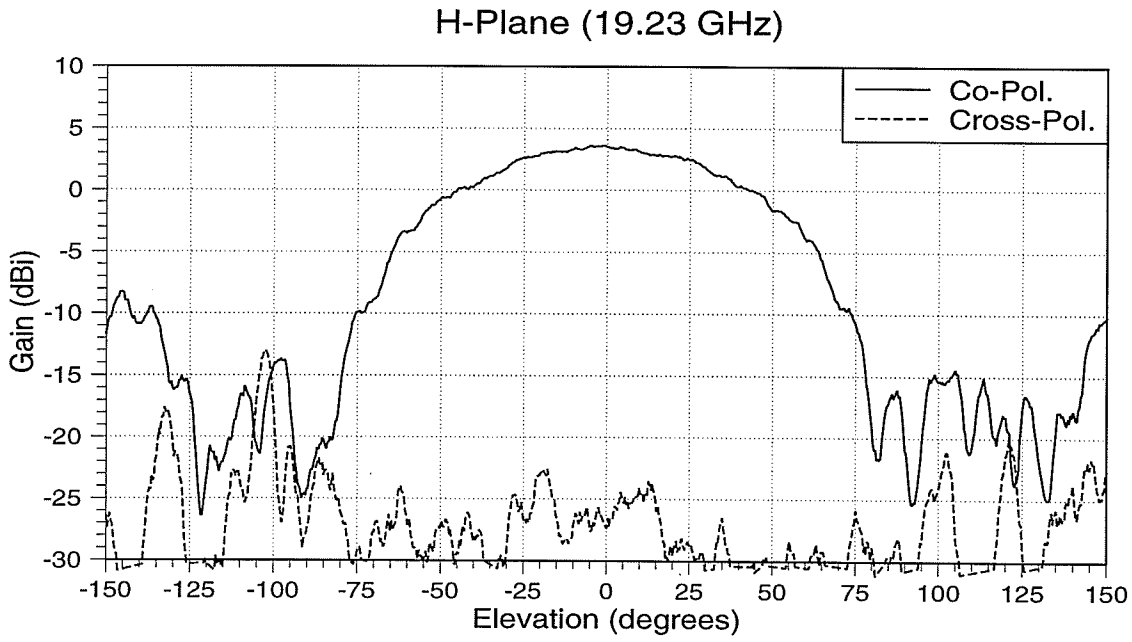

(b)

Figure 4.24: Radiation pattern of a microstrip antenna with a 3.0 λ_g circular cavity and Ls=1.541 mm
(a) E-Plane, (b) H-Plane

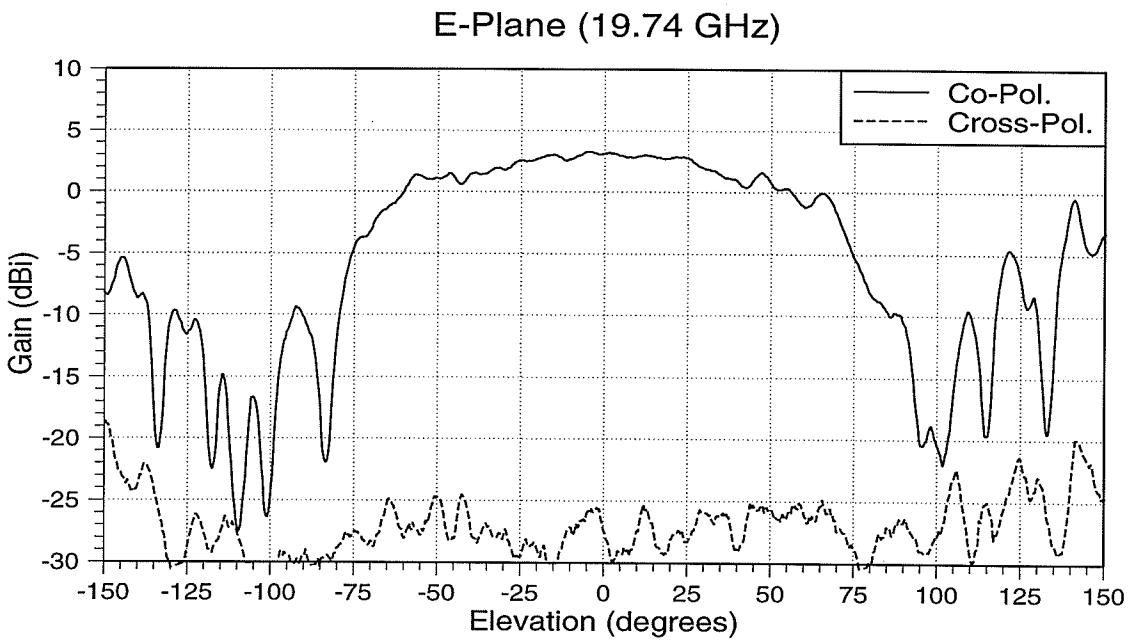

(a)

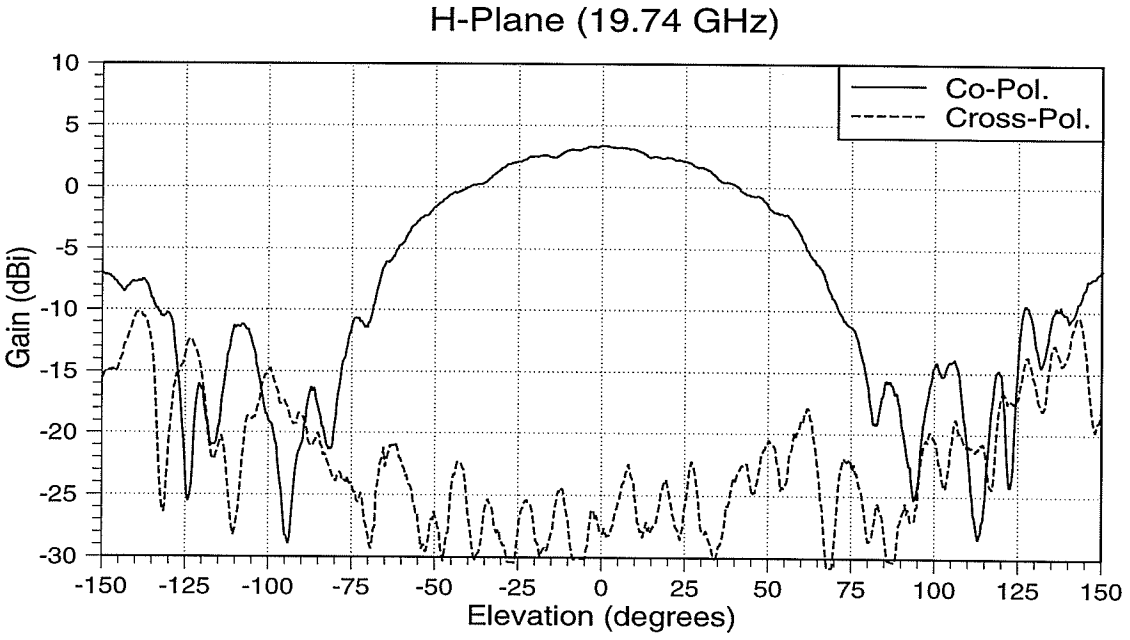

(b)

Figure 4.25: Radiation pattern of a microstrip antenna with a 2.5 λ_g circular cavity and Ls=1.617 mm
(a) E-Plane, (b) H-Plane

4.3.3 Antenna Noise Temperature

The approximate noise temperature of the antenna can be calculated by multiplying the averaged radiated E- and H-plane power and the associated sky noise temperature. This temperature is dependent on the operating frequency of the antenna. The microstrip antenna containing the 2.0 λ_g circular cavity (Table 4.2) has the lowest side-lobe radiation and is therefore chosen for the noise temperature calculation. The fractional areas corresponding to the averaged E- and H-plane radiation power and the associated sky noise temperature [24] are listed in Table 4.3.

Table 4.3: E- and H-plane gains with corresponding sky noise for the microstrip antenna with a 2.0 λ_g circular cavity (Figure 4.22), at a frequency of 20 GHz.

Elevation Angle (degrees)	Averaged E and H Radiated Power (fractional)	Associated Sky Noise Temperature (K)
-180 to -90 and 90 to 180	0.0525	300
-90 to -85 and 85 to 90	0.0031	150
-85 to -80 and 80 to 85	0.0043	100
-80 to -70 and 70 to 80	0.0154	50
-70 to -60 and 60 to 70	0.0664	30
-60 to -40 and 40 to 60	0.1885	20
-40 to 40	0.6697	14

The approximate antenna noise temperature is found to be 32.81°K, when the antenna is aimed at the zenith. The precise method of calculating antenna noise temperature requires integrating the front radiation and back radiation with the associated sky noise temperature. However, the integration method gives only a marginally more accu-

rate antenna noise temperature.

4.3.4 Integration of an LNA into the Antenna Structure

This section examines the operation of the antenna with an LNA. The antenna selected for testing with the LNA has the 5.0 λ_g width square cavity. The chosen LNA is designed at the CRC (Communications Research Centre) in Ottawa. The LNA operates at approximately 20 GHz with approximately 20 dB of gain.

The LNA's S-parameters are measured to determine the mismatch, gain and isolation. The measured S-parameters are illustrated in Figure 4.26 and Figure 4.27. The passive antenna structure has the best match at 19.2 GHz. The input match of the LNA at 19.2 GHz is approximately -2.7 dB. At this frequency the gain is found to be 21.9 dB, the isolation -24.7 dB, and the output match -21.6 dB. The amplifier is designed to operate at 17.75 GHz with a 1.5 GHz 10 dB impedance bandwidth. Because the input match at 19.2 GHz is poor, the performance of the antenna may be affected due to the non-50-ohm system. However, this LNA is the only one available at the required frequency, and thus it has to be used. In order for the amplifier to operate with the lowest noise figure, the drain voltage has to be fixed at 2.0 V and the drain current at 5 mA. The measured LNA noise figure is 2.15 dB (185.77°K) at 19.2 GHz.

The LNA carrier material consists of kovar, which has the same coefficient of thermal expansion as alumina. The amplifier circuitry is fabricated on 0.254 mm thick alumina and the microstrip antenna transmission line on 0.254 mm thick duroid. In order to minimize mismatches, the ground plane of the LNA and the ground plane of the transmission line need to be aligned with each other. The base of the kovar carrier is designed to fit

into a machined cavity in the brass ground plane of the antenna. The kovar carrier/LNA unit is illustrated in Figure 4.28, and the carrier/LNA unit which fits into the milled ground plane cavity is shown in Figure 4.29.

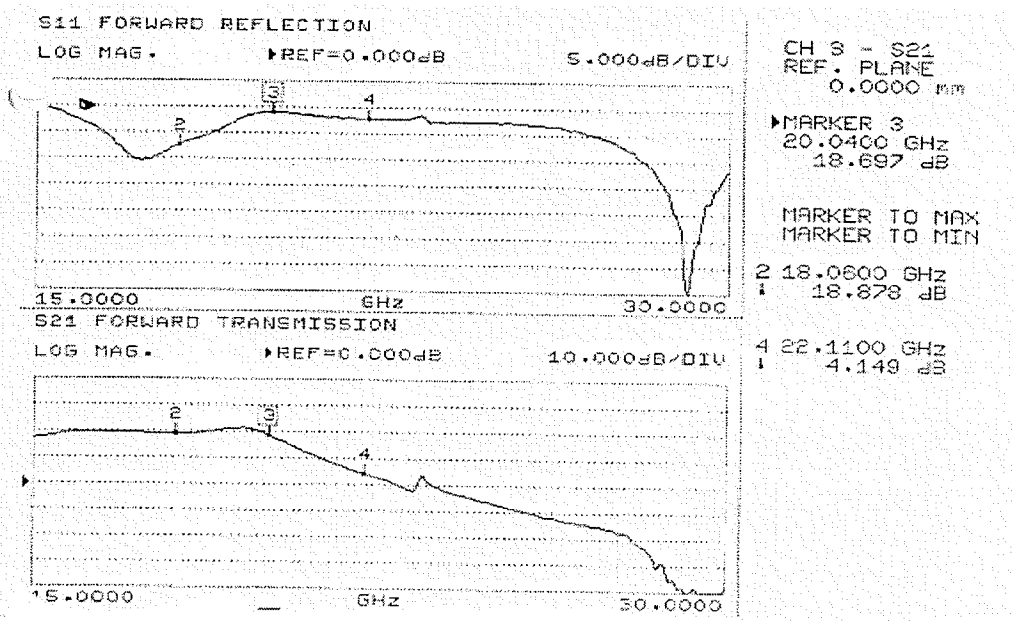

Figure 4.26: S_{11} and S_{21} for the low noise amplifier

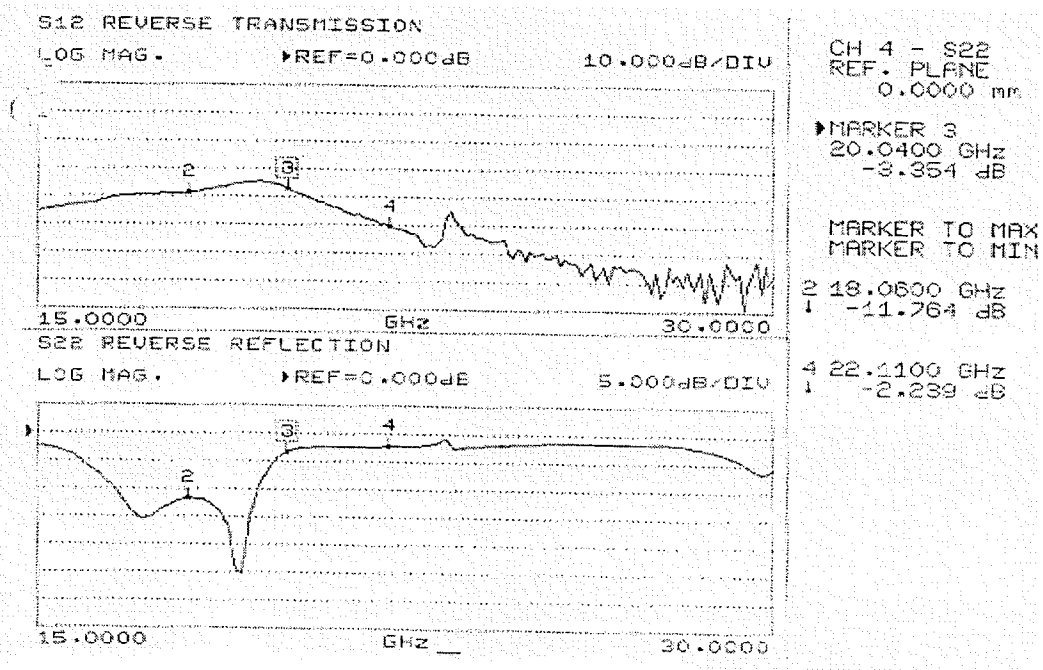

Figure 4.27: S_{22} and S_{12} for the low noise amplifier

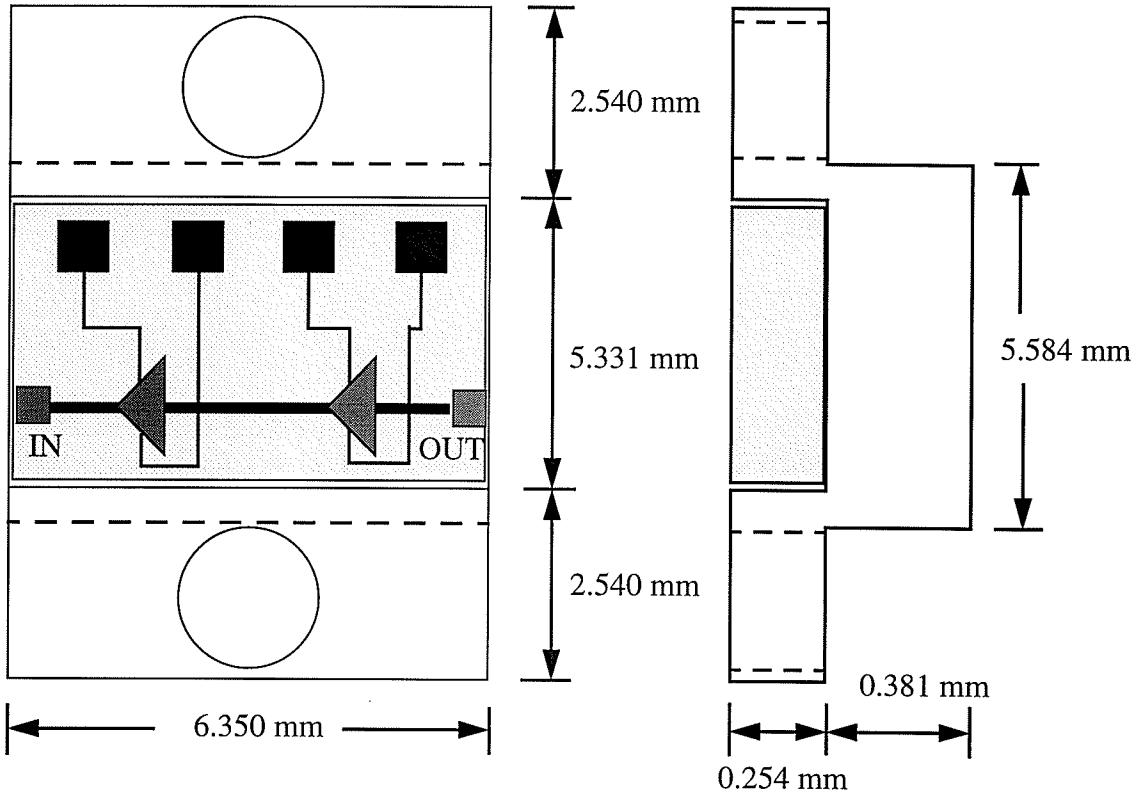

Figure 4.28: Dimensions of kovar carrier containing the LNA

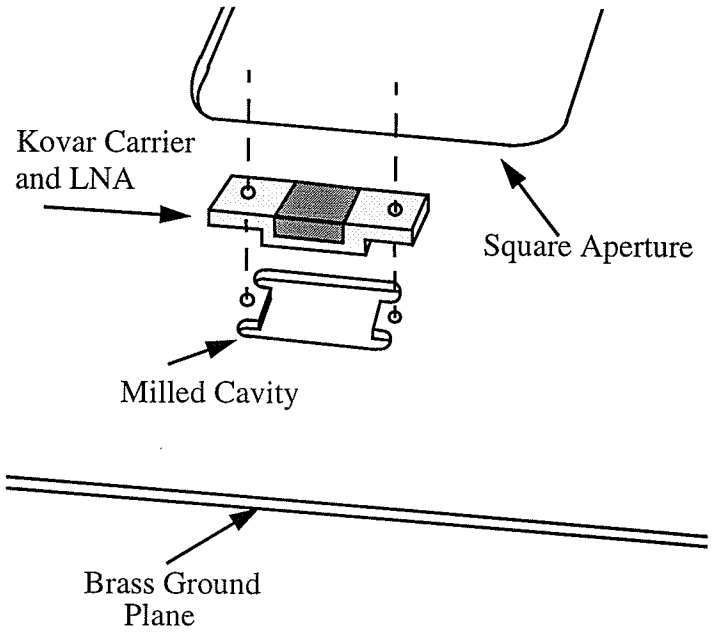

Figure 4.29: Placement of kovar carrier/LNA unit into the brass ground plane

A rectangular piece of material is removed from the transmission line substrate, which is located directly over the milled cavity. This hole is carefully shaped to minimize the space between the LNA and antenna transmission lines. The LNA is placed into the cavity and fastened to the brass ground plane with screws. An ultrasonic ribbon bonder is used to form an electrical connection between the LNA and the transmission line.

A metal structure is added to the back of the antenna, which contains four filter-cons. Filter-cons allow DC current to pass, but filter out AC current. The LNA contains two amplifier stages, each containing a drain, a gate, and ground ports; two of the filter-cons are connected to the drain voltage ports, and the other two are connected to the gate voltage ports. The electrical ground connections are made through the kovar carriers to the antenna ground plane. The two stages are powered separately in order to verify that each stage is functioning correctly.

The antenna radiation pattern at 19.2 GHz of the active antenna is illustrated in Figure 4.30, which, when compared with Figure 4.11, demonstrates a gain increase of approximately 22 dB. The gain of the LNA at this frequency is 21.9 dB. The side-lobe radiation level increases with the integration of the LNA. This is possibly due to the mis-match between the antenna element and the LNA. The LNA raises both the co-polarized and the cross-polarized gain by 21.9 dB.

The increase in cross-polarization levels is unfortunate. However, the active aper-ture-coupled microstrip antenna has the advantage of being small, flat and light-weight.

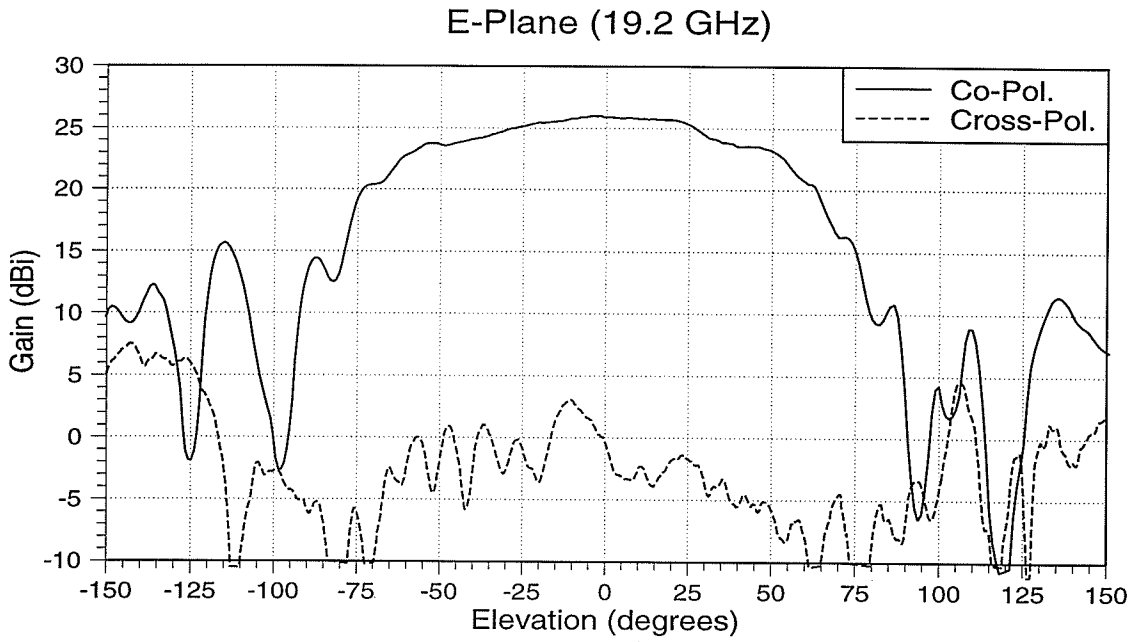

(a)

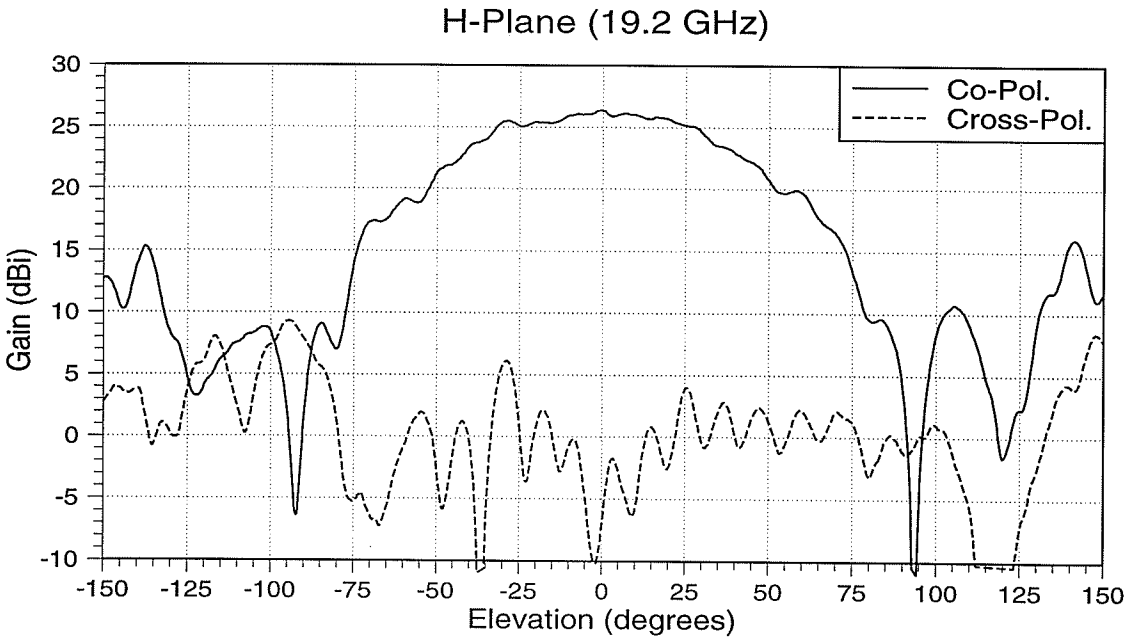

(b)

Figure 4.30: Radiation pattern of an active microstrip antenna (a) E-Plane, (b) H-Plane

4.4 System Noise

Adding an LNA to a receive antenna application is advantageous because of the increased signal-to-noise-ratio performance. Amplifiers are especially important in situations where transmission lines are electrically long (i.e., losses are high). In antenna arrays, lengthy transmission lines generally exist due to the linking of many antenna elements to a common transmission line. For long transmission lines, the receive signal power could diminish considerably, resulting in an increased system noise temperature. An amplifier located electrically close to the antenna element can significantly reduce the effect of noise caused by the lengthy transmission lines.

This section presents the basics of system noise, a system noise example, and an approximate G/T ratio for the active antenna.

4.4.1 Noise Overview

Noise in a system is usually caused by the random motions of charge carriers in devices and materials. Some typical types of noise [24], [25] are:

Thermal Noise: Random motions of charges or charge carriers. This includes ohmic losses which are dependent on temperature.

Sky Noise: Caused by the attenuation of a wave as it passes through the atmosphere. Causes of this attenuation include atmospheric gases and hydrometeors (rain, snow, etc.)

Other Noise: Shot noise, flicker noise, plasma noise and quantum noise.

A typical system usually consists of cascaded components (i.e., antenna, amplifier,

transmission line, etc.). Each component can degrade the signal to noise ratio. The noise figure (or noise temperature) can be determined if the noise figure is known for the individual components. Depending on how the various components are placed, the system noise figure can vary.

Noise theory can be utilized to determine the optimum component setup for the lowest system noise temperature. Figure 4.31 illustrates how two cascaded networks can be presented as an equivalent network [25]:

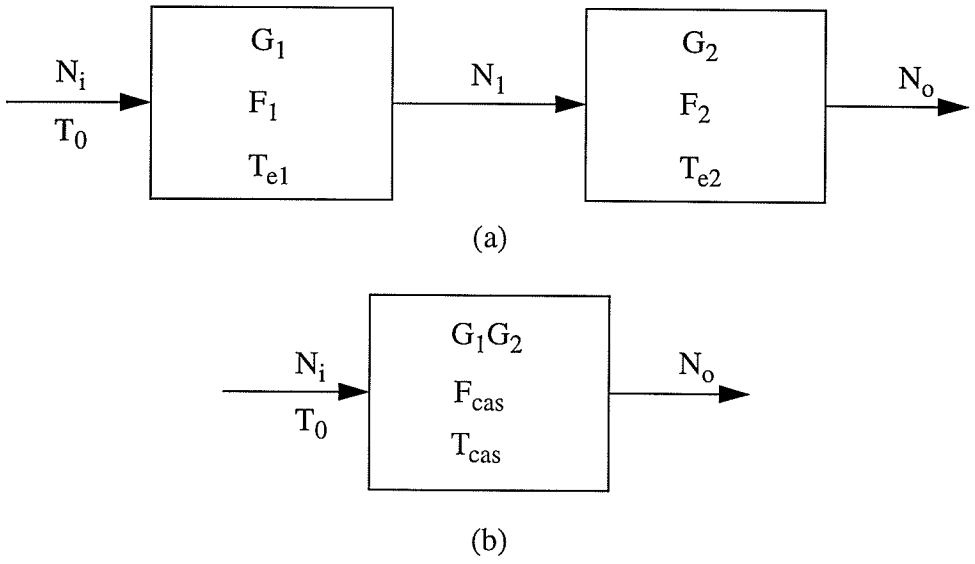

Figure 4.31: Noise figure and equivalent noise temperature of a cascaded system (a) Two cascaded networks, (b) Equivalent network

Noise temperature is given by:

$$T_e = \frac{P_s}{kB} \tag{4.1}$$

Where T_e is the equivalent temperature in degrees kelvin (K), P_s is the noise power, k is the Boltzman constant (1.380×10^{-23} J/°K) and B is the bandwidth of the system in Hz.

Using the noise temperatures (Figure 4.31(a)), the noise power at the output of the first stage is:

$$N_1 = G_1 k T_0 B + G_1 k T_{e1} B \tag{4.2}$$

The noise power at the output of the second stage is given by:

$$N_o = G_2 N_1 + G_2 k T_{e2} B = G_1 G_2 k B \left(T_0 + T_{e1} + \frac{1}{G_1} T_{e2} \right) \tag{4.3}$$

The equivalent system can be found to be:

$$N_o = G_1 G_2 k B \, (T_{cas} + T_0) \tag{4.4}$$

where

$$T_{cas} = T_{e1} + \frac{1}{G_1} T_{e2} \tag{4.5}$$

The noise figure is given by:

$$F = 1 + \frac{T_e}{T_0} \geq 1 \tag{4.6}$$

Therefore, equation (4.5) can be rewritten as:

$$F_{cas} = F_1 + \frac{1}{G_1} (F_2 - 1) \tag{4.7}$$

Both equations (4.5) and (4.7) show that the first stage has the most dominant consequences. Therefore, in order to obtain the best possible system noise performance, the first stage should have a low noise figure and reasonable gain. The later stages have a diminishing impact on the overall noise performance, as shown in the following generalized equations:

$$T_{cas} = T_{e1} + \frac{T_{e2}}{G_1} + \frac{T_{e3}}{G_1 G_2} + \ldots \tag{4.8}$$

$$F_{cas} = F_1 + \frac{F_2 - 1}{G_1} + \frac{F_3 - 1}{G_1 G_2} + \ldots \tag{4.9}$$

Therefore, the LNA should be located as close as possible to the antenna element to reduce the overall noise figure or noise temperature.

4.4.2 System Noise Example and G/T Ratio of the Active Antenna

This section examines the system noise as a function of component location (i.e., transmission lines, amplifiers, etc.) with the use of an example. Also, the G/T (Gain to noise Temperature) ratio of the active antenna is calculated.

Placing the LNA close to the antenna element, as opposed to a significant distance away, should theoretically result in the lower system noise temperature. An example of the noise temperature for two different component configurations is illustrated in Figure 4.32. The first case shows a configuration consisting of the antenna element, the transmission line, and the amplifier. In the second case, the configuration consists of the antenna element, the amplifier, and a transmission line. The LNA and antenna element parameters from section 4.3 are utilized in this example, and the length of the transmission line is chosen to be 38.65 mm. At frequencies of 20 GHz on a substrate 0.254 mm thick, with a dielectric constant of 10.2 and a transmission line 0.238 mm wide, losses equal approximately 0.164 dB per wavelength. The guide wavelength at 20 GHz for the given transmission line is 5.64 mm.

The theoretical system temperature of the two active antenna systems is presented

in Figure 4.32. CASE 1 has a significantly higher system temperature than CASE 2. Therefore, the LNA should be located as closely to the antenna element as possible, in order to reduce system noise temperature.

CASE 1.

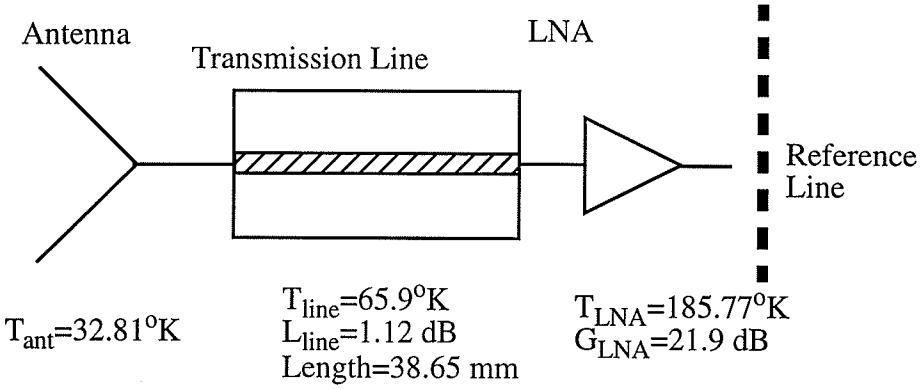

$$T_{ref}=T_{ant}G_{line}G_{LNA}+T_{line}G_{line}G_{LNA}+T_{LNA}G_{LNA}$$
$$=[T_{ant}+T_{line}+\frac{T_{LNA}}{G_{line}}]G_{line}G_{LNA}$$
$$=41134^{o}\ K$$

CASE 2.

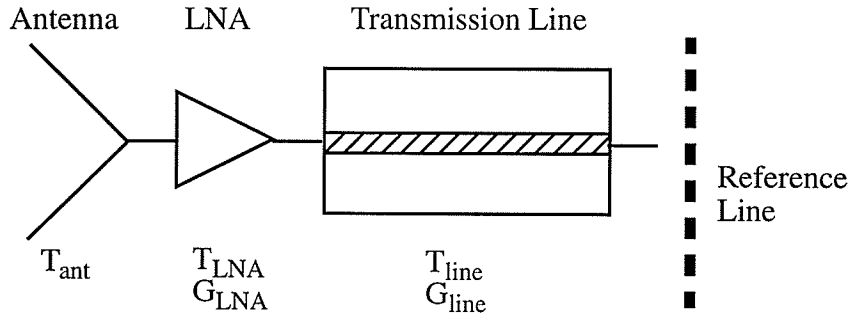

$$T_{ref}=T_{ant}G_{LNA}G_{line}+T_{LNA}G_{LNA}G_{line}+T_{line}G_{line}$$
$$=[T_{ant}+T_{LNA}+T_{line}]G_{LNA}G_{line}$$
$$\overline{G_{LNA}}$$
$$=26708^{o}\ K$$

where L - loss
G - gain
T - noise temperature
G=1/L
and the system is referenced to 290° K

Figure 4.32: Effects of amplifier location on the noise temperature

The G/T ratio is used as a *figure of merit* for receive antennas [26]. The ratio combines the gain of the antenna with the various contributing noise components (sky noise, line loss, amplifier noise, etc.). As mentioned above, the placement of components can significantly alter the noise figure of a system. The placement of components can also greatly affect the G/T ratio.

An approximate G/T ratio for the active antenna presented in this thesis can be found as follows. The dimensions, gains, losses and noise temperatures for the active antenna are illustrated in Figure 4.33.

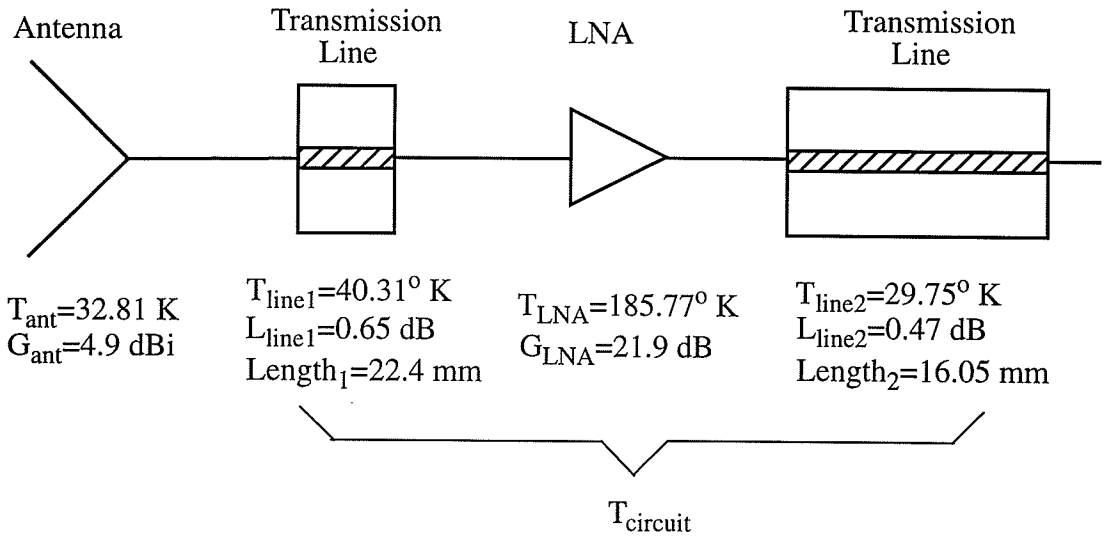

$$T_{circuit}=(T_{line1}+T_{LNA}/G_{line1}+T_{line2}/(G_{line1}G_{LNA}))G_{line1}G_{LNA}G_{line2}$$
$$=30656.87 \text{ K}$$

where L - loss
G - gain
T - noise temperature
G=1/L
and the system is referenced to 290° K

Figure 4.33: G/T parameters for the active antenna

The equation for G/T ratio is:

$$\frac{G}{T} = \frac{G_{ANT}}{T_{ANT} + T_{circuit}} \tag{4.10}$$

and the approximate G/T ratio for the active antenna is calculated to be:

$$\frac{G}{T} \cong -40.0 \; dB/\mathrm{K} \tag{4.11}$$

4.5 Summary

In this chapter, a novel method for combining a thick sheet of metal with an aperture-coupled microstrip antenna structure is investigated. A thick ground plane containing a dielectric filled cavity is placed between the thin ground plane and feed substrate.

This chapter consists of four sections. The first section presents results of two microstrip transmission line transitions. The experimental and computed results match quite well for the transition with the smaller step, but are found not to agree very well for the larger step (for frequencies higher than 20 GHz). The second section presents the design and test results for aperture-coupled microstrip antennas with 0.891 and 1.145mm thick feed substrates. The experimental results for both antennas do not match well with the modal expansion analysis results. This is because the dynamic transmission line model only functions correctly for thin substrates. The antenna with the 0.891 mm thick feed substrate is found to radiate with stub tuning but the radiation pattern results in a high side-lobe level.

The third section combines the microstrip transmission line transition and the antenna with the 0.891 mm thick feed substrate. The antenna is tested and found to be

equivalent in function to an aperture-coupled microstrip line with a thin feed substrate, except that the front-to-side radiation ratio is lower. The diameter of the cavity surrounding the aperture in the ground plane is found to affect the front-to-side radiation ratio. An LNA is integrated into the passive antenna structure, and the co- and cross-polarized E- and H-plane levels increase in accordance with the LNA gain. The side-lobe level also increases, which is possibly due to the poor match of the LNA. The final section investigates the system noise temperature of the active antenna with the use of an example, and a theoretical G/T ratio calculation is made.

Chapter 5:

Conclusions and Future Directions

5.0 Conclusions

In this thesis, a method is developed to integrate active devices with aperture-coupled microstrip antenna structures. The goal of the research is to find a technique which makes designs uncomplicated, gives good antenna performance, and results in low fabrication costs. In accordance with this goal, the following information and results are presented in this thesis:

- A basic review of two numerical techniques utilized in the research of various antenna and transmission line structures are presented. The numerical techniques included are the modal expansion method for an aperture-coupled microstrip antenna [2] and the full-wave TLM (Transmission Line Matrix) method [3].

- Two- and four-port aperture-coupled microstrip couplers are designed and tested. The TLM method is found to agree reasonably well with the measured results. The coupler dimensions are optimized for maximum coupling for a number of different ground plane thicknesses. The couplers are found to radiate as the ground plane thickness increases.

- The modal expansion method is utilized in the design of aperture-coupled microstrip antennas with thick feed substrates. The algorithm presented by [2] is found to

become less accurate as the feed substrate thickness increases, which is due to the dynamic transmission line model. The transmission line substrate thickness is found to affect the front-to-side radiation ratio. The H-plane differs by 15.2 dB and the E-plane differs by 10.8 dB. For a thin feed substrate, the front-to-back radiation ratio is found to differ by 22 dB [24].

- The microstrip antenna containing a thick ground plane is fabricated and tested with and without active circuitry. The diameter of the cavity surrounding the aperture in the ground plane is found to affect the front-to-back radiation ratio and the impedance match.

- An approximate noise temperature of the antenna containing a thick ground plane is calculated to be 32.81°K.

- An LNA, when integrated into the passive antenna structure, is found to cause the co- and cross-polarized E- and H-plane levels to increase accordingly with the LNA gain. The LNA also causes the back lobe level to increase, which is possibly due to the poor impedance match.

- An approximate G/T ratio of the active antenna is found to be -40.0 dB/K.

5.1 Future Directions

The following topics are proposed for future investigation:

- The modification of the aperture-coupled microstrip antenna algorithm given by [2]. The transmission line model should be altered to allow for thick feed substrates.

- The investigation of how the cavity diameter surrounding the aperture affects the impedance match and radiation pattern of the aperture-coupled microstrip antenna with a thick ground plane. Also, the determination of what the smallest cavity diameter can be.

- To minimize the back-plane radiation for aperture-coupled antenna structures containing a thick ground plane.

References

References

[1] R. Martinez, R. Compton, "High-efficiency FET/microstrip-patch oscillators", *IEEE Trans. Antennas and Propogation Magazine*, vol. 36, no. 1, pp. 16-19, 1994.

[2] A. Ittipiboon, R. Oostlander, Y. M. M. Antar, M. Cuhaci, "A modal expansion method of analysis and measurement on aperture-coupled microstrip antenna," *IEEE Transactions on Antennas and Propagation*, vol. AP-39, no.11,pp. 1567-1574, 1991.

[3] P.B. Johns and R.L. Beurle, "Numerical solution of two-dimensional scattering problems using a transmission-line matrix," *Proceedings of the IEE*, vol. 118, pp. 1203-1208, 1971.

[4] P.B. Johns, "A symmetric condensed node for the TLM method," *IEEE Transactions on Microwave Theory and Techniques.*, vol. 35, no. 4, pp. 370-377, Apr. 1987.

[5] R. Oostlander, "A study of microstrip antenna elements fed via aperture coupling," M.Eng.thesis, Royal Military College of Canada, 1989.

[6] Harrington, R.F., *Time Harmonic Electromagnetic Fields*, McGraw Hill Book Co., 1961.

[7] Lo, Y.T., Solomon, D., Richards, W.F., "Theory and Experiment on Microstrip Antennas", *IEEE Trans. Antennas Propagat.*, vol. AP-27, pp. 137-145, 1979.

[8] E.O. Hammerstad and F. Bekkadal, "A microstrip handbook," ELAB Rep. STF44A74169, N7034, Univ. Trondheim-NTH, Norway, 1975.

[9] M. Kirschning, R.H. Jansen, and N.H.L. Koster, "Accurate model for open end effect of microstrip lines," *Electron. Lett.*, vol. 17, pp. 123-125, 1981.

[10] D. M. Pozar, " A reciprocity method of analysis for printed slot and slot-coupled microstrip antennas", *IEEE Transactions on Antennas and Propagation*, vol. 34, no. 12, Dec. 1986.

[11] Hoffman, R. K., *Handbook of Microwave Integrated Circuits*, Artech House, 1983.

[12] L.R. Rao and B.N. Das, "Impedance charactersitics of transverse slots in the ground plane of a stripline," *Inst. Elec. Eng. Proc.*, vol. 125, no. 1, pp. 29-32, 1978.

[13] K.R. Carver and J.W. Mink, "Microstrip antenna technology," *IEEE Trans. Antennas Propag.,* vol. 29, pp. 2-24, 1981.

[14] E. Lier, "Improved formulae for input impedance of coax-fed microstrip patch antennas," *Inst. Elec. Eng. Proc.*, vol. 129, no.4, pp.161-164, 1982.

[15] W.J.R. Hoefer, "The transmission line matrix (TLM) method," in: **Numerical Techniques for Microwave and Millimeter Wave Passive Structures,** Edited by T. Itoh, New York: Wiley, 1989.

[16] N.R.S. Simons, "Developmentand application of differential-equation based numerical techniques to electro-magnetic scattering and radiation problems," Ph.D. thesis, University of Manitoba, 1994.

[17] S. Akhtarzad and P.B. Johns, "Generalized elements for the TLM method of numerical analysis," *Proc. Inst. Elec. Eng.*, vol. 122, no. 12, pp. 1349-1352, December 1975.

[18] A. M. Tran and T. Itoh, "Analysis of microstrip lines coupled through an arbitrarily shaped aperture in a thick common ground plane," *IEEE MTT-S Digest*, pp. 819-822, 1993.

[19] P. R. Haddad and D. M. Pozar, "Ananlysis of an aperture coupled microstrip patch antenna with a thick ground plane," *IEEE Antennas and Propagation Society International Symposium Digest,* Symposium Slides, vol. 2, pp. 932-935, 1994.

[20] P. R. Haddad and D. M. Pozar, "Characterisation of aperture coupled microstrip patch antenna with thick ground plane," *Electronic Letters*, vol. 30, no. 14, pp. 1106-1107, 1994.

[21] A. Ittipiboon, S. Meszaros and M. Cuhaci, :"S-Parameter description of microstrip slot-couplers," *ANTEM' 92*, pp. 632-636, 1992.

[22] S. B. Cohn, "Microwave coupling by large apertures," *Proc. IRE.*, vol. 40, pp. 696-699, 1952.

[23] F. Masot, F. Medina, and M. Horno, "Analysis, synthesis, and experimental validation of a new type of microstrip transition," *IEEE Transactions on Microwave Theory and Techniques, vol. 43, no. 1, Jan. 1995.*

[24] T. Pratt and C.W. Bostian, **Satellite Communications**, John Wiley & Sons, 1986.

References

[25] D. M. Pozar, **Microwave Engineering**, Addison-Wesley Publishing Company, 1990.

[26] D.J. Roscoe, "The development of active integrated antennas and a design methodology," Ph.D. thesis, University of Manitoba, 1993.